1-31-2013

Numerical analysis of surface mount electronics with viscoelastic epoxy underfills and potting

Matthew Neidigk

Recommended Citation

Neidigk, Matthew. "Numerical analysis of surface mount electronics with viscoelastic epoxy underfills and potting." (2013). https://digitalrepository.unm.edu/me_etds/16

Matthew Neidigk
Candidate

Engineering
Department

This dissertation is approved, and it is acceptable in quality and form for publication:

Approved by the Dissertation Committee:

Dr. Yu-Lin Shen, Chairperson

Dr. Tariq Khraishi

Dr. Mahmoud Taha

Dr. Zayd Leseman

Numerical Analysis of Surface Mount Electronics with Viscoelastic Epoxy Underfills and Potting

By

Matthew A Neidigk

DISSERTATION

Submitted in partial fulfillment
of the requirements
for the degree

DOCTOR OF PHILOSOPHY

Engineering

The University of New Mexico

Albuquerque, New Mexico

December 2012

For my wife Valerie and my six beautiful children.

ACKNOWLEDGEMENTS

I would like to express my deepest appreciation to Doug Adolf, whose vision, technical expertise, and mentoring made this possible. I am saddened that his retirement from Sandia National Laboratories didn't allow him to see this process to completion. I would also like to thank Robert Chambers who has been a wonderful mentor and friend both personally and professionally.

I would also like to offer my appreciation to my university advisor Professor Yu-Lin Shen, who has very patiently guided me through this process. In addition, I would like to thank the members of my dissertation committee, Professor Tariq Khraishi, Professor Mahmoud Taha, and Professor Zayd Leseman, who have given their time and expertise to better my work.

I would also like to express my thanks to the experimentalists Mark Stavig, Kevin Austin, and Scott Spangler at Sandia National Labs for taking the data that made the polymer modeling possible. Also thanks are due to Mike Neilsen for sharing his time and viscoplastic braze model work with me.

Sandia is a multiprogram laboratory operated by Sandia Corporation, a Lockheed Martin Company, for the United States Department of Energy's National Nuclear Security Administration under contract DE-AC04-94AL85000

Numerical Analysis of Surface Mount Electronics with Viscoelastic Epoxy Underfills and Potting

By

Matthew Neidigk

B. S., Mechanical Engineering, New Mexico State University, 1996
M. S., Mechanical Engineering, New Mexico State University, 2001
PhD., Engineering, University of New Mexico, 2012

ABSTRACT

Surface mount technology is quite common in modern electronics industry. In some instances, printed circuit boards (PCBs) have been encapsulated in foam or epoxy to improve survivability. When packaging PCBs to survive operational environments, it is important to understand the stresses and strains generated during manufacturing and thermal cycling in addition to dynamic loading. The large disparity in the coefficients of thermal expansion (CTE) of polymers, ceramic components, metal solders, and PCBs can generate significant stress during thermal cycling. Cracking of encapsulants or ceramic components, underfill debonding, and solder fatigue are just a few of the potential failure mechanisms that may result. An extensive numerical parameter study was performed to investigate the response representative surface mount components to thermal cycling. Generic packaging design guidelines were identified to reduce component stress, and maximize solder fatigue life.

Table of Contents

List of Figures

List of Tables

1 Introduction

1.1 Motivation for Research

At the onset of this research effort, much work had been done by scientists at Sandia National Laboratories in the field of nonlinear viscoelastic constitutive modeling. Doug Adolf and Robert Chambers had recently completed their Potential Energy Clock (PEC) model with Purdue's J. Caruthers, and were in the process of developing the Simplified Potential Energy Clock (SPEC) model. Section 2.1 of this dissertation details the need that prompted these efforts and the resulting models. As a new PhD student, I applied the PEC model to its first practical application and published the results with my advisor Yu-Lin Shen [1]. A brief summary of the paper is included in Section 9.1. The publication of this paper ultimately led to our collaborative efforts in the area of electronics packaging. To further their efforts, Doug Adolf and Robert Chambers allowed me to assist with the extensive validation of the SPEC model, resulting in my inclusion as a coauthor of the paper [2]. Under the tutelage of Robert Chambers, I modified the SPEC model to include a general filled capability (Section 2.2) based on research done by Doug Adolf. By combining these polymer research efforts with the solder viscoplasticity research work of another Sandian, Michael Neilsen, I was able to compile all the tools necessary to computationally model electronics packaging. This dissertation summarizes much of the information I have compiled, models I have created, and results I have obtained, with the intent of fully understanding packaging of surface mount electronics.

1.2 Overview

Surface mount technology is quite common in the modern electronics industry. A diagram depicting common packaging materials for a surface mounted component can be seen in Figure 1-1. Examples of surface mounted components can be seen in Figure 1-2 and Figure 1-3. In some instances, boards have been encapsulated in foam or epoxy to improve survivability against moisture, chemical agents, radiation and hostile environments [3-6]. An example of a sectioned, packaged component can be seen in Figure 1-4. When designing printed circuit boards (PCBs) to survive operational environments, it is important to understand the stresses and strains generated during manufacturing and thermal cycling in addition to dynamic loading. The large disparity in the coefficients of thermal expansion (CTE) of polymers, ceramic components, metal solders, and PCBs can generate significant stress during thermal cycling. Cracking of encapsulants or ceramic components, underfill debonding, and solder fatigue are just a few of the potential failure mechanisms that may result.

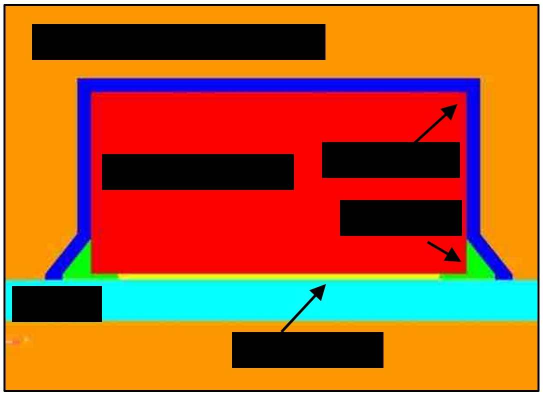

Figure 1-1: Encapsulated component with underfill and elastomer coating.

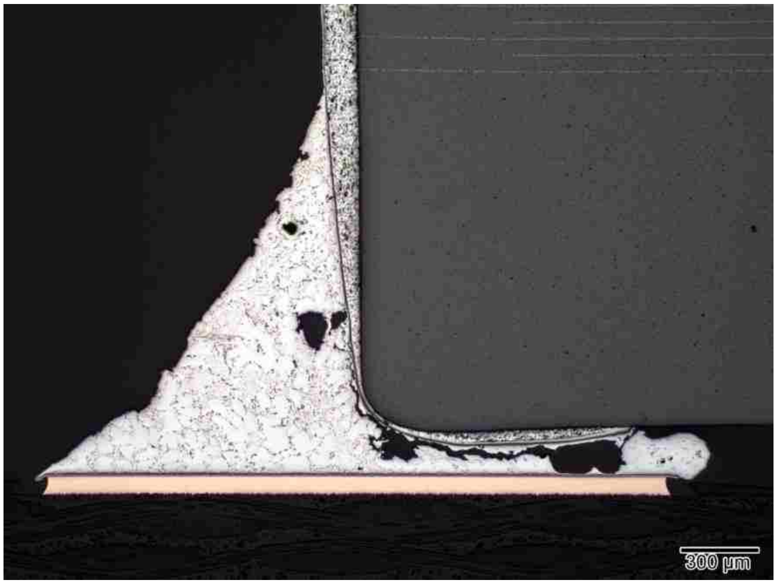

Figure 1-2: Cross-sectioned “large” capacitor with cracked solder joint.

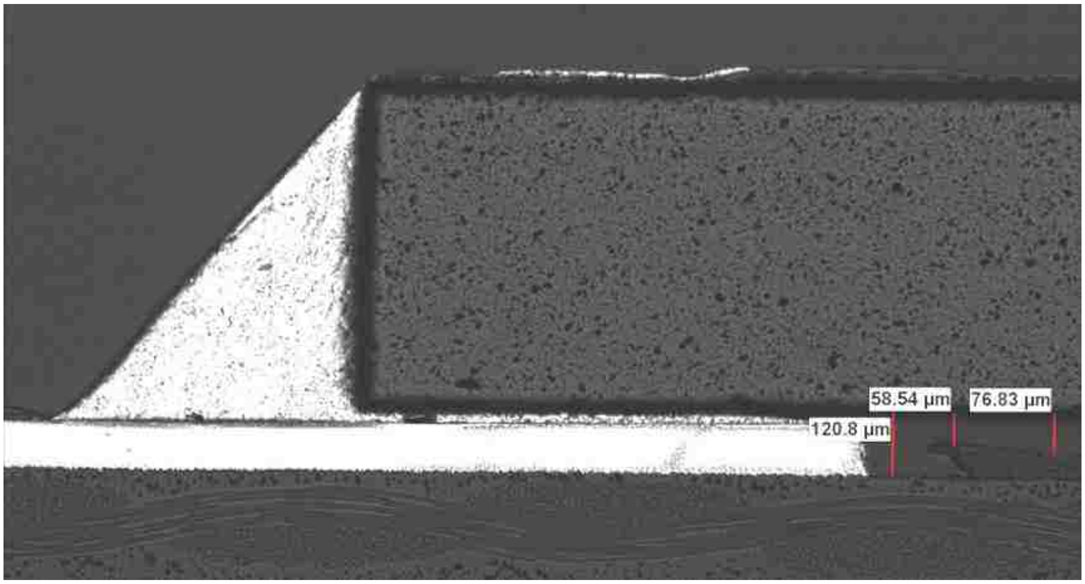

Figure 1-3: Cross-sectioned “small” resistor with intact solder joint.

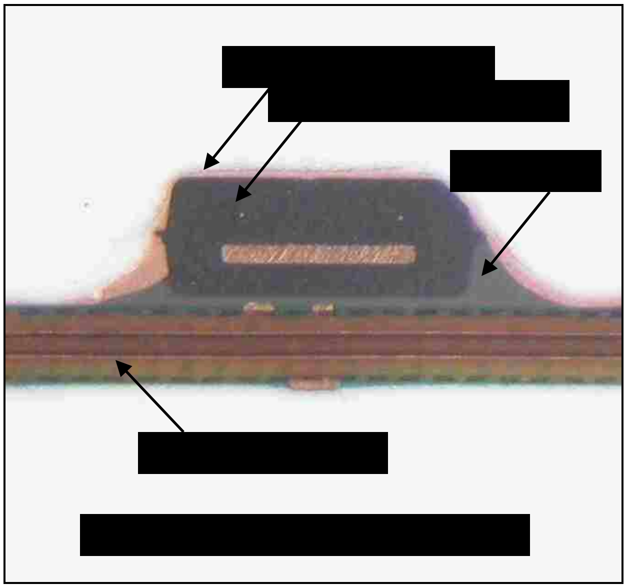

Figure 1-4: Encapsulated component with underfill and elastomer coating.

To increase the reliability of surface mounted electronics, glassy thermosets are sometimes used as underfills. See for example the results of the simple finite element model shown in Figure 1-5 and Figure 1-6. Figure 1-5 depicts a surface mount, ceramic capacitor soldered to a PCB subjected to a 4-point bend test. The maximum principal stress contours of the capacitor with and without the underfill are shown in Figure 1-6. In the plots, everything in red is in excess of 70 MPa. Although the circuit board deflection is the same for both cases, the tensile stresses in the ceramic are significantly reduced in the case with an underfill. The presence of underfills can affect the solder reliability and component failure during dynamic environments as well.

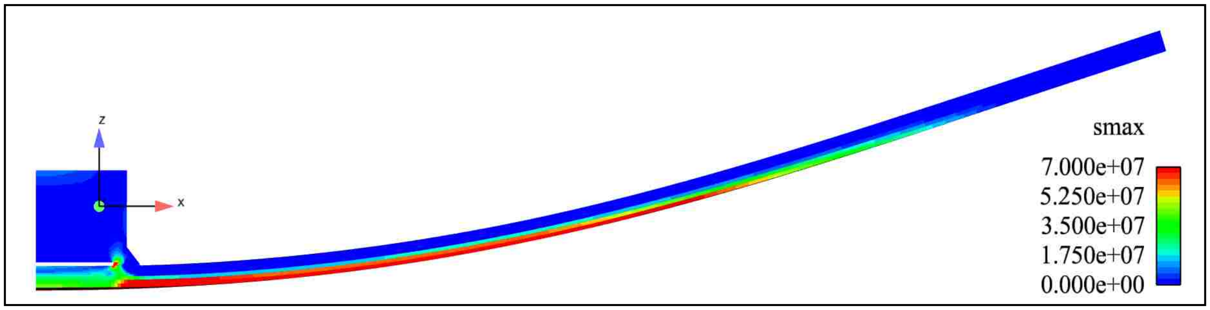

Figure 1-5: Contour plot of maximum principal stress in PCB and capacitor (without underfill) during 4-point bend test.

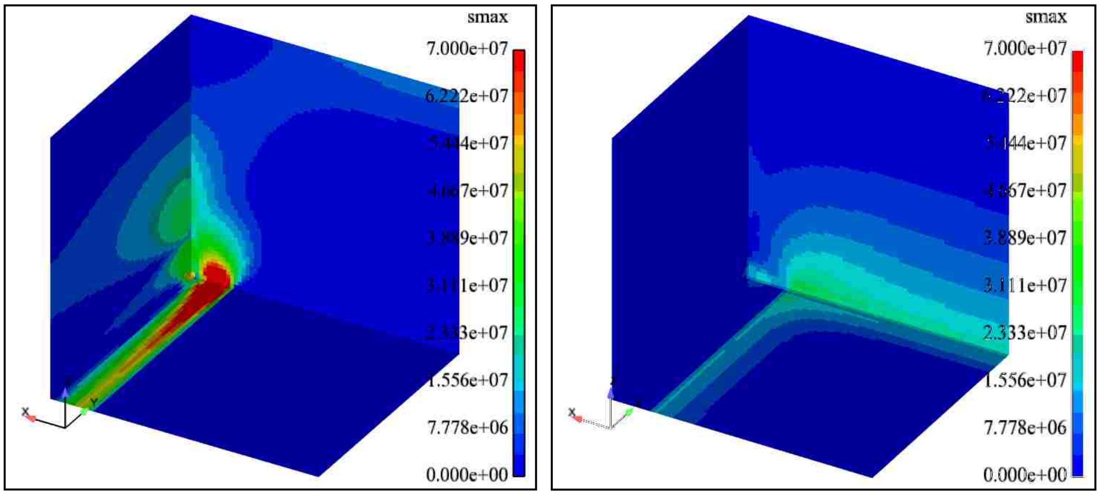

[redacted]

[redacted]

Figure 1-6: Maximum principal stress contour plots for capacitor with and without underfill.

By adding filler to the polymer as shown in Figure 1-7, underfill mechanical properties such as the bulk and shear moduli and the CTE can be tailored. Filler options include glass micro-balloons (GMB) or hard fillers such as silica or alumina.

Figure 1-7: Silica filler (left) and alumina filler (right).

Solder fatigue is a result of strains generated by the CTE mismatch between dissimilar materials in the assembly. Deformation and cracking of solder has been an important subject for many numerical investigations [7-12]. The addition of a glassy thermoset epoxy or foam encapsulation, or elastomeric stress relief coating can only increase the complexity of the stress state in the assembly, and sometimes in a non-intuitive way.

1.3 Approach

While historical lore, and past experience can sometimes produce successful packaging strategies, this approach may not necessarily result in the best design options. The goal of this dissertation was to develop generic packaging guidelines, as well as demonstrate methodologies for determining optimal solutions for specific applications. The approach combines experimental tests and computational simulations to understand the advantages and disadvantages of various encapsulation, coating, and underfill choices, to identify material properties which lead a robust design. While dynamic stresses from vibration and impact are important, understanding the residual manufacturing stress is a critical first step for determining margins. In many cases, if a packaged electronic assembly can survive thermal cycling, it can survive almost anything. With this in mind, quasi-static stresses from manufacturing and thermal cycling are the primary subject of this research.

To compare and assess design and material choices, accurate material models were needed. As part of this research effort, the nonlinear viscoelastic Simplified Potential Energy Clock (SPEC) model [2] was extensively validated and used to model the thermoset epoxy encapsulation. In addition, the SPEC model was modified to include a general filled capability [13], which allowed for efficient modeling of filled underfills. By combining these models with a unified creep plasticity model for solder [14], an excellent tool for investigating the effects of various underfills on surface mounted components was created. Using the Coffin-Manson solder fatigue criterion [15], this tool was then used to investigate solder fatigue life in various packaging configurations. The details of the material models are outlined in Chapter 2.

2 Material Modeling and Characterization

2.1 Simplified Potential Energy Clock Model

2.1.1 *Demonstrated Need*

As described by Caruthers *et al* [16], for the last few decades, the polymer rheology and continuum mechanics communities have attempted to develop constitutive equations to describe the response of viscoelastic materials during arbitrary temperature and deformation histories. This has been an enormously difficult endeavor due to the wide range of mechanical behavior that is observed for amorphous polymers. At temperatures above the glass transition temperature (Tg), these materials demonstrate rubber elasticity or time-dependent non-Newtonian flow behavior, while at temperatures below or near Tg, nonlinear viscoelasticity and physical aging are observed. In the Tg region itself, polymers exhibit thermal history dependent volume and enthalpy relaxation. Amorphous polymers are linear viscoelastic for infinitesimal strains both in the rubbery and glassy states; however, the relaxation times grow longer during thermal cooling at and below the glass transition temperature [17]. Predicting this glassy polymer behavior has been modeled using two formulations, plasticity and nonlinear viscoelasticity. Although each of these approaches is able to predict some subset of glassy polymer behavior, neither, until the creation of the PEC model [16], had been able describe the full range of relaxation behavior under arbitrary time, temperature, and deformation histories.

Plasticity theories are a common tool used to model yield in polymers [18-22]. In many cases, enthalpy relaxation and physical aging are neglected, and one major limitation is the inability to predict the return to the original state after yield when heated above Tg. These are just a few limitations due to the fact that the dependence of plastic strain on temperature, rate and pressure is typically fitted to limited data, and is physically unrelated to the underlying viscoelasticity.

Nonlinear viscoelastic constitutive equations preserve the continuous transition between the rubbery and glassy states. In addition, mechanical yield is the result of the nonlinear relaxation behavior induced by loading. Viscoelastic models are capable of describing a wide range of nonlinear viscoelastic phenomena when the relaxation time scale is coupled to the materials state given by the temperature, specific volume, and strain. The nonlinear viscoelastic constitutive equations discussed in this section use the concept of a 'material clock' [23-25] to describe viscoelastic relaxation rates in glassy polymers. Just as the 'WLF shift factor' defines the dependence of the relaxation rates on temperature [26], material clock models affect nonlinear behavior by including additional terms in the clock.

A key assumption of clock models is that the current state of the material controls the instantaneous rate of relaxation. The challenge is then identifying the "variable" or term that controls the rate of relaxation. Some examples found in the literature include: volume terms [27-30], entropy terms [31], stress terms [32-33], and strain terms [34-35]. Given that these models are designed to capture only a portion of the overall nonlinear viscoelastic response, other physical behaviors are neglected. Phenomena such as volume recovery [30, 36-37] and enthalpy relaxation [38-40] have been examined with some success; however, the mechanical response, e.g. compressive or tensile yield, is not considered. In other models, the mechanical response is examined [41-42], but the complex thermodynamic response is neglected. It would be possible to continue developing new models for specific relaxation phenomena by adding new pieces to existing constitutive models; however, a true constitutive equation should anticipate a materials behavior.

Another key assumption of clock models is thermorheological simplicity. In a thermorheologically simple material, the shape of the relaxation spectrum does not change. Thermorheological simplicity appears to be a reasonable assumption, although some polymers may exhibit slight deviations [43].

“Rational Mechanics” [44] is a rigorous theory of continuum thermodynamics for nonlinear viscoelastic materials. The key result of Rational Mechanics is that the stress tensor, internal energy, and entropy can all be determined from a single Helmholtz free energy constitutive functional [45-46]. Note, however, a material clock was not included in Coleman and Noll’s formulation. Following the ideas of Coleman, [47] proposed using a history-dependent material clock. It was also shown that if the clock depends upon a viscoelastic thermodynamic quantity, to remain consistent, the clock itself must be a function of the thermal and deformation histories. Much like Adams and Gibbs [48], Lustig *et al* [47] proposed using configurational entropy as the clock variable. While they were able to demonstrate qualitatively important relaxation features in the glass transition region, the predictions were not quantitative.

2.1.2 *Constitutive Model*

The Simplified Potential Energy Clock (SPEC) Model is a variation of the Potential Energy Clock (PEC) Model [16], a nonlinear thermo-viscoelastic constitutive equation that has a rigorous thermodynamic basis and is capable of predicting a wide variety of mechanical behavior [49-50]. The PEC model, however, was difficult to parameterize, so an effort was made to simplify the model by decoupling the clock and the constitutive equation, and keep only the terms necessary for accurate predictions. The resulting SPEC model has been shown to predict a broad range of mechanical behavior including temperature- and pressure-dependent glass transition, temperature-, pressure- and time-dependent mechanical yielding in tension, compression and shear, the viscoelastic shift factor below glass transition, and the increase of yield stress with glassy aging etc.

Details of the changes made to the PEC model are well documented [2]. The resulting SPEC constitutive equation to calculate stresses in glassy polymers is:

$$
\begin{aligned}
\underline{\underline{\sigma}} = \frac{\rho}{\rho_{ref}} & \left[K_d(T) \int_0^t ds\ f_v(t^* - s^*) \frac{dI_1}{ds} - L_d(T) \int_0^t ds\ f_v(t^* - s^*) \frac{dT}{ds} \right] \underline{\underline{I}} \\
& + \frac{2\rho G_d(T)}{\rho_{ref}} \int_0^t ds\ f_s(t^* - s^*) \left[\underline{\underline{R}}(t) \cdot \underline{\underline{d}}_{dev}(s) \cdot \underline{\underline{R}}^{-1}(t) \right] \\
& + \frac{\rho}{\rho_{ref}} \left[K_\infty(T) I_1 - L_\infty(T) \{T - T_{ref}\} \right] \underline{\underline{I}} + \frac{2\rho G_\infty(T)}{\rho_{ref}} \left[\underline{\underline{R}} \cdot \underline{\underline{\varepsilon}}_{dev} \cdot \underline{\underline{R}}^{-1} \right]
\end{aligned}
$$

Where $t^* - s^* = \int_0^t \frac{dx}{a(x)}$ and $\log(a) = -\frac{C_1 N}{C_2^{"} + N}$

and

$$
C_2^{"} = C_2 \left[1 + \alpha_\infty \left(\frac{T L_d(T_{ref})}{\rho_{ref}} \right) \left(\frac{T_{ref}}{T C_{v_d}(T_{ref})} \right) \right]
$$

and

$$
\begin{aligned}
N = & \left[\{T - T_{ref}\} - \int_0^t ds\ f_v(t^* - s^*) \frac{dT}{ds} \right] + C_3 \left[I_1 - \int_0^t ds\ f_v(t^* - s^*) \frac{dI_1}{ds} \right] \\
& + C_4 \int_0^t ds\ f_s(t^* - s^*) \underline{\underline{d}}_{dev}(s) : \left[\underline{\underline{\varepsilon}}_{dev}(t) - \underline{\underline{\varepsilon}}_{dev}(s) \right]
\end{aligned}
$$

Note that terms, X_d, are defined as the difference of the glassy and rubbery values, X_g - X_∞. C_v is the specific heat capacity at constant volume, $\underline{\underline{d}}$ is the unrotated rate of deformation tensor, $\underline{\underline{\varepsilon}}$ is the integrated strain rate, I_1 is the first invariant, $\underline{\underline{\varepsilon}} : \underline{\underline{I}}$, approximated by $\alpha_\infty \Delta T$ (α_∞ is a volumetric CTE), the deviatoric strain $\underline{\underline{\varepsilon}}_{dev}$ is $\underline{\underline{\varepsilon}} - \frac{1}{3} I_1 \underline{\underline{I}}$, and $\underline{\underline{R}}$ is the rotation tensor obtained from the decomposition of the deformation tensor into its rotation and stretch components, $\underline{\underline{F}} = \underline{\underline{R}} \cdot \underline{\underline{U}}$. Table 2-1 lists the required input parameters. Note, that the equation for log (*a*) exactly reproduces the historical WLF equation [26] in equilibrated free expansion.

Table 2-1: Variables used in the SPEC nonlinear viscoelastic model.

variable	definition
ρ	density
T	temperature
T_{ref}	reference temperature where the epoxy is stress free
ρ_{ref}	density at the reference temperature
K_∞	temperature dependent equilibrium (i.e., above Tg) bulk modulus
L_∞	K_∞ times the equilibrium volumetric CTE, α_∞
G_∞	temperature dependent equilibrium shear modulus
K_d	temperature dependent glassy bulk modulus, K_g, minus K_∞
L_d	$K_g\alpha_g$ - L_∞, where α_g is the glassy volumetric CTE
G_d	temperature dependent glassy shear modulus, G_g, minus G_∞
$\underline{\underline{R}}$	rotational component of the deformation gradient
$\underline{\underline{d}}_{dev}$	the deviatoric unrotated rate of deformation tensor
$\underline{\underline{\varepsilon}}_{dev}$	time integral of $\underline{\underline{d}}_{dev}$
I_1	first invariant of $\underline{\underline{\varepsilon}}_{dev}$
C_1	first WLF coefficient
C_2	uniquely related to the second WLF coefficient
C_3	constant producing the pressure dependence of Tg
C_4	constant producing yield
τ_s	stretched exponential time constant for the shear spectrum
β_s	stretched exponential exponent for the shear spectrum
τ_v	stretched exponential time constant for the volumetric spectrum
β_v	stretched exponential exponent for the volumetric spectrum

2.1.3 ***SPEC Model Validation***

As with the potential energy clock model, it was necessary to model a variety of tests using the simplified potential energy clock model to verify that the model accurately predicted the nonlinear viscoelastic behavior of glassy polymers. Several such tests were performed and are summarized below. Similar to the potential energy clock model validation [50], no attempt was made to characterize the exact materials investigated in some of the cited publications, as the intent was to predict the “physical behavior” of the polymers using the SPEC model. The epoxy encapsulant chosen for these studies was diglycidyl ether of bisphenol A (Epon 828, Resolution Chemicals) cured with 12 phr diethanolamine (DEA, Fisher Scientific), commonly referred to as 828/DEA.

An iterative process was used for the model parameterization, as changes made to variables in the model for one comparison influenced others. The first step for model parameterization was to accurately predict the volumetric coefficient of thermal expansion (Figure 2-1), shift factor (Figure 2-2), and yield for a glassy polymer (Figure 2-3) used for the PEC model validation [16]. To further demonstrate the capability of the new SPEC model, tensile yield at 23°C for two different cooling histories was also predicted, and can be seen in Figure 2-4.

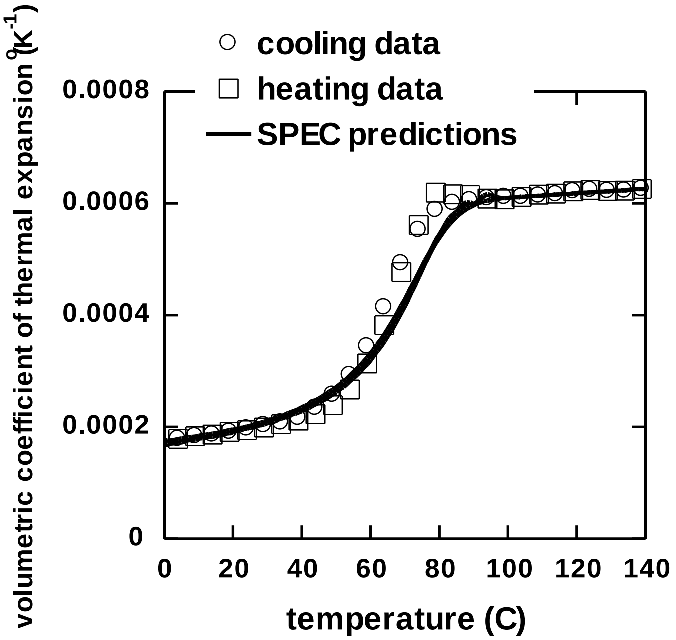

Figure 2-1: Comparison of predictions and data for thermal expansion. Note that the epoxy's Tg is roughly 70°C.

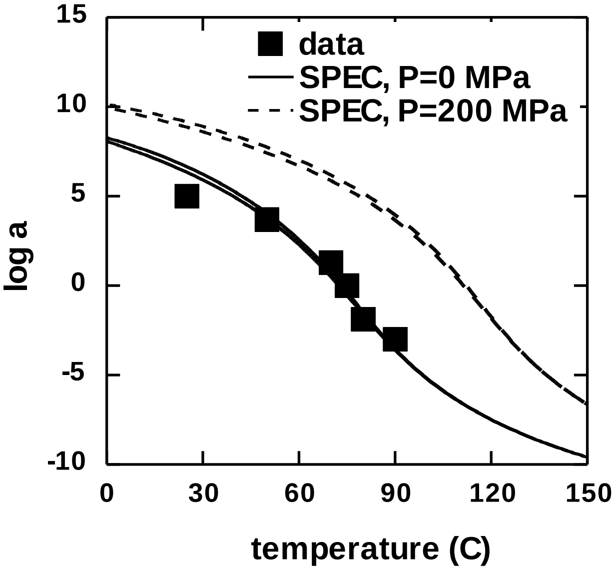

Figure 2-2: Comparison of SPEC predictions and data for the temperature and pressure dependence of Tg.

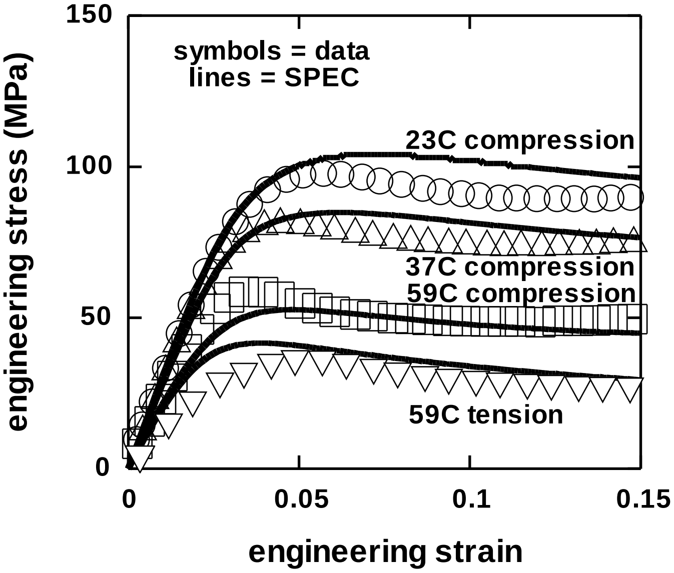

Figure 2-3: Comparison of SPEC predictions and data for the temperature dependence of compressive yield, as well as the difference between tensile and compressive yield at one temperature.

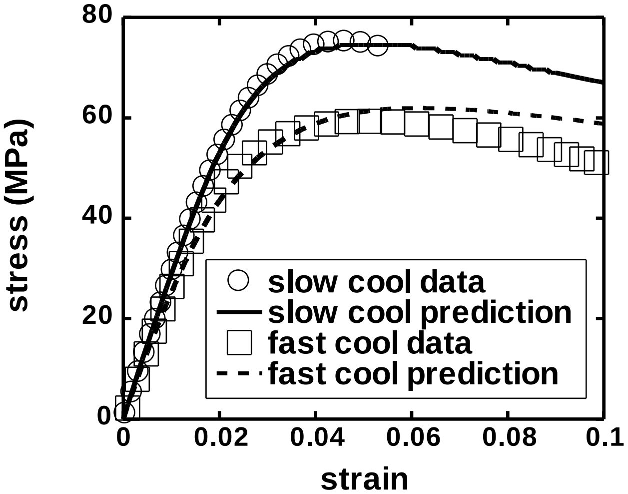

Figure 2-4: Comparison of SPEC predictions and data for tensile yield at 23°C for two different cooling histories.

While better fits were achieved for the volumetric CTE and shift factor, compromises had to be made in order to accurately model the creep behavior. Until now, no creep modeling had been done using the PEC or the SPEC models. Therefore, a series of tensile creep tests at 55°C and 23°C were performed using 828-DEA epoxy. Two cooling profiles were used to investigate physical aging effects. The samples were cooled from well above Tg at rates of 0.1 or 10°C/min by either cooling in the curing mold or quenching on a cold metal plate. The dogbone samples were then displaced using a screw driven Instron machine to determine the yield stresses at the two temperatures. Following loading, creep was allowed for two hours, and measured with an extensometer.

Typical tensile creep data and predictions on the 828/DEA epoxy at room temperature for an applied stress of 55 MPa are shown in Figure 2-5 for two different cooling profiles: a “fast quench” representing placing the sample on a bench after removal from an oven and a “slow cool” representing turning off the power with the sample in the oven. The initial curvature of each response is simply a result of the application of the load plotted on the log scale. Note that the creep rates vary by three orders of magnitude.

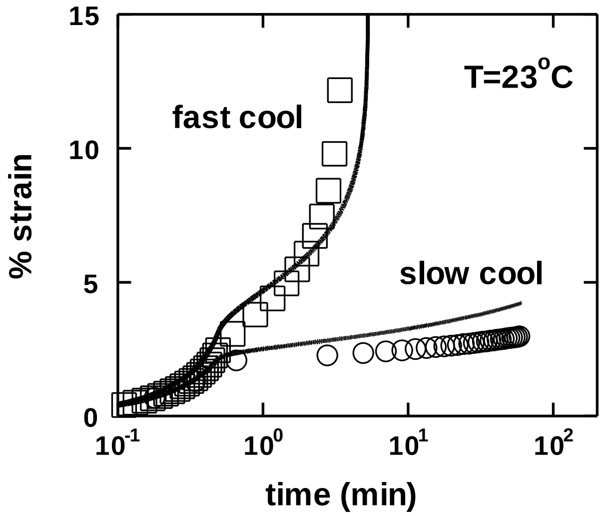

Figure 2-5: Measured and predicted creep at 23°C after a fast quench and slow cool from 100°C for the 828/DEA epoxy at 23°C.

The variables used in the parameterization were C_3, C_4, and the volumetric relaxation spectra terms, as the other terms are based on physical properties of the polymer. As can be seen in the figures, good fits were still achieved for use in engineering applications. The parameters chosen to populate the model can be seen in Table 2-2.

Table 2-2: SPEC model parameters for the 828/DEA epoxy.

parameter	Initial SPEC value	Creep SPEC value	units
T_{ref}	75	75	°C
K_∞ at T_{ref}	3.2	3.2	GPa
dK_∞/dT	-12	-12	MPa/°C
K_g at T_{ref}	4.9	4.9	GPa
dK_g/dT	-12	-12	GPa/°C
linear α_∞ at T_{ref}	600	600	ppm/°C
$d\alpha_\infty/dT$	0.4	0.4	ppm/°C^2
linear α_g at T_{ref}	170	170	ppm/°C
$d\alpha_g/dT$	0.2	0.2	ppm/°C^2
G_∞ at T_{ref}	4.5	4.5	MPa
dG_∞/dT	0	0	MPa/°C
G_g at T_{ref}	0.75	0.9	GPa
dG_g/dT	-4.2	-4.2	MPa/°C
C_1	16.5	16.5	---
C_2	54.5	54.5	°C
C_3	1000	1000	---
C_4	8000	11,800	Pa
τ_s	6	6	sec
β_s	0.24	0.14	---
τ_v	0.12	0.12	sec
β_v	0.22	0.22	---

Using the SPEC parameters for the 828/DEA epoxy, the experiments performed by G'Sell and McKenna [51] were modeled, repeating the efforts for the PEC model validation [50]. The epoxy used in the experiments 828/D230 has a similar Tg (~ 87°C) to 828/DEA. In the test, the 828/D230 epoxy was equilibrated above the glass transition temperature (Tg) and then quenched to temperatures ranging from 5 to 20°C below Tg. The compressive yield stress was then determined as a function of aging time at the various aging temperatures. The experimental paper observes that the yield stresses increase with aging time and then appear to level off. The time at which the yield stress reaches a plateau is dependent on the aging temperature. Although the experimental results are for a different epoxy, the predictions seen in Figure 2-6 are surprisingly close to the data.

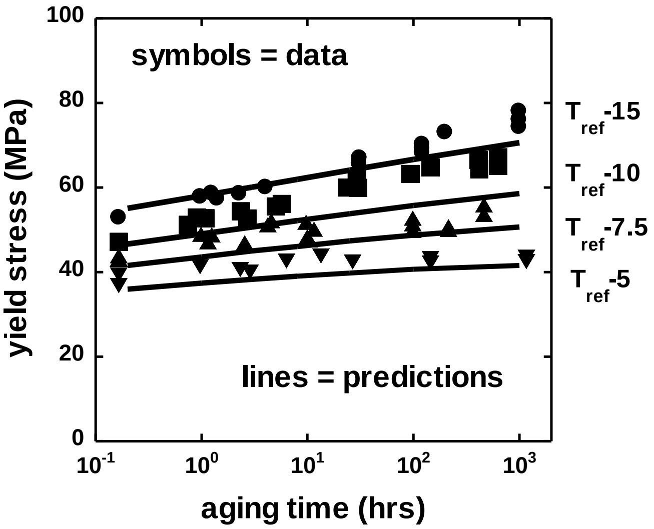

Figure 2-6: Measured and predicted yield stress as a function of aging time.

An additional test modeled using the SPEC model, was conducted by Colucci *et al.* [52]. In these tests, a polycarbonate was annealed above Tg and quenched to room temperature, where a step strain was applied. During the stress relaxation test, the volume was monitored. The experimental paper emphasized the fact that the volume during the test actually decreased below its value just prior to the step strain, and found this to be a peculiar result naming it “volume implosion.” When this test was modeled for the PEC model validation [50], the PEC model predictions showed the cause for these observations. The volume increased at the step strain, but again decreased as the stress relaxed. It appeared that the volume will eventually follow the underlying aging response observed prior to the step strain, which will plateau at the significantly smaller equilibrated volume for the polycarbonate at room temperature. Thus, the volume will naturally decrease below the value measured just prior to the step strain. This test was again modeled using the SPEC model with the parameters for the 828/DEA epoxy. The Tg, however, was shifted to match the experimental systems. The results can be seen in Figure 2-7.

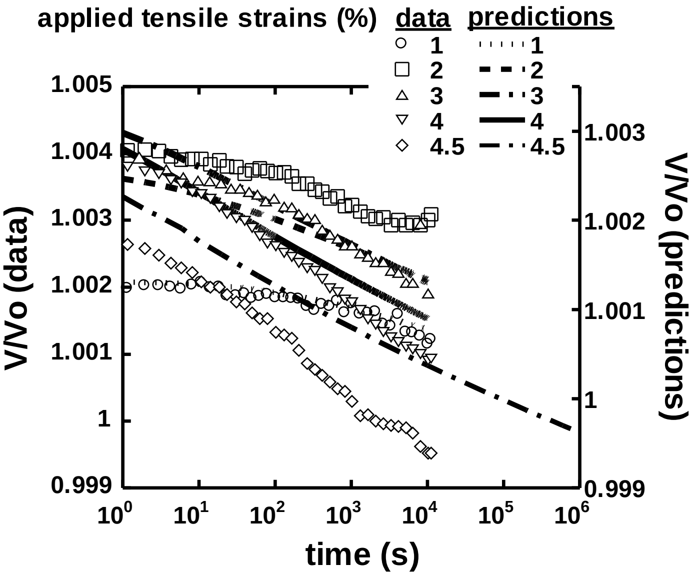

Figure 2-7: Measured and predicted creep at 23°C after a fast quench from 100°C.

Since these test results were extracted from the literature, none of the polymers were characterized. Instead, SPEC model predictions used parameters for the 828/DEA epoxy obtained from Table 2-2 with the Tg (or T_{ref}) shifted to match the experimental systems. Therefore, precise agreement with the data should not be expected. These more complicated tests, however, show the ability of the model to reproduce complex response: physical aging during both yield and creep tests, and coupled mechanical response (tensile stress and volumetric strain). Since the PEC model predictions qualitatively matched the experimental results, they offered another opportunity to validate the simplifying assumptions [2].

With the SPEC validation now complete, the real goal of the effort could now be pursued. Epoxy over-encapsulant can be used to prevent high voltage break-down or support the components and circuit boards during impact. Problems with epoxy over-encapsulants may arise due the high stresses generated in electronic assemblies from the CTE mismatch of the encapsulant and the electronics. These high stresses may lead to shortened thermal cycle fatigue life and diminished margin during impact.

Electronic assemblies are not typically packaged with unfilled epoxy encapsulants unless they are room temperature cured and not subjected to thermal cycling. To reduce thermal manufacturing stresses, filler materials are regularly added to the epoxy encapsulant to modify the mechanical properties. One such filler are glass micro balloons (GMB). As stated by Adolf *et al.* [13], the advantage of these GMB filled encapsulants lies in the variation in thermoelastic properties arising from this unique filler. While most hard fillers (e.g., silica, alumina, titania) lower the CTE, the moduli increase severely. As an example, 40% filler volume fraction of alumina decreases the CTE of 828/DEA to 30 ppm/°C but increases the shear modulus to 5 GPa. Therefore, the effect of additional hard filler on stresses generated during thermal cycles is unclear, and depends on the boundary conditions of that particular problem. GMB fillers, however, reduce the CTE and bulk moduli while increasing the shear modulus only slightly. The product of the CTE and either bulk or Young's modulus is lower when GMB are added, so even in highly confined geometries, the stresses generated during thermal cycles are lower.

The GMB filled epoxy encapsulant chosen for these studies was 828/DEA filled with 48 vol% of GMB (D32/4500, 3M Corp.). As with the 828/DEA, 828/DEA/GMB was fully characterized experimentally, and a similar parameterization was performed as for the unfilled material. The measured and predicted linear CTE for 828/DEA/GMB can be seen in Figure 2-8. The measure and predicted the compressive yield at various temperatures can be seen in Figure 2-9. The parameters used in the SPEC model for the 828/DEA/GMB epoxy can be found in Table 2-3.

Throughout this dissertation, 828/DEA/GMB will be referred to as GMB epoxy, which is the over-encapsulation used in the electronics packaging parameter studies.

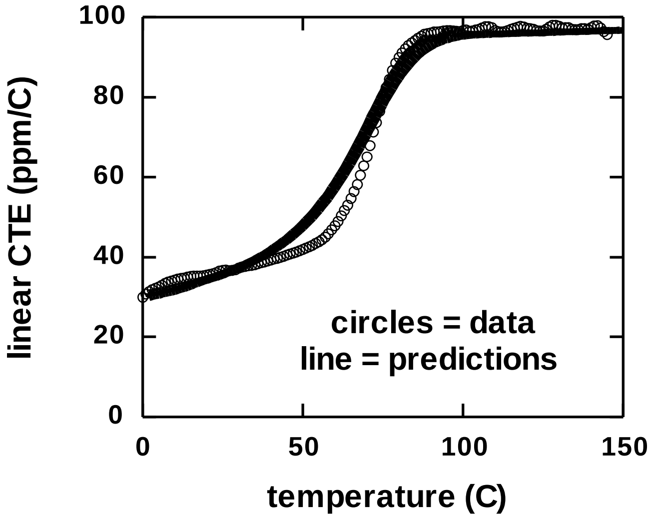

Figure 2-8: 828/DEA/GMB measured and predicted volumetric strains in free expansion.

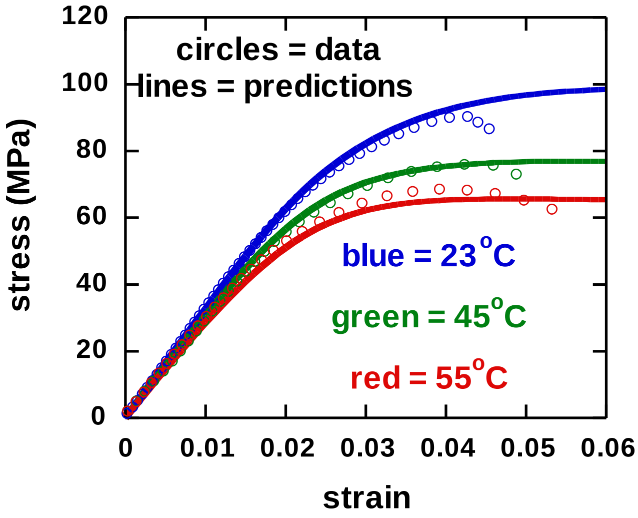

Figure 2-9: 828/DEA/GMB measured and predicted compressive yield at various temperatures.

Table 2-3: SPEC model parameters for the 828/DEA/GMB epoxy.

variable	value	units
ρ_{ref}	750	kg/m^3
T_{ref}	75	°C
K_∞ at T_{ref}	3.35	GPa
dK_∞/dT	0	GPa/°C
linear α_∞ at T_{ref}	95	ppm/°C
$d\alpha_\infty/dT$	0.023	ppm/°C^2
G_∞ at T_{ref}	40	MPa
dG_∞/dT	0.05	MPa/°C
K_g at T_{ref}	3.35	GPa
dK_g/dT	0	GPa/°C
linear α_g at T_{ref}	27	ppm/°C
$d\alpha_g/dT$	0.033	ppm/°C^2
G_g at T_{ref}	1.2	GPa
dG_g/dT	-1	MPa/°C
C_1	12.5	---
C_2	45.4	°C
C_3	2000	---
C_4	17,500	Pa
τ_s	0.51	sec
β_s	0.231	---
τ_v	20	sec
β_v	0.15	---

2.2 General filled SPEC model

Given that a wide range of curatives and resins are available for underfill applications, it is desirable to have a generic predictive capability. Researchers at Sandia National Laboratories has shown that, while having glass transition temperatures (Tg) differing by as much as 150°C, crosslinked epoxies have very similar properties when normalized about Tg [13]. Thus as an approximation, the nonlinear viscoelastic properties of unfilled 828/DEA epoxy were defined as default inputs for the SPEC model for use in representing a generic underfill material. The user must then only specify the actual Tg and stress free temperature. In addition, fillers can greatly affect the underfill properties. If the properties of the filler such as moduli and CTE are significantly greater than those of the polymer, properties (ψ) of the composite can be approximated using the following rule of mixtures

$$\Psi = \Psi_e (1 - \phi)^x$$

The subscript e denotes epoxy properties, x is an experimentally determined exponent, and ϕ is the filler volume fraction. By applying this exponential function to the glassy and rubbery moduli terms, thermal expansion terms, and all the corresponding temperature dependent terms, as well as C_4 in the SPEC constitutive equation, reasonable approximations to microparticle filled polymers were achieved. Data and predictions for the compressive yield stress of 828/DEA epoxy filled with 30 and 45 vol% silica beads are shown in Figure 2-10 and Figure 2-11, respectively. In the figures, two predictions are compared to the data. The “best fit” predictions demonstrate the SPEC model fits with the constitutive model inputs specifically tailored to the material (this requires a full characterization of the homogenized material as seen in Section 2.1.3). The “generic filler” predictions demonstrate the generic filled SPEC model fits which only required the glass transition temperature, the filler volume fraction, and the stress free temperature. While the post-yield softening is more pronounced in the “generic filler” fit, these predictions are certainly reasonable for engineering applications. The properties used in the model for the generic unfilled polymer along with the exponents for the generic hard and GMB filled capability can be found in Table 2-4.

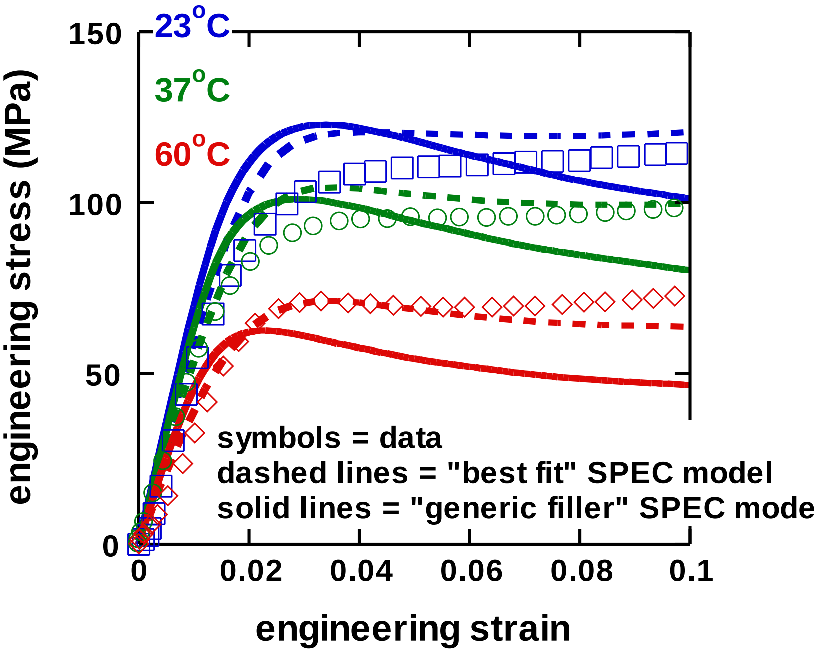

Figure 2-10: Measured and predicted compressive yield of 30 vol% silica filled 828/DEA.

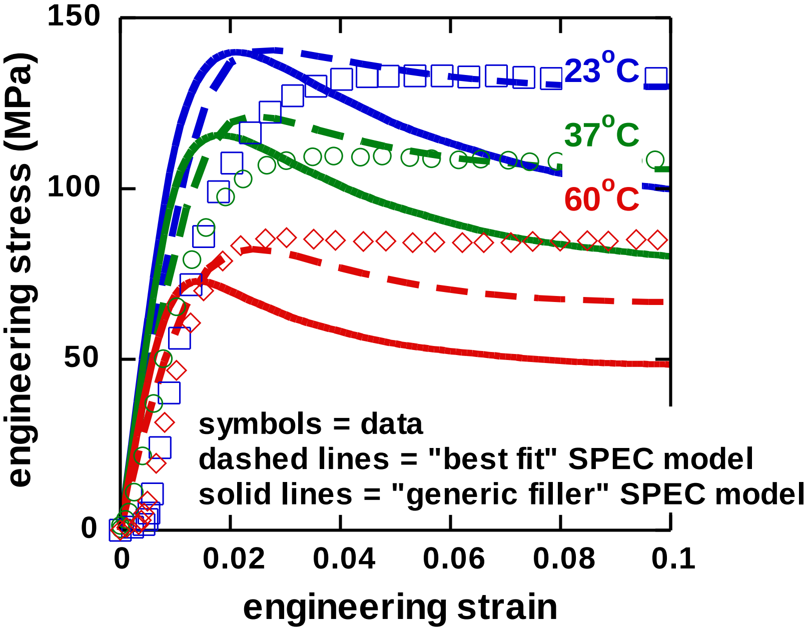

Figure 2-11: Measured and predicted compressive yield of 45 vol% silica filled 828/DEA.

Table 2-4: Filler exponents used in generic filled epoxies.

variable	828/DEA generic inputs	Solid hard filler exponent, x	GMB filler exponent, x
K_∞ at T_{ref}	3.35 GPa	0	0
dK_∞/dT	0 GPa/°C	-1	0
linear α_∞ at T_{ref}	95 ppm/°C	-1	0.67
$d\alpha_\infty/dT$	0.023 ppm/°C^2	1.3	0.67
G_∞ at T_{ref}	40 MPa	1.3	0
dG_∞/dT	0.05 MPa/°C	-2.5	0
K_g at T_{ref}	3.35 GPa	-2.5	0
dK_g/dT	0 GPa/°C	-1	0
linear α_g at T_{ref}	27 ppm/°C	-1	0.67
$d\alpha_g/dT$	0.033 ppm/°C^2	1.3	0.67
G_g at T_{ref}	1.2 GPa	1.3	0
dG_g/dT	-1 MPa/°C	-2.5	0
C_1	12.5	-2.5	0
C_2	45.4°C	0	0
C_3	2000	0	0
C_4	17,500 Pa	0	0
τ_s	0.51 sec	-3.75	0
β_s	0.231	0	0
τ_v	20 sec	0	0
β_v	0.15	0	0

2.3 Incompressible and filled elastomers

Several elastomeric materials were characterized as possible candidates for use as elastomeric “stress relief coatings” in packaged electronics assemblies [13]. The unfilled elastomers selected as possible candidates were Sylgard 184 (Dow Corning) and polysulfide CS3100 (Flamemaster Corp.). Just as GMB filler is added to epoxies, it can be added to elastomers as well. One formulation characterized consisted of Sylgard 184 with 8.3 wt% of a different GMB (A16, 3M Corp.) to modify the composite properties. The A16 GMB has much thinner glass walls than the previously discussed GMB. Likewise, polysulfide elastomers can also be filled with microballoons. In this case, however, phenolic microballoons (Asia Pacific Microspheres) referred to as PMB were used. The PMB were first pre-baked to thin the walls by oxidizing some phenolic, and were then added to the CS3100 polysulfide at 2.7 wt%. In both cases, the filler resulted in a decreased CTE and an increased shear modulus. A summary of the elastic properties for the various unfilled and filled elastomers can be found in Table 2-5. A significant disparity was measured in the bulk modulus for the filled elastomers between damaged and undamaged material. The properties of the damaged materials were used in the packaging analyses, given that the first few thermal cycles crush the fragile balloon materials, resulting in much the damaged material properties.

Table 2-5: Elastomer Elastic Properties.

Properties → Elastomer ↓	**CTE (ppm/°C)**	**Shear Modulus (MPa)**	**Bulk Modulus (MPa)**
Sylgard	300	0.8	920
Polysulfide	280	0.5	2300
Sylgard GMB	185	5.0	3.4
Polysulfide PMB	200	1.3	10

In addition to measuring mechanical properties, elastomer adhesive and cohesive strengths were also measured [13]. Polysulfides were found to fail cohesively at stresses on the order of 1.0 MPa. This was the case for several test methods including shear napkin ring tests (Figure 2-12), butt tension tests (Figure 2-13), and bog bone tension tests. Although dogbone tests were performed to investigate the tensile strength of the silicones, it was found that the material was much more likely to debond due to its extremely low adhesion strength, found to be on the order of 0.1 MPa. The elastomer adhesive and cohesive strength results can be seen in Figure 2-14.

Figure 2-12: Shear napkin ring test geometry.

Figure 2-13: Butt tension test geometry.

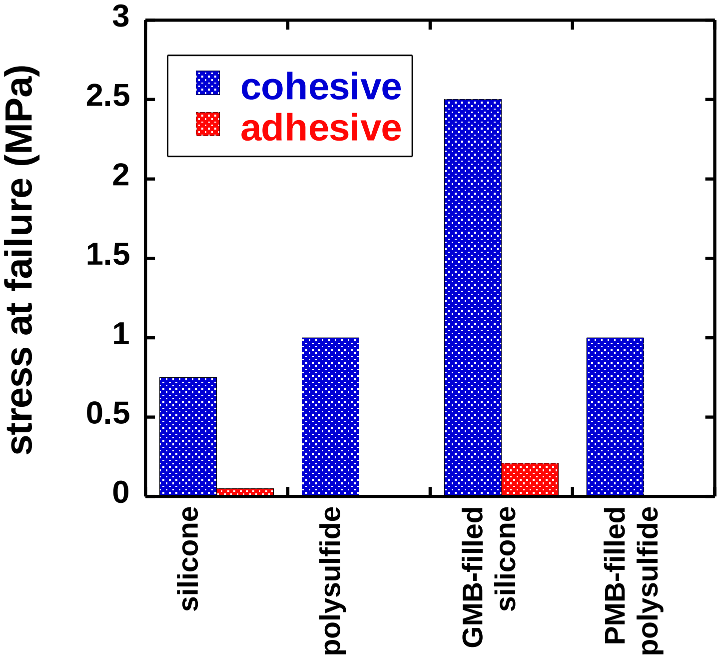

Figure 2-14: Adhesive and cohesive strengths of various elastomer coating materials.

2.4 Viscoplastic solder model

2.4.1 *Constitutive Model*

Stephens and Frear [53] studied the creep behavior of near-eutectic 60Sn-40Pb solder, and found that this solder exhibits significant creep at stress levels well below the yield strength for the material. Its minimum or steady state creep rate, $\dot{\gamma}_{\min}$, could be described using

$$\dot{\gamma}_{\min} = Ae^{\frac{-Q}{RT}}\left[\sinh(\alpha\sigma)\right]^{p} = 2.48x10^{4}\, e^{\frac{-56{,}944}{RT}}\left[\sinh(0.0793\sigma)\right]^{3.04}$$

where *R* is the gas constant, 8.314 J/mole-*K*, *T* is absolute temperature, and σ is true stress in MPa. This result is well suited for the use of a unified creep plasticity model to describe the mechanical behavior of Sn-Pb solders. The implementation of the model was taken directly from [7]. The unified creep plasticity model is based on the model for braze alloys developed by Neilsen et al. [54]. For small elastic strains, the total strain rate, $\dot{\boldsymbol{\varepsilon}}$, can be additively decomposed into elastic, $\dot{\boldsymbol{\varepsilon}}^{e}$, and inelastic (creep + plastic), $\dot{\boldsymbol{\varepsilon}}^{in}$ parts as follows

$$\dot{\boldsymbol{\varepsilon}} = \dot{\boldsymbol{\varepsilon}}^{e} + \dot{\boldsymbol{\varepsilon}}^{in}$$

Also assumed, is that the elastic response is linear and isotropic such that the stress rate is given by

$$\dot{\boldsymbol{\sigma}} = \mathbf{E} : \dot{\boldsymbol{\varepsilon}}^{e} = \mathbf{E} : (\dot{\boldsymbol{\varepsilon}} - \dot{\boldsymbol{\varepsilon}}^{in})$$

where **E** is the fourth-order isotropic elasticity tensor. The inelastic strain rate, $\dot{\boldsymbol{\varepsilon}}^{in}$, is a kinetic equation of the following form

$$\dot{\boldsymbol{\varepsilon}}^{in} = \frac{3}{2}\dot{\gamma}\,\mathbf{n} = \frac{3}{2} f \ \sinh^{p}\left(\frac{\tau}{D}\right)\mathbf{n}$$

where *f* is a function of temperature (typically Arrhenius), the internal state variable *D* is used to account for the isotropic hardening and recovery, and **n** is the normalized stress difference tensor given by

$$\mathbf{n} = \frac{\mathbf{s} - \frac{2}{3}\mathbf{B}}{\tau}$$

The second-order state tensor **B** accounts for kinematic hardening and recovery, **s** is the stress deviator, and τ is a scalar measure of the stress difference magnitude described by

$$\tau = \sqrt{\frac{3}{2}\left(\mathbf{s} - \frac{2}{3}\mathbf{B}\right) : \left(\mathbf{s} - \frac{2}{3}\mathbf{B}\right)}$$

Competing nonlinear hardening and thermal recovery mechanisms are captured by the evolution equations for the internal state variable *D* and the internal state tensor **B**. Evolution of the internal state variable *D* is given by

$$\dot{D} = \frac{A_1 \dot{\gamma}}{(D - D_0)^{A_3}} - A_2 (D - D_0)^2$$

where D_0, A_1, A_2, and A_3 are material parameters. Evolution of the second-order state tensor **B** is given by

$$\dot{\mathbf{B}} = \frac{A_4 \, \dot{\boldsymbol{\varepsilon}}^{in}}{b^{A_6}} - A_5 b \mathbf{B}$$

where A_4, A_5, and A_6 are material parameters and b is the magnitude of **B** as follows

$$b = \sqrt{\frac{2}{3} \mathbf{B} : \mathbf{B}}$$

The inputs for the model can be found in Table 2-6.

2.4.2 ***Coffin Manson fatigue criterion***

The technique to calculate the solder fatigue life begins by subjecting an intact solder joint to a few thermal cycles to determine the equivalent plastic strain in the worst solder element per thermal cycle. If the increase in plastic strain per cycle is constant, the change in plastic strain from a single thermal cycle, ΔEQPS, may be used in the calculation to generate a lifetime prediction (cycles to initiate a crack in the solder joint). Using Solomon's Coffin Manson failure criterion [15], the cycles to failure, N_f, based on the plastic shear strain range, $\Delta\gamma_p$, can be estimated from the increment in equivalent plastic strain from one complete thermal cycle, as follows

$$N_f = \left(\frac{1.14}{\Delta\gamma_p}\right)^{\frac{1}{0.51}} \approx \left(\frac{1.31636}{\Delta EQPS}\right)^{1.96078} \tag{10}$$

Note that this failure model is based on cyclic shear test data over the temperature range of -50 to 125°C. The actual solder properties under cyclic deformation may be influenced by the physical dimension, microstructure, processing history, and loading mode. To facilitate a comparison of predicted fatigue performance as affected by the underfill, this well documented solder failure criterion was chosen.

Table 2-6: Eutectic Sn-Pb Solder – Unified Creep Plasticity Model Parameters.

Temperature (°C)	-60	21	100
Young's Modulus (MPa)	48,276	43,255	36,860
Poisson's Ratio	0.380	0.400	0.430
Flow Rate ln(f)	-44.63	-20.09	-10.72
Sinh Exponent, p	7.1778	4.2074	3.7151
Isotropic Hardening, A_1 (MPa)	270.67	193.44	167.76
Isotropic Recovery, A_2 (1/MPa-sec)	0.37891×10^{-3}	1.8074×10^{-3}	8.3128×10^{-3}
Isotropic Exponent, A_3	0.970		
Kinematic Hardening, A_4 (MPa)	0.0		
Kinematic Recovery, A_5 1/(MPa-sec)	0.0		
Kinematic Exponent, A_6	1.0		
Flow Stress, D_0 (MPa)	8.2759		
Linear Thermal Expansion Coefficient (/°C)	25.0×10^{-6}		

3 Surface Mount Component Finite Element Models

When designing PCBs to survive operational environments, it is important to understand the stresses and strains generated during manufacturing in addition to dynamic loading. The previous chapter described work done to characterize and model the polymers and solders used to package electronic components. In this chapter, the thermal stress finite element models used to evaluate design options for generic surface mounted components are described.

3.1 FE Model description

Two components with significantly different geometries were chosen for the study. First, a “large” capacitor, seen in Figure 1-2, was selected because of its stiff block-like geometry. The second was a small resistor shown in Figure 1-3. Not only is the resistor significantly smaller than the capacitor (0.365”×0.02”×0.125” vs. 0.55”×0.265”×0.5”), the length to thickness ratio also is quite different resulting in more flexible “diving-board” like geometry. The underfill gaps of these components were chosen to represent workable geometries that may be underfilled without screening out the filler because the gap is too small, verses requiring damming around the component because the gap is too large. The gaps assumed for the initial analyses were 0.381 mm (0.015“) for the capacitor and 0.127 mm (0.005”) for the resistor, where the gap is the height that the component sits off the board, or the underfill thickness.

3.1.1 *Mesh and Boundary Condition Details*

Implicit, quasi-static, 3D finite element models of the two representative surface mount components were utilized to model the residual stress and strain due to underfilling and thermal cycling. The assemblies were assumed to be stress free at the underfill cure temperature, and the response of the components as a function of temperature was computed using Sandia National Laboratories' finite element code ADAGIO [55].

The finite element models of the "large" capacitor and "small" resistor are shown in Figure 3-1 and Figure 3-2 respectively. The models were restrained normal to the vertical sectioning planes to approximate a 1/4 symmetry boundary condition (i.e., the xy and yz planes are symmetry planes). To reduce the number of required elements, a fine mesh of each component was inserted into a coarse mesh of the encapsulated printed circuit board using tied contact boundary conditions at the adjacent interfaces. Thermal stresses were generated in each model by cooling the assembly from the underfill cure temperature of 80°C to -55°C, where -55°C is approximately the minimum temperature environment that this component might be expected to experience during its service duration. The assembly was then reheated to 70°C and cooled to -55°C to complete the thermal cycle. Each thermal excursion was performed in 60 minutes. The time-temperature history was created using the cooling rates experienced during the encapsulation process. The extra thermal excursion was used to determine the solder plastic strain due to thermal cycling. The cool-down from the solder stress-free temperature was neglected.

It should be noted that all calculations presented assume a free surface boundary condition. That is, the exterior surface of the encapsulant is not adhered to a "stiff" housing. A stiff housing would produce a high degree of confinement not considered in these analyses.

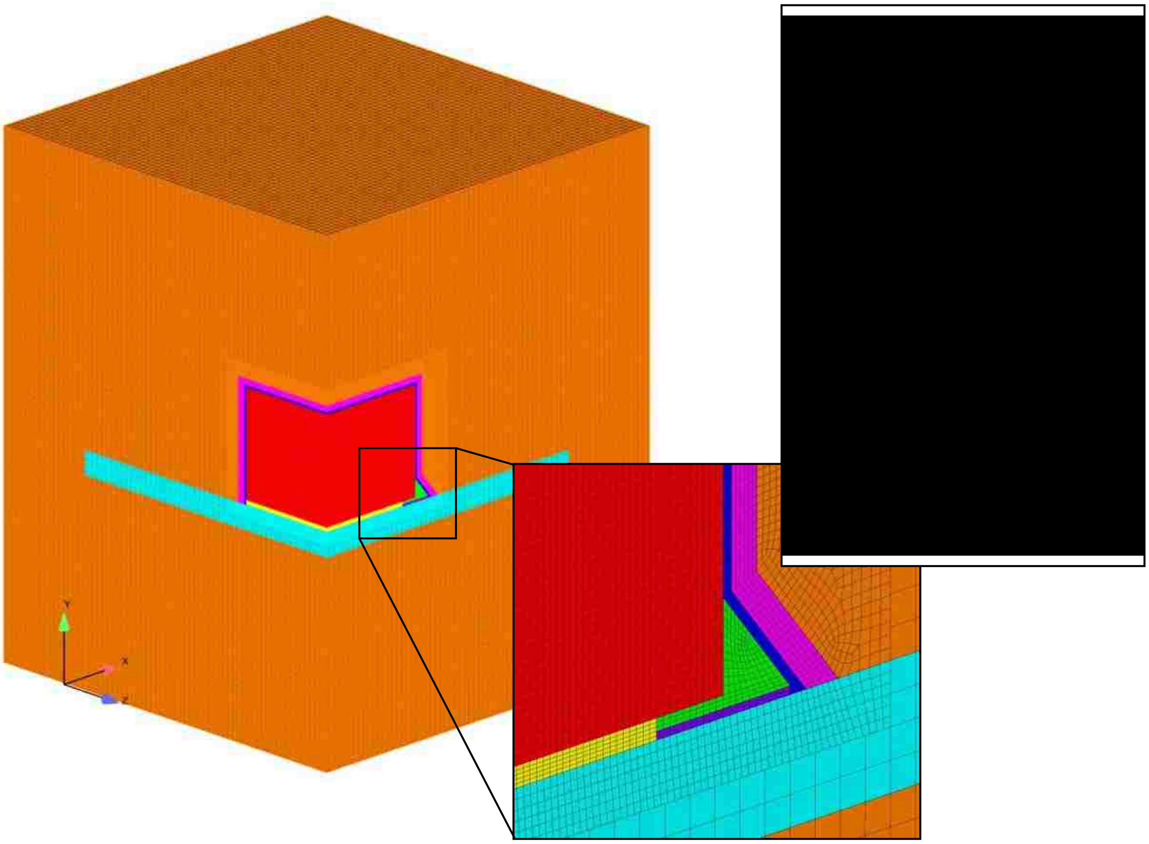

[redacted]

Figure 3-1: Capacitor quarter symmetry finite element mesh used in the finite element analysis.

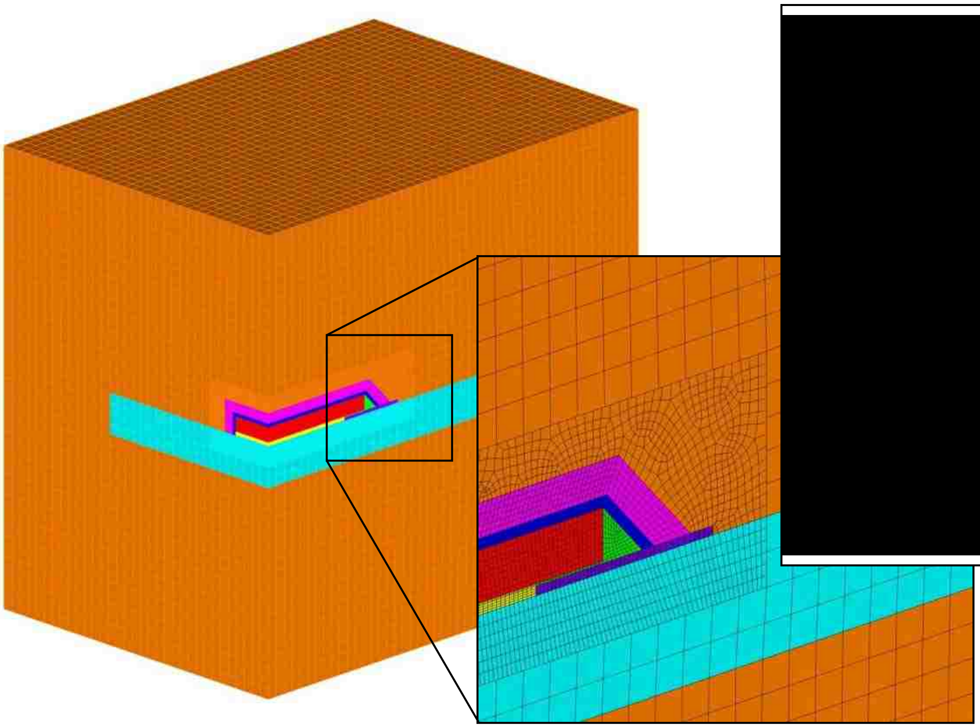

[redacted]

Figure 3-2: Resistor quarter symmetry finite element mesh used in the finite element analysis.

3.1.2 *Material models*

The capacitor and resistor were modeled as an elastic ferrite ceramic. A power law hardening plasticity model was used for the copper solder pads, and an isotropic elastic model was used to simulate the FR4 printed circuit board. The Pb-Sn solder was modeled using unified creep plasticity model described in Section 2.4. Elastomer coating materials were modeled using the elastic properties described in Section 2.3. The epoxy over-encapsulation was modeled using the SPEC Model described in

Section 2.1.2, and the actual inputs used for the 828/DEA/GMB epoxy in the model are given in Table 2-3. An elastic model was assumed when foam was modeled for the encapsulation. Many constants and CTE's used for various materials in the simulations are listed in Table 3-1. The underfill properties were based on the general filled nonlinear viscoelastic capability developed in Section 2.2, with the filler volume fraction (FVF) varied from 0 to 40%.

Table 3-1: Constants and CTE's for various analysis materials.

Material	Young's Modulus (GPa)	Poisson's Ratio	CTE (/°C)	Yield Stress (MPa)	Hardening Constant (MPa)	Hardening Exponent
Ferrite	161.0	0.25	10.4E-6	NA	NA	NA
Copper	117.0	0.34	16.9E-6	0.689	458.7	0.364
FR4	17.2	0.3	16.0E-6	NA	NA	NA
20# Foam	0.11	0.297	45.0E-6	NA	NA	NA

4 Over-encapsulation

Four encapsulation cases were investigated in this study, with the intent of understanding the effect of over-encapsulation on the residual stress state of surface mount components. The capacitor and resistor models described in Chapter 3, and shown in Figure 3-1 and Figure 3-2 were used for the analyses. Investigated, were the following encapsulation cases: no over-encapsulant, 20 lb. foam, and 828/DEA/GMB epoxy, with and without an elastomer coating. While many underfill cases were investigated, both the capacitor and resistor described in this section use a 0.005” thick, 20% FVF hard filled underfill, which should be adequate to identify trends from over-encapsulation. Note, that the intent of this study was not to predict quantitatively the onset of failure in materials, but to identify “trends” that will lead to reductions in residual stress, enhance solder thermal fatigue life, and increase margins for components subjected to harsh dynamic environments.

4.1 Over-encapsulation and Component Stress

The effect of over-encapsulation on component maximum principal stress can be seen in Figure 4-1. In the figure, GMB refers to 828/DEA/GMB epoxy encapsulation, and PMB refers to 828/DEA/GMB epoxy with a PMB filled polysulfide coating. As can be seen in the figure, foam encapsulation slightly decreased the maximum principal stress in both underfilled components. The resistor experienced a 4.9% stress decrease from

48.5 MPa to 46.1 MPa, and the stress in capacitor decreased from 57.0 MPa to 56.5 MPa, or 0.9%.

A common trend, however, was not identified for the epoxy encapsulated components, where the resistor maximum principal stress decreased, but the capacitor stress increased with the addition of encapsulation. For the resistor, the addition of the epoxy encapsulation decreased the maximum principal stress by 12% from 48.5 MPa to 42.7 MPa, and if an elastomer coating was included, the stress in the resistor decreased from 48.5 MPa to 44.0 MPa, or 9.3%. For the capacitor, however, a stress increase of 12% from 57.0 MPa to 63.9 MPa was realized with the addition of the epoxy encapsulation, which further increased from 57.0 MPa to 115 MPa, or 101% with the addition of an elastomer coating.

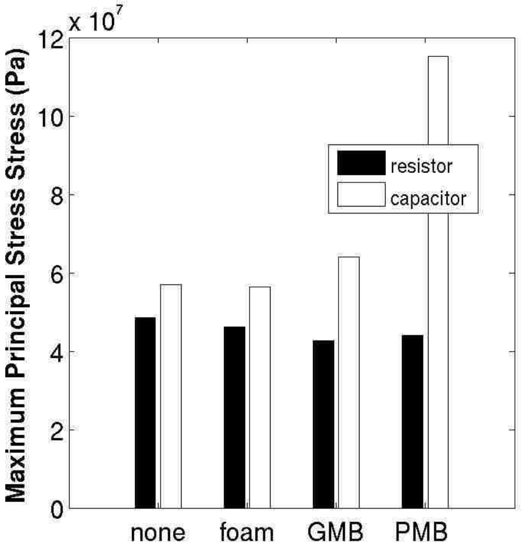

Figure 4-1: Peak ceramic maximum principal stress in capacitor and resistor for various over-encapsulation cases.

4.2 Over-encapsulation and Underfill Stress

Figure 4-2 demonstrates the underfill maximum principal stress as a result of over-encapsulation. As in the previous figure, GMB refers to 828/DEA/GMB epoxy encapsulation, and PMB refers to 828/DEA/GMB epoxy with a PMB filled polysulfide coating. Similar to the component stress results, foam encapsulation resulted in a slight decrease in underfill maximum principal stress in both components, and the resistor stress decreased 0.6% from 67.2 MPa to 66.8 MPa, while the capacitor stress decreased 1.6% from 68.7 MPa to 67.6 MPa.

828/DEA/GMB epoxy encapsulation resulted in an underfill stress increase for both the resistor and capacitor. As seen in the figure, the resistor maximum principal stress increased from 67.2 MPa to 69.2 MPa, or 3.0%, and inclusion of an elastomer coating resulted in a stress increase of 27%, from 67.2 MPa to 85.3 MPa. The underfill stress in the epoxy encapsulated capacitor increased 31% from 68.7 MPa to 99.3 MPa, and by including an elastomer coating, the maximum principal stress increased from 68.7 MPa to 161.5 MPa, or 135%.

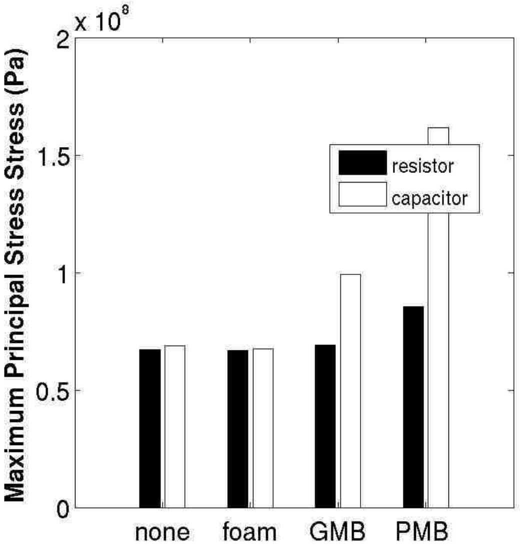

Figure 4-2: Peak underfill maximum principal stress in capacitor and resistor for various over-encapsulation cases.

4.3 Over-encapsulation and Solder Fatigue

The results for solder fatigue and over-encapsulation for the capacitor and resistor can be seen in Figure 4-3. As before, GMB refers to 828/DEA/GMB epoxy encapsulation, and PMB refers to 828/DEA/GMB epoxy with a PMB filled polysulfide coating. While the stress results were not significantly modified by foam encapsulation, solder fatigue does appear to be affected. The addition of foam encapsulation reduced the resistors solder fatigue life by 15% (21,865 cycles to 18,524 cycles), and by 63% (13,117 cycles to 4,907 cycles) for the capacitor.

The results were so dramatic for the epoxy encapsulated components, that a second plot was included in the figure to depict the results separately. The resistor experienced a decrease of 91% in fatigue life, from 21,865 cycles to 1,987 cycles. The addition of an elastomeric coating further reduced the fatigue life by 93% from 21,865 cycles to 1,577 cycles. The capacitor, however, suffered the greatest loss in fatigue life, where a decrease of ~98% was experienced for both cases with and without the elastomer coating (13,117 cycles to 263 cycles or 13,117 cycles to 243 cycles respectively).

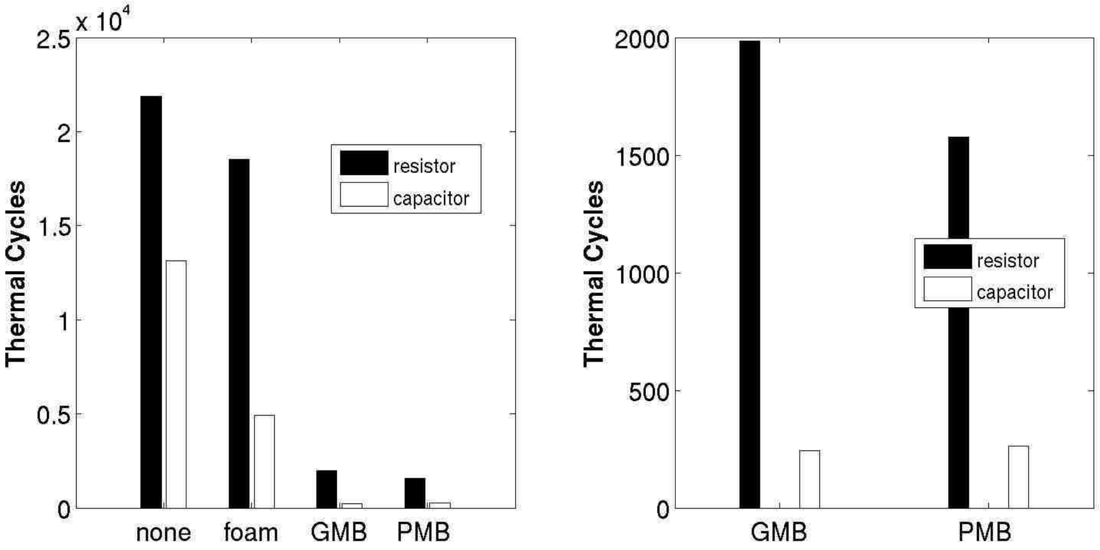

Figure 4-3: Solder thermal fatigue cycles for capacitor and resistor and various over-encapsulation cases.

4.4 Over-encapsulation Discussion

While the solder fatigue life of the capacitor and resistor were reduced by 63% and 15% with the application of a foam encapsulant, the most significant observation from the over-encapsulation study was how much the GMB epoxy over-encapsulation reduced the solder fatigue life. For both the resistor and capacitor, the fatigue lives were reduced by more than 90% by the addition of 828/DEA/GMB epoxy encapsulation. This decrease in solder fatigue life can be explained by the additional strain in the PCB as a result of the epoxy encapsulation. While the CTE's of the FR4 PCB and the ceramic are not that disparate (16.0E-6/°C vs. 10.4E-6/°C), the stiffness is off by an order of magnitude (17.2 GPa vs. 161.0 GPa). As the higher CTE epoxy encapsulation (~35.0E-6/°C) expands and contracts during thermal cycling, it more easily deforms the PCB. This results in increased plastic strain in the solder joints per thermal cycle, i.e. shorter fatigue life. Another observation included a significant increase in the underfill and ceramic stress with the inclusion of an elastomer coating for the capacitor (not as pronounced for the thinner more flexible resistor). The elastomer coating material behavior creates an almost a void-like condition around the capacitor. Combining the above explanation for solder fatigue with this new void-like condition, results in bending of the PCB toward the void. This results in increased localized component stress at the solder joints. These effects were not found to be as prominent with the thinner more flexible resistor, however, they were still observed.

5 Elastomer Coatings

Although the reasons for their use may not fully understood, elastomeric coatings are often used to coat components on PCB's. Common lore indicates that elastomer coatings are helpful for thermal cycling, but can be detrimental during shock and vibration. Typically, elastomeric coatings are used in applications involving epoxy encapsulations, and are sometimes called "stress relief" coatings. While epoxy encapsulation is not the topic of this chapter, the findings from this chapter were useful in the down-selection of the elastomer coating case chosen in Chapter 4.

The four elastomeric coating materials discussed in Section 2.3 were investigated in this study, with the intent of understanding the effect of over-encapsulation on the residual stress state of surface mount components. The capacitor and resistor models described in Chapter 3, and shown in Figure 3-1 and Figure 3-2 were used for the analyses. In all cases, 828/DEA/GMB epoxy over-capsulation was assumed. A summary of the cases Investigated can be seen in Table 5-1. Note that each case was investigated for coating thicknesses of 0.127 mm and 0.508 mm (0.005" and 0.02"). While many underfill material cases were investigated, both the capacitor and resistor described in this section use a 20% FVF hard filled underfill, which should be adequate to identify trends from encapsulation.

Table 5-1: Packaging variations examined for a GMB-filled epoxy encapsulant.

underfills → coatings ↓	no underfill	unfilled epoxy underfill	filled with 10-40 vol% alumina	filled with 10-40 vol% GMB
no coating	X	X	X	X
unfilled silicone	X	X	X	X
GMB filled silicone	X	X	X	X
unfilled polysulfide	X	X	X	X
PMB filled polysulfide	X	X	X	X

For contiguously meshed geometry with 828/DEA/GMB epoxy over-encapsulation, the unfilled elastomeric coatings experienced high tensile stresses during the cool-down of the thermal cycle at the low temperature of -55°C. This was found to be true for both the thick and thin coatings, and for both the capacitor and resistor. The peak values of the calculated maximum principal tensile stresses can be seen in Figure 5-1. In the figure, 0.005 and 0.02 refer to the coating thickness in inches. The calculated maximum principal tensile stresses in the polysulfide ranged from 15 MPa in the 0.005" thick coated capacitor, to 34 MPa in the 0.02" thick coated resistor. The calculated maximum principal tensile stresses in the Sylgard ranged from 20 MPa in the 0.005" thick coated capacitor, to 30 MPa in the 0.02" thick coated resistor. The experimentally determined failure tensile strengths for the unfilled elastomeric coatings in Figure 2-14 of Section 2.3 were found to be on the order of 0.1 to 0.7 MPa. Because these calculated stresses exceed the failure tensile strengths of the materials by an order of magnitude, one could expect that the elastomeric coatings will fail cohesively (polysulfide) or adhesively (Sylgard). This result is consistent with sectioned electronic devices as seen in Figure 5-2, where the unfilled polysulfide in a GMB filled epoxy encapsulated device has failed cohesively.

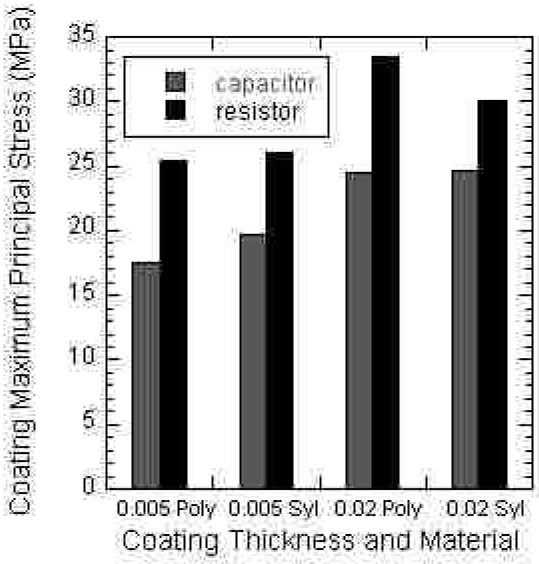

Figure 5-1: Plot of max principal stress in unfilled elastomer coatings for contiguously meshed resistor and capacitor models.

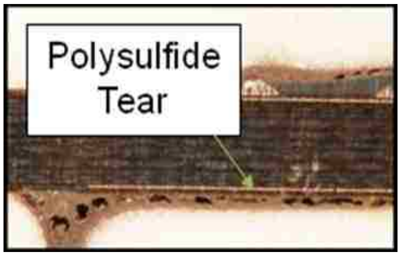

Figure 5-2: Sectioned Electronic Device with cohesively failed, unfilled polysulfide, elastomer coating.

To avoid modeling failure and failure propagation, the elastomer elements in the models were detached from the surrounding epoxy elements, creating a debonded interface. The models were then rerun using this new geometry, and further analysis with unfilled elastomer coatings assume a debonded interface. An image at -55°C depicting the predicted deformed mesh of the debonded elastomer in the resistor model can be seen in Figure 5-3. The model assumes a 0.02" thick elastomer coating.

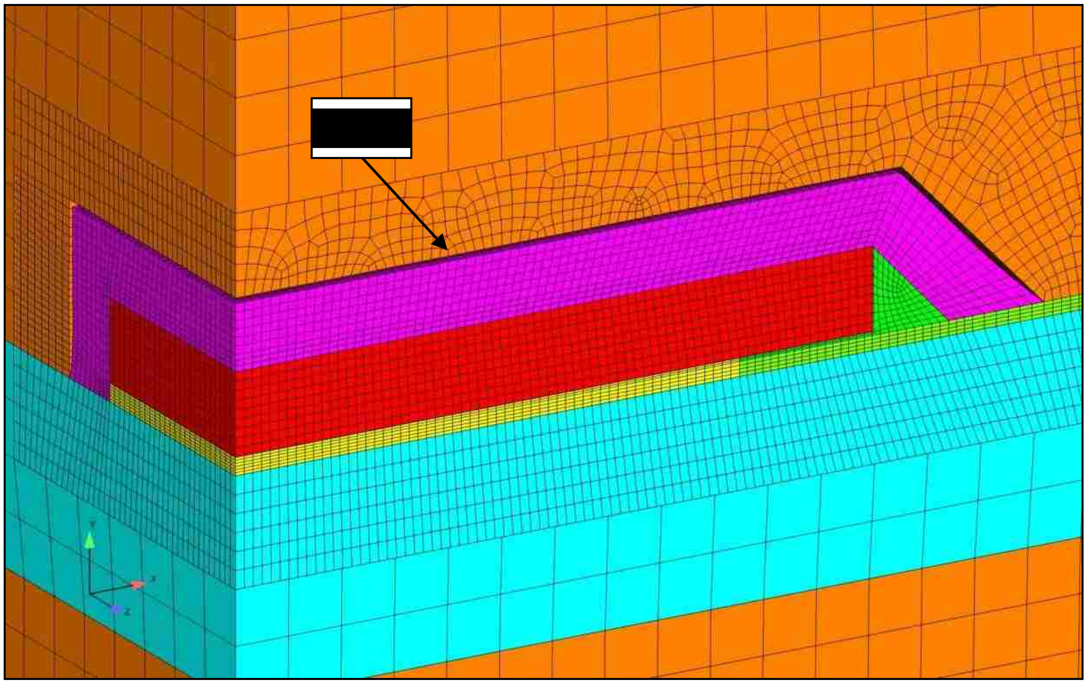

Figure 5-3: Resistor model (1/4 symmetry) with debonded elastomer coating at -55°C.

Because of their significantly lower CTE's and bulk moduli, the filled elastomeric coatings resulted in significantly lower calculated tensile stresses during the cool-down of the thermal cycle. The peak values of the calculated maximum principal tensile stresses for the contiguously meshed geometries can be seen in Figure 5-4. As seen in the figure, the calculated maximum principal tensile stresses in the PMB filled polysulfide ranged from 0.6 MPa for the 0.005” thick coated capacitor to 0.7 MPa for the 0.005” thick coated resistor. The calculated maximum principal tensile stresses in the GMB filled Sylgard ranged from 0.3 MPa for the 0.02” thick coated resistor to 0.8 MPa for the 0.005” thick coated capacitor. As with the unfilled elastomers, the experimentally determined failure tensile strengths for the filled elastomeric coatings in Section 2.3 were found to be on the order of 1 MPa, thus failure of the filled elastomeric coatings was not considered likely, and a contiguous mesh should be a reasonable assumption.

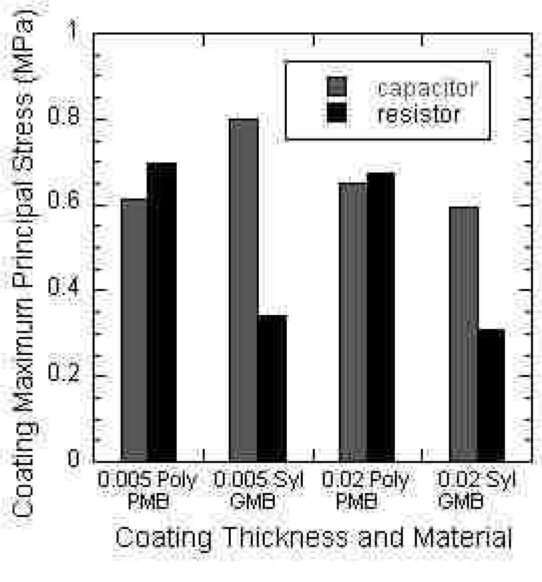

Figure 5-4: Plot of max principal stress in filled elastomer coatings for contiguously meshed resistor and capacitor models

5.1 Elastomeric Coatings and Component Stress

The elastomer coating cases investigated for 828/DEA/GMB epoxy over-encapsulated components included debonded polysulfide and Sylgard and contiguously meshed PMB filled polysulfide and GMB filled Sylgard. The effects of the elastomeric coating on component stresses can be seen in Figure 5-5, where PMB refers to PMB filled polysulfide and GMB to GMB filled Sylgard and 0.005 and 0.02 refer to the coating thickness in inches. In all cases, the capacitor experiences higher stresses than the resistor. This may be explained by the size and stiffness disparity between the components, as the capacitor is larger and stiffer.

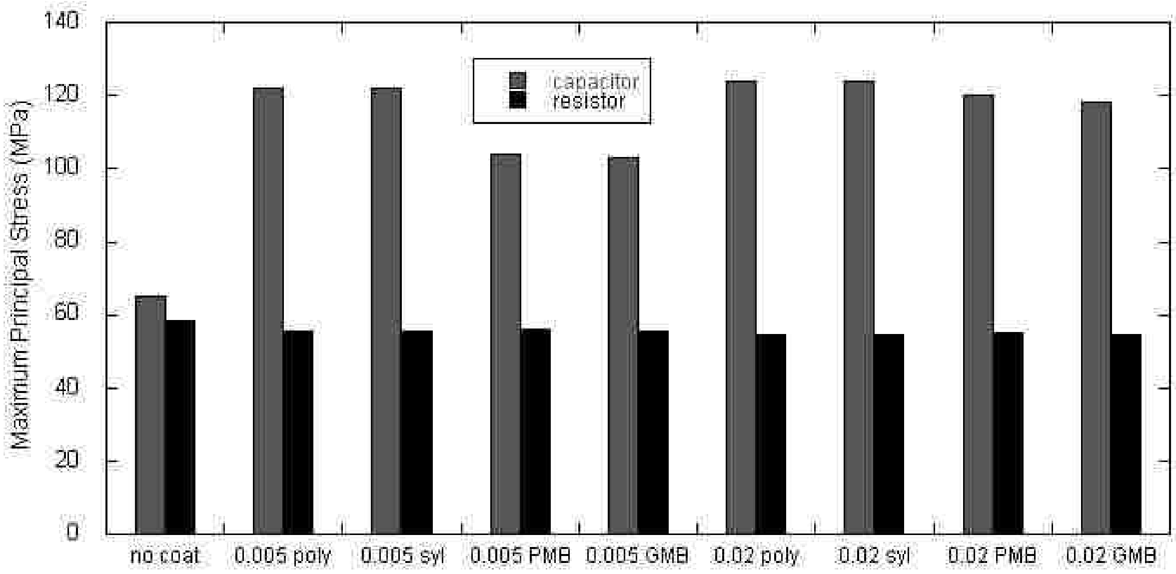

Figure 5-5: Peak ceramic maximum principal stress in capacitor and resistor for various elastomer coating cases with 0.2 hard filler volume fraction in underfill.

As can be seen in the figure, the coatings have little effect on the peak maximum principal tensile stress in the ceramic resistor. The highest resistor stress was calculated to be 58 MPa in the uncoated configuration and ~55 MPa in the coated configurations. A significant stress increase was experienced by the capacitor due to the addition of the coatings (see Section 4.4 for explanation). The uncoated capacitor peak maximum principal stress was calculated to be 65 MPa. The coated ceramic stresses, however, ranged from ~103.5 MPa for the 0.005” thick filled elastomer cases to between 118 and 124 MPa for the other cases. It is worth noting that the capacitor experienced a worst case 92% increase in localized maximum principal stress with the addition of the elastomeric coating, and an 81.5% increase in stress as the best case.

After seeing the significant increase in the ceramic maximum principal stresses in the capacitor by the addition of the elastomeric coatings, one might wonder why a coating would be necessary at all. To investigate further, the average hydrostatic stress in the ceramic for each component was calculated by summing the stress from each element and dividing by the number of ceramic elements. The results are plotted in Figure 5-6.

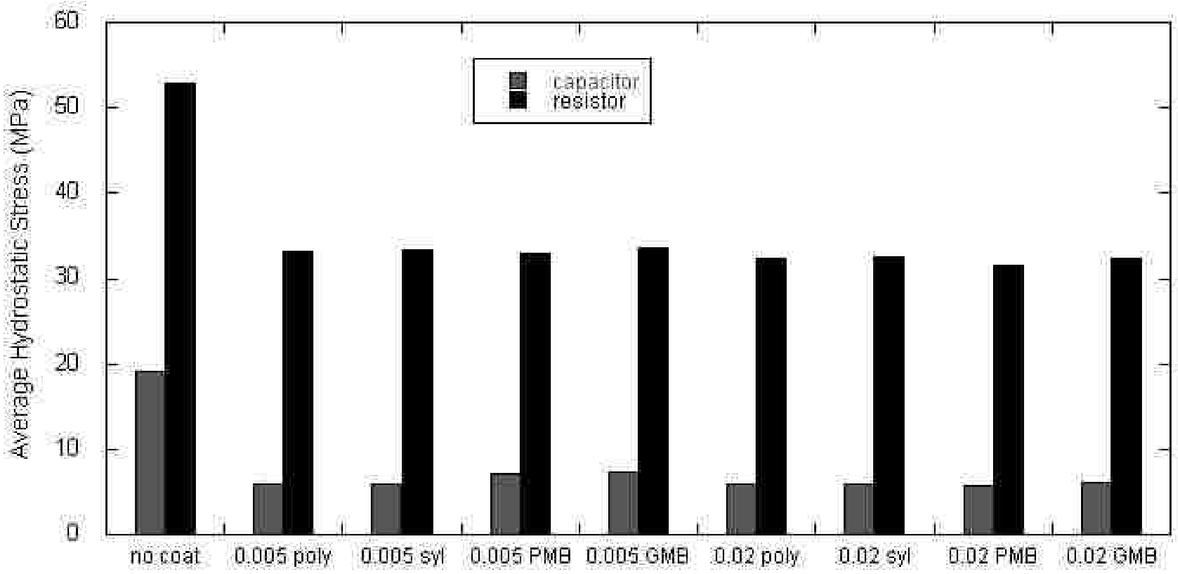

Figure 5-6: Average ceramic hydrostatic stress in capacitor and resistor for various elastomer coating cases with 0.2 hard filler volume fraction.

As can be seen in the figure, the hydrostatic stress is significantly decreased by the addition of the coating. As a consequence, the "stress relief" function is best manifested within this context. The average stress for the capacitor decreased from 19 MPa to 6 MPa, and decreased from 53 MPa to 33 MPa for the resistor. The elastomer coating material and thickness choices do not appear to significantly affect the stresses in the ceramic.

Stress contour plots illustrating the effect of the elastomeric coating can be seen in Figure 5-7. In the figure, the calculated maximum principal stress increases from 65 MPa to 135 MPa with the addition of the coating. The hydrostatic stress at the center of the capacitor, however, decreases from 40 MPa to 4 MPa with the addition of the coating. These results imply that coatings should be applied to components that are sensitive to externally applied loading. In some components, externally applied stress may result in electrical "drift" or even cracking, if the component is hollow.

[redacted] [redacted]

[redacted]

[redacted]

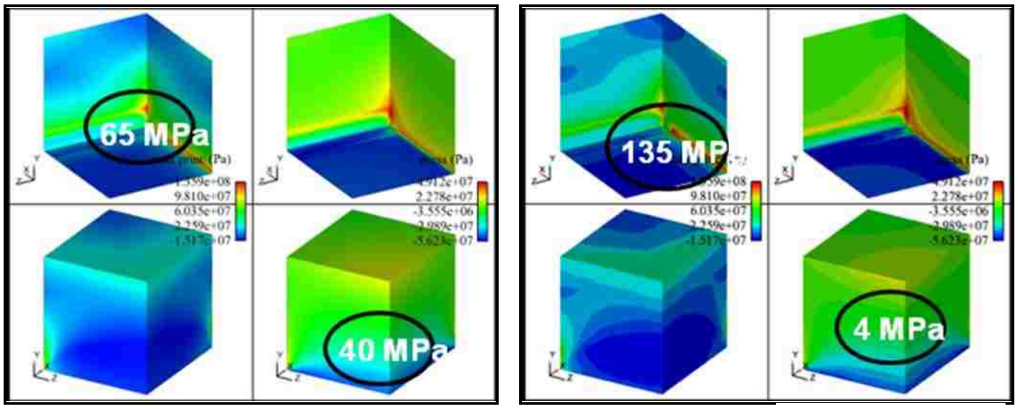

[redacted] [redacted] [redacted] [redacted]

Figure 5-7: Stress contour plots for encapsulated ceramic capacitor with and without elastomeric stress relief coating.

5.2 Elastomeric Coatings and Underfill Stress

The underfill maximum principal stress for epoxy encapsulated components was also studied. Again, 828/DEA/GMB epoxy over-encapsulated components coated with debonded polysulfide and Sylgard and contiguously meshed PMB filled polysulfide and GMB filled Sylgard were assumed. The effects of the elastomeric coatings and thicknesses can be seen in Figure 5-8. In the graph, PMB refers to PMB filled polysulfide and GMB to GMB filled Sylgard and 0.005 and 0.02 refer to the coating thickness in inches.

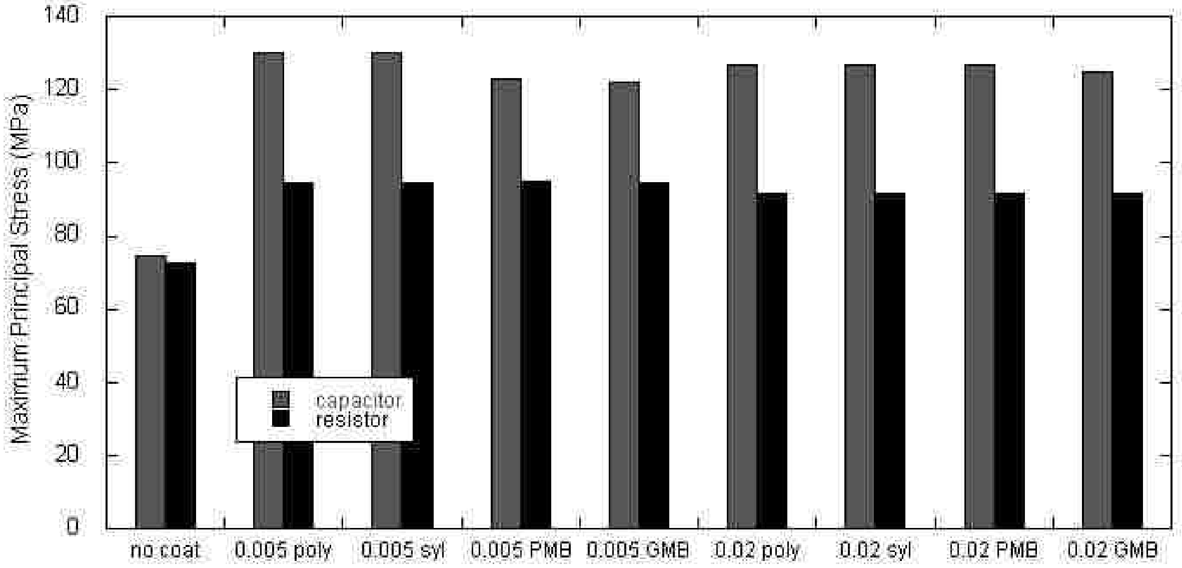

Figure 5-8: Underfill maximum principal stress for epoxy encapsulated capacitor and resistor with various elastomer coating cases and 20% hard filler in the underfill.

As indicated in the figure, coating material and thickness changes did not significantly affect the underfill stress; however, including a coating significantly increased the underfill stress from the uncoated configuration. The peak maximum principal stress in the underfill increased ~70 % from 74.4 MPa to an average of 126 MPa for the capacitor, and 29% from 72.5 MPa to an average of 93 MPa for the resistor (again, see Section 4.4 for explanation).

5.3 Elastomeric Coatings and Solder Fatigue

The effects of elastomer coatings on solder fatigue life for epoxy encapsulated components were also studied. As in the previous section, the elastomer coating cases for 828/DEA/GMB epoxy over-encapsulated components included debonded polysulfide and Sylgard and contiguously meshed PMB filled polysulfide and GMB filled Sylgard.

The thermal-mechanical fatigue life of the solder joints was assessed using the Coffin-Manson fatigue criterion discussed in Section 2.4, and based on the change in plastic strain increment accrued in the eutectic SnPb over a thermal cycle from -55°C to 71°C and back to -55°C. The solder fatigue life is defined as the number of thermal cycles required to initiate a crack in the solder.

The effects of the elastomeric coating can be seen in Figure 5-9, where PMB refers to PMB filled polysulfide and GMB to GMB filled Sylgard and 0.005 and 0.02 refer to the coating thickness in inches. Interestingly, the calculated fatigue lives in all the cases are fairly similar even with the size/stiffness disparity of the components. This indicates that the surrounding epoxy is the dominating factor with respect to solder fatigue life. It is important to note that the underfill thickness assumed for the capacitor in these models was ~0.015”, and the underfill thickness assumed for the resistor was 0.005”. The effect of underfill thickness is examined in Chapter 7.

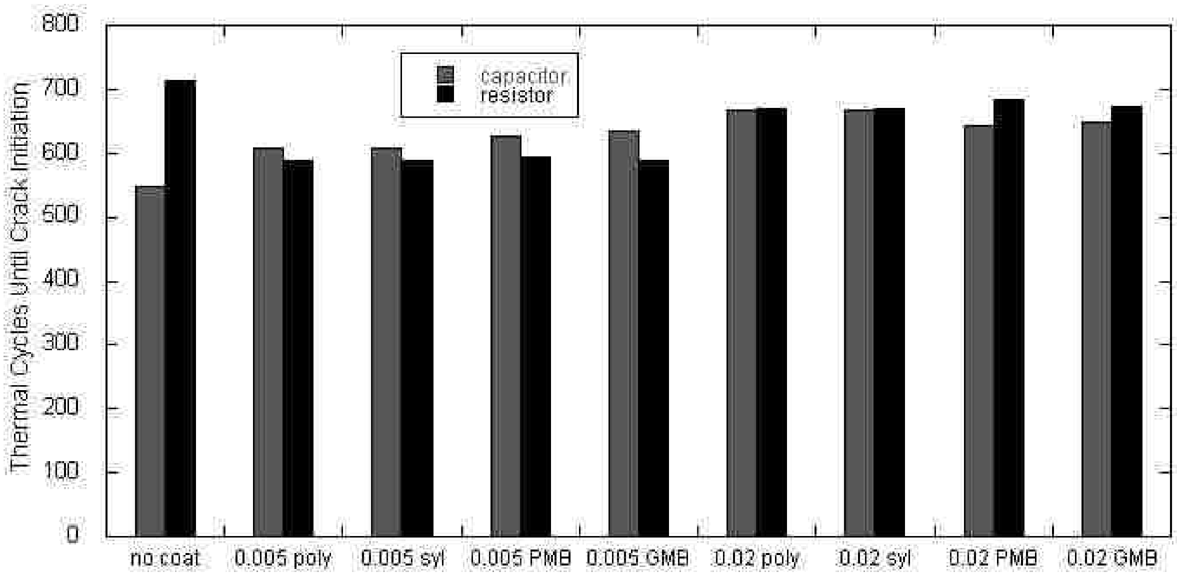

Figure 5-9: Thermal cycles until solder crack initiation for epoxy encapsulated capacitor and resistor with various elastomer coating cases and 20% hard filler in the underfill.

As can be seen in the figure, the coatings have a minimal effect on the calculated fatigue life in either the capacitor or resistor. For the capacitor, the highest fatigue life was calculated to be 549 cycles in the uncoated configuration and 668 cycles in the coated configurations. The minimum coated capacitor fatigue life was calculated to be 609 cycles. The highest fatigue life for the resistor was calculated to be 714 cycles for the uncoated configuration and 684 cycles in the coated configurations, and the minimum fatigue life was calculated to be 588 cycles. It is interesting to note that the addition of the elastomer coatings increased the fatigue life of the capacitor by as much as 22%, but decreased the life of the resistor by as much as 18%.

5.4 Elastomeric Coatings Results Discussion

Four elastomer coatings were investigated: unfilled Sylgard, GMB filled Sylgard, polysulfide, and PMB filled polysulfide. The stresses experienced by the unfilled elastomer coatings when over-encapsulated by an epoxy will likely result in tearing or debonding of the coating (important for finite element model boundary conditions). The filled elastomer coatings probably will not tear or debond. The application of the elastomer coating to the large encapsulated capacitor resulted in a significant reduction of hydrostatic stress in the ceramic. The cost, however, was a large increase in the localized ceramic stress at the solder joints. The elastomer coating had a minimal impact on the solder fatigue life of either the resistor or capacitor, but did result in an increase in the underfill stress.

6 Underfill Filler Volume Fraction

The intent of this study was not to predict quantitatively the onset of failure in these materials, but to identify "trends" that will lead to reductions in residual stress, enhance solder thermal fatigue life, and increase margins for components subjected to harsh dynamic environments.

6.1 Underfill Filler Volume Fraction and Component Stress

6.1.1 *No Encapsulant / Foam Encapsulant*

The stress results for the unencapsulated capacitor and resistor are plotted in Figure 6-1. In the left plot of the figure, it can be seen that the addition of an unfilled underfill to the unencapsulated capacitor significantly decreases the peak maximum principal stress from 73 MPa to 57 MPa. Adding filler to the underfill, however, linearly increased the stress to 63 MPa for hard filled and 61 MPa for GMB filled underfills. An opposite trend was experienced by the resistor. As seen in the right plot of Figure 6-1, the resistor stress increased from 50.8 MPa to 57.5 MPa with the addition of an unfilled underfill, but monotonically decreased with addition of filler to 52.4 MPa for a 40% FVF hard filled underfill and to 53.9 MPa for a 40% FVF GMB filled underfill.

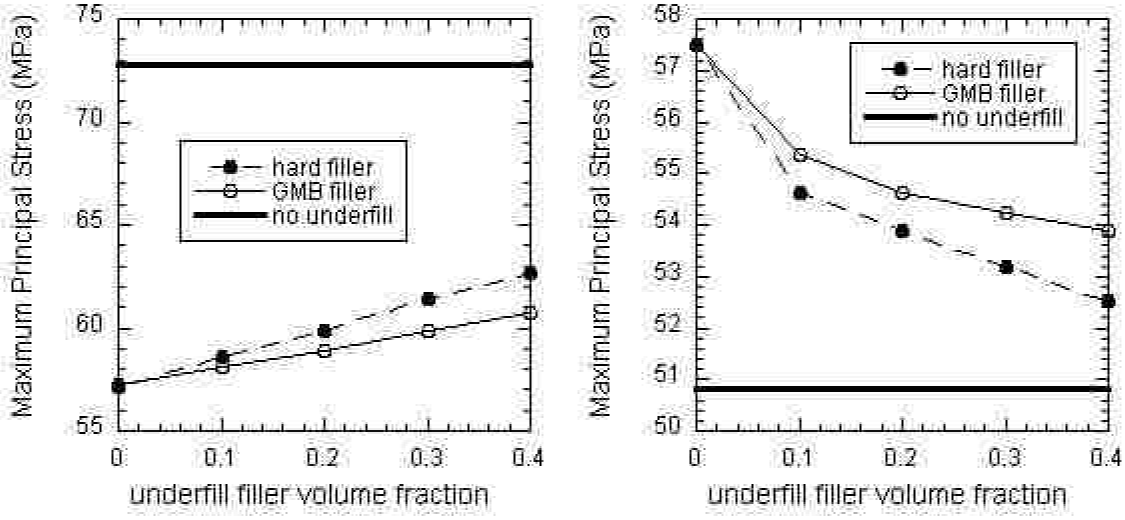

Figure 6-1: Ceramic maximum principal stress vs. underfill FVF for unencapsulated capacitor (left) and resistor (right).

Plots of the peak maximum principal stresses in the capacitor and resistor for the foam encapsulated cases can be seen in Figure 6-2. The ceramic stress results from the foam encapsulated and unencapsulated components are fairly similar. The capacitor experienced a decrease in stress from 63.3 MPa to 53.7 MPa with the addition of an unfilled underfill, but a linear increase in stress from 53.7 MPa to 57.9 MPa with the addition of 40% FVF GMB, and an increase to 61.0 MPa with the addition of 40% hard filler. The resistor (right, Figure 6-2) experienced an increase in stress from 49.3 MPa to 53.4 MPa with the addition of an unfilled underfill, but a decrease in stress from 53.4 MPa to 51.0 MPa with the addition of 40% FVF GMB, and a decrease to 49.6 MPa with the addition of 40% hard filler.

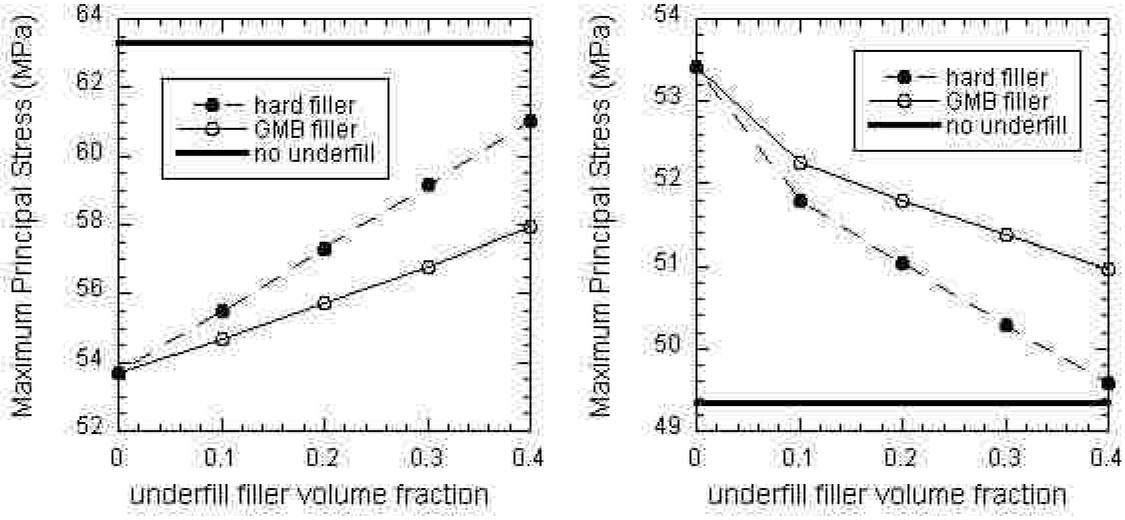

Figure 6-2: Ceramic maximum principal stress vs. underfill FVF for foam encapsulated capacitor (left) and resistor (right).

6.1.2 *Epoxy Encapsulant*

The effect on peak maximum principal stress in the ceramic components for various underfill filler volume fractions can be seen in Figure 6-3 for the uncoated, epoxy encapsulated components. As seen in the figure, some “trends” may be identified. For both the resistor and capacitor, adding GMB filler to the underfill almost linearly reduced the ceramic stress. The capacitor peak maximum principal stress was reduced from 61.3 MPa to 55.2 MPa, and the resistor peak stress was reduced from 62.4 MPa to 60.2 MPa with the addition of 40% GMB filler. The solid hard filler results were more complicated. The addition of hard filler to the capacitor increased the ceramic stress from 61.3 MPa to 72.9 MPa, while adding hard filler to the resistor decreased the stress from 62.4 MPa to 55.9 MPa. The addition of GMB filler to the underfill reduces the underfill CTE but only slightly changes the moduli, resulting in lower thermal stress. Adding hard filler reduces the CTE, but increases the moduli. This coupled with the stiffer capacitor geometry results in a higher stress state. The loss of stiffness produced by the absence of underfill increases the resistor stresses noticeably.

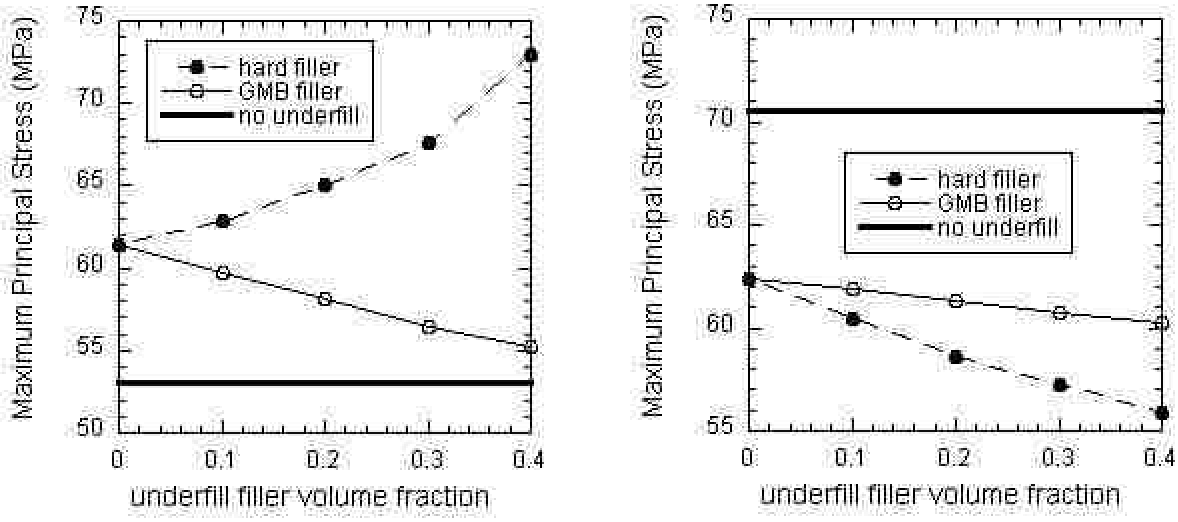

Figure 6-3: Ceramic maximum principal stress vs. underfill FVF for GMB epoxy encapsulated capacitor (left) and resistor (right).

Changes in the peak maximum principal stress for the capacitor and resistor due to the addition of an underfill and filler are depicted in Figure 6-4 for elastomer coated, epoxy encapsulated components. Results were calculated for a variety of various elastomer coating cases; however, PMB polysulfide is the only coating presented in the plots. The results from the debonded unfilled elastomer coatings and GMB filled Sylgard were found to be very similar to those of the PMB polysulfide, and “trends” due to coating thickness were found to be similar (See Chapter 5).

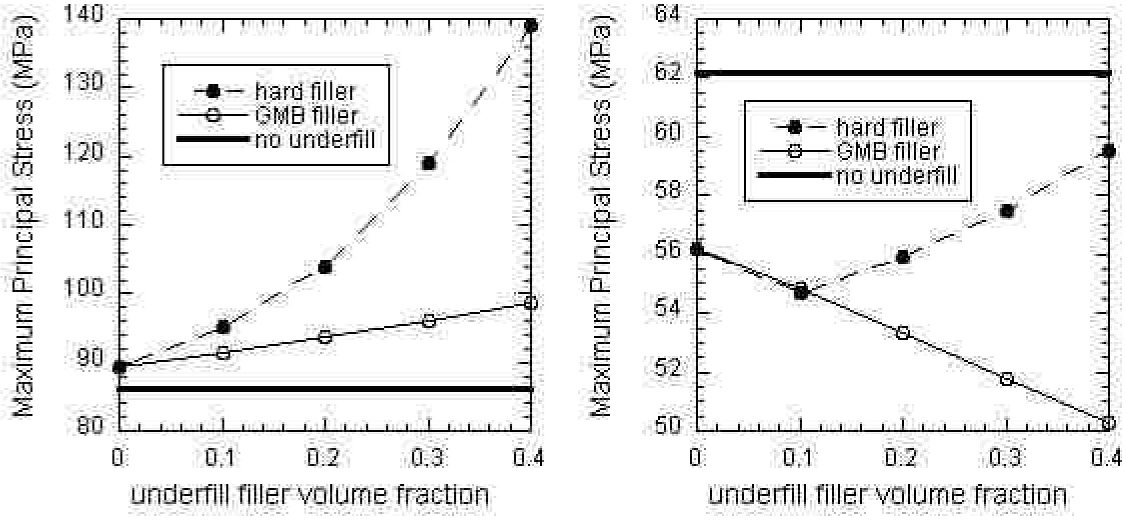

Figure 6-4: Ceramic maximum principal stress vs. underfill FVF for elastomer coated, GMB epoxy encapsulated capacitor (left) and resistor (right).

As seen in the figures, “trends” are not necessarily obvious. One unusual trend in the resistor data is the decrease in stress from the unfilled case to the 10% hard filled case followed by a consistent increase in stress with the addition of more hard filler. This indicates an optimum hard filler volume fraction of 10% for this particular geometry and encapsulation state. Other such optimums can be identified by further analyses involving other over-encapsulated and unencapsulated states. Another unusual observation is that for the capacitor, the addition of filler to the underfill in all cases with the elastomer coating increases the component stress. With the resistor, however, the addition of GMB filler decreases the stress in the ceramic component. The opposite trends lead one to believe that “general” design guides with respect to optimizing underfill filler volume fraction may not exist, and that details likely matter.

Adding an underfill to the resistor, decreased the peak maximum principal stress from 62 MPa to as low as 50 MPa for the 40% FVF GMB case with the thin coating (Figure 6-4, right). The capacitor, however, had more mixed results. The addition of underfill resulted consistently in higher stress with the thin coating, the best case being an increase from 86 MPa to 89 MPa for the unfilled underfill, and the worst case being an increase to 140 MPa for the 40% FVF solid hard underfill (Figure 6-4, left).

6.2 Underfill Filler Volume Fraction and Underfill Stress

6.2.1 *No Encapsulant / Foam Encapsulant*

Because the results for the foam encapsulation case were very similar, only the unencapsulated case is discussed. The predicted underfill maximum principal stress for the unencapsulated capacitor and resistor due to the addition of an underfill and filler are depicted in Figure 6-5. In all cases, adding any filler to the underfill almost linearly decreases the underfill stress. Adding 40% FVF solid hard filler to the capacitor underfill decreased the stress from 62.7MPa to 55.5 MPa, or 11.5%, while adding 40% FVF GMB filler to the underfill decreased the stress by 30.6% to 43.5 MPa (Figure 6-5, left). The trends were almost identical for the resistor. By adding 40% FVF solid hard filler to the resistor underfill, the maximum principal stress decreased 11.2% from 63.4 MPa to

56.3 MPa, while adding 40% FVF GMB filler to the underfill decreased the stress by 32.5% to 42.8 MPa (Figure 6-5, right).

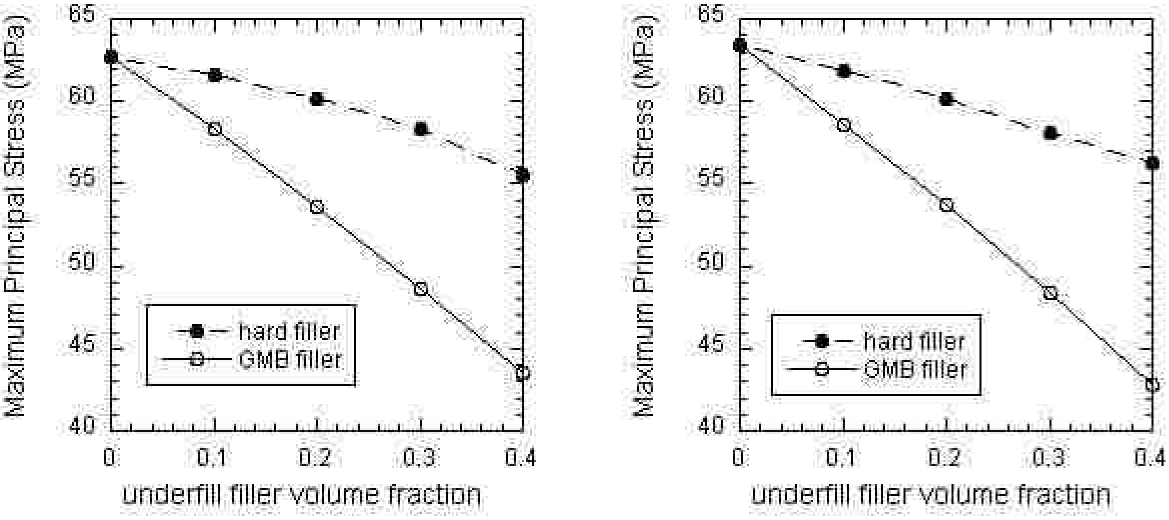

Figure 6-5: Underfill maximum principal stress vs. underfill FVF for unencapsulated capacitor (left) and resistor (right) with no coating.

6.2.2 *Epoxy Encapsulant*

The effect on peak maximum principal stress in the underfill for various underfill filler volume fractions can be seen in Figure 6-6 for the uncoated, epoxy encapsulated components. Again, some “trends” may be identified from the figure. For both the resistor and capacitor, adding GMB filler to the underfill almost linearly reduced the underfill stress. The capacitor peak maximum principal stress was reduced 31% from 64.2 MPa to 44.2 MPa, and the resistor peak stress was reduced 35% from 65.6 MPa to 42.6 MPa with the addition of 40% GMB filler. The solid hard filler results indicated an opposite trend. The addition of hard filler to the capacitor increased the ceramic stress 55% from 64.2 MPa to 99.5 MPa, while adding hard filler to the resistor decreased the stress 26% from 65.6 MPa to 82.9 MPa. These results are very similar to those for the ceramic component stresses, and the explanation in Section 6.1.2 applies.

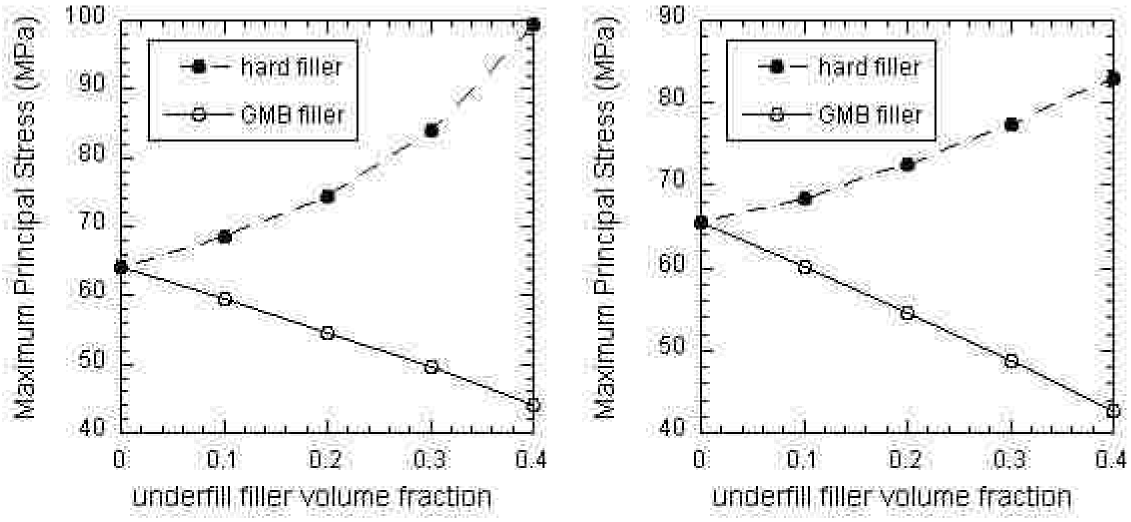

Figure 6-6: Underfill maximum principal stress vs. underfill FVF for GMB epoxy encapsulated capacitor (left) and resistor (right).

The predicted underfill maximum principal stress for the poly PMB coated, epoxy encapsulated capacitor and resistor as a function of underfill filler volume fraction can be seen in Figure 6-7. As in previous sections, only the 0.005" thick PMB polysulfide coating cases are presented in the plots because the results were similar for the various coating cases.

As seen in the figures, obvious “trends” appear. In all cases adding GMB filler to the underfill linearly decreased the underfill stress while adding solid hard filler monotonically increased the stress. Adding 40% FVF solid hard filler to the capacitor underfill increased the stress from 98.8 MPa to 158 MPa, or 60%, while adding 40% FVF GMB filler to the underfill decreased the stress by 16% to 82.6 MPa (Figure 6-7, left). The trends were similar for the resistor. By adding 40% FVF solid hard filler to the resistor underfill, the maximum principal stress increased 33% from 83.0 MPa to 110 MPa, while adding 40% FVF GMB filler to the underfill decreased the stress by 23% to 61.8 MPa (Figure 6-7, right).

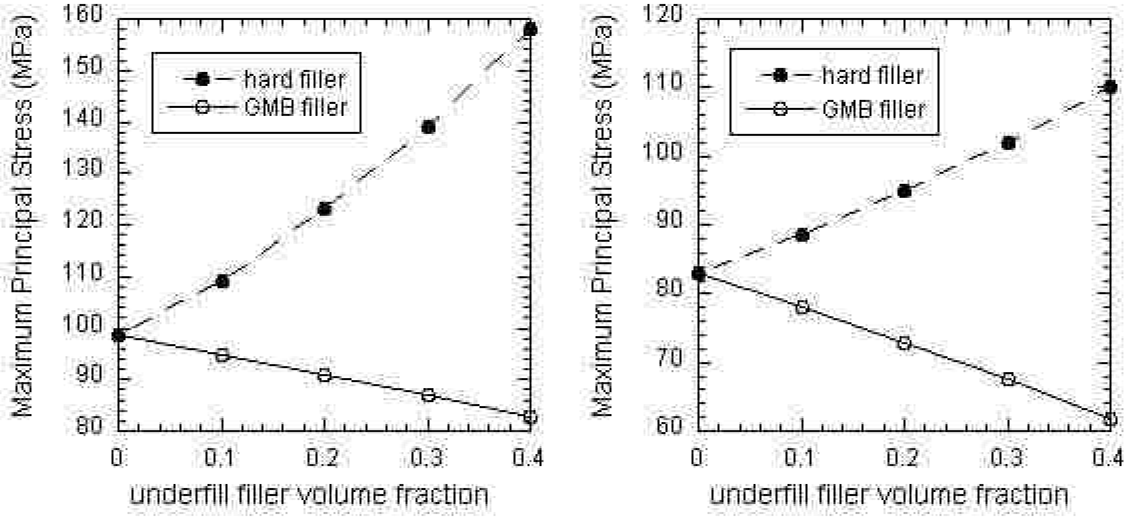

Figure 6-7: Underfill maximum principal stress vs. underfill FVF for elastomer coated, GMB epoxy encapsulated capacitor (left) and resistor (right).

6.3 Underfill Filler Volume Fraction and Solder Fatigue

6.3.1 *No Encapsulant / Foam Encapsulant*

The predicted solder fatigue lives for the unencapsulated and foam encapsulated components are plotted in Figure 6-8 and Figure 6-9 for a range of underfill filler volume fractions. Like the 828/DEA/GMB epoxy encapsulated components, design “trends” for generic unencapsulated and foam encapsulated components may be identified with respect to solder fatigue life.

In each figure, the addition of an unfilled underfill reduced the fatigue life from the no underfill case. The largest decrease in fatigue life was a 44% drop from 6,236 cycles to 3,496 cycles for the foam encapsulated resistor (Figure 6-9, right) with the addition of the unfilled underfill, and the smallest decrease was experienced by the foam encapsulated capacitor, with a 33% drop from 6,628 cycles to 4,456 cycles (Figure 6-9, left). The addition of GMB to the underfill consistently increased the fatigue life. In the best case, the fatigue life for the unencapsulated capacitor (Figure 6-8, left) was increased from 10,556 cycles by 187% to 30,355 cycles with the addition of 40% FVF GMB to the underfill, and the worst cases improvement was an 89% increase from 4,461 cycles to 8,712 cycles for the unencapsulated resistor (Figure 6-8, right) with 40% FVF GMB in the underfill. The addition of solid hard filler to the underfill increased the fatigue life to a point, after which addition of more filler reduces the fatigue life. 20% to 30% FVF hard filler appears to be the optimum. The best improvement from hard filler was achieved by the unencapsulated capacitor (Figure 6-8, left) by adding 20% FVF hard filler to increase the fatigue life by 151% from 10,566 cycles to 26,513 cycles. The smallest improvement was obtained by the unencapsulated resistor (Figure 6-8, right) by adding 20% FVF hard filler to increase the fatigue life by 89% from 4,459 cycles to 8,405 cycles.

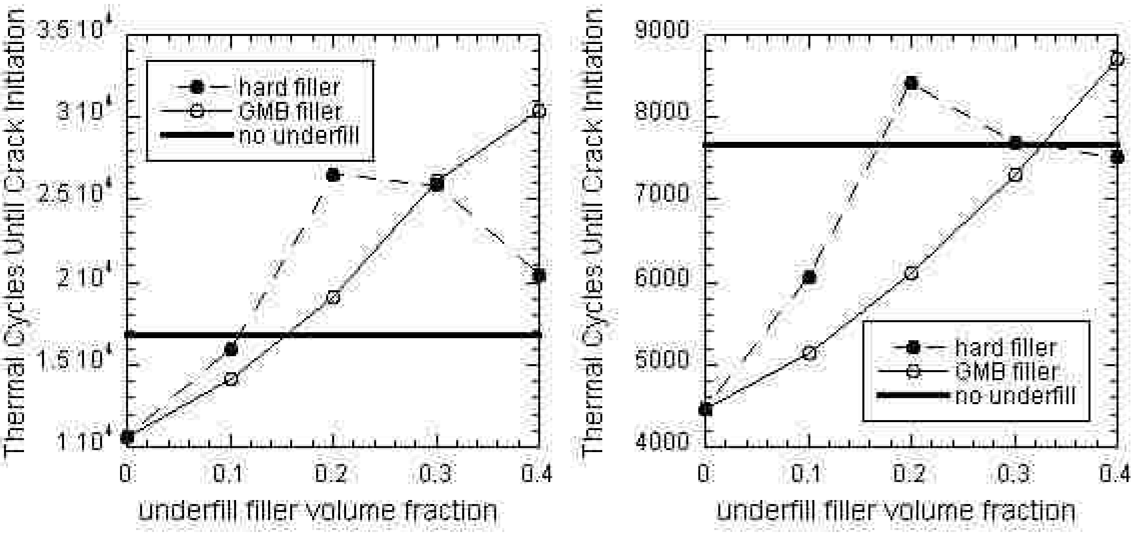

Figure 6-8: Thermal cycles until solder crack initiation vs. underfill FVF for unencapsulated capacitor (left) and resistor (right).

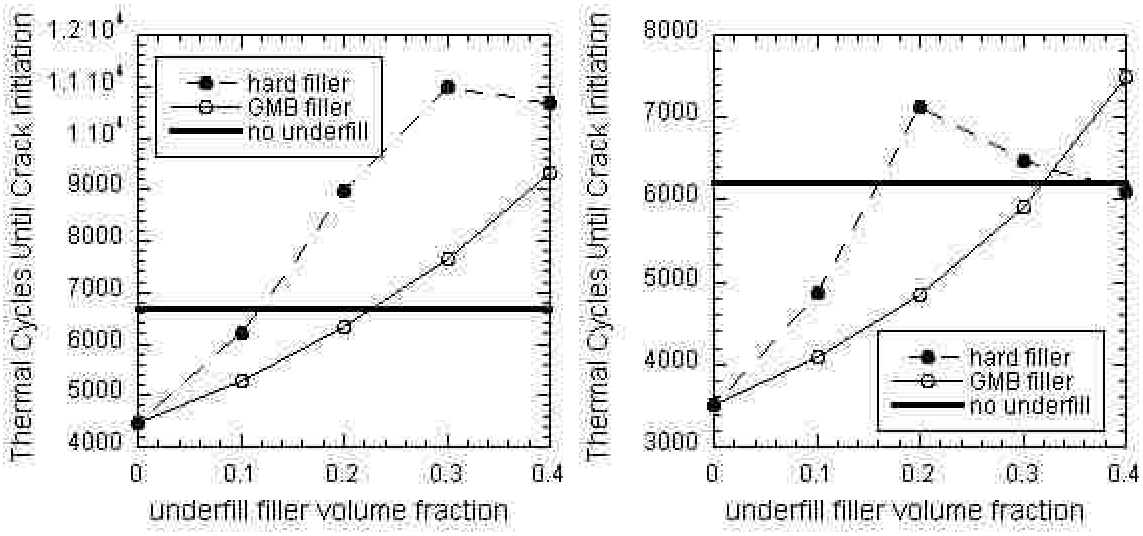

Figure 6-9: Thermal cycles until solder crack initiation vs. underfill FVF for foam encapsulated capacitor (left) and resistor (right).

6.3.2 *Epoxy Encapsulant*

The effect of underfill filler volume fraction on solder fatigue for the epoxy encapsulated capacitor (left) and resistor (right) with no elastomer coating can be seen in Figure 6-10. One obvious “trend” can immediately be identified in the figure. A void under the component significantly reduces the fatigue life. By adding an unfilled underfill, the fatigue life for the capacitor was increased by 177% from 181 cycles to 501 cycles, and the fatigue life for the resistor was increased by 73% from 328 cycles to 566 cycles. The addition of hard filler linearly increased the fatigue life by another 21% with an increase to 609 cycles with 40% FVF, but the addition of GMB filler to the capacitor underfill had almost no effect on the fatigue life. The resistor, however, experienced an increase in fatigue life with the addition of any filler to the underfill. The addition of

40% FVF solid hard filler increased the fatigue life by 37% from 566 cycles to 773 cycles, and the addition of 40% FVF GMB increased the fatigue life by 22% to 690 cycles.

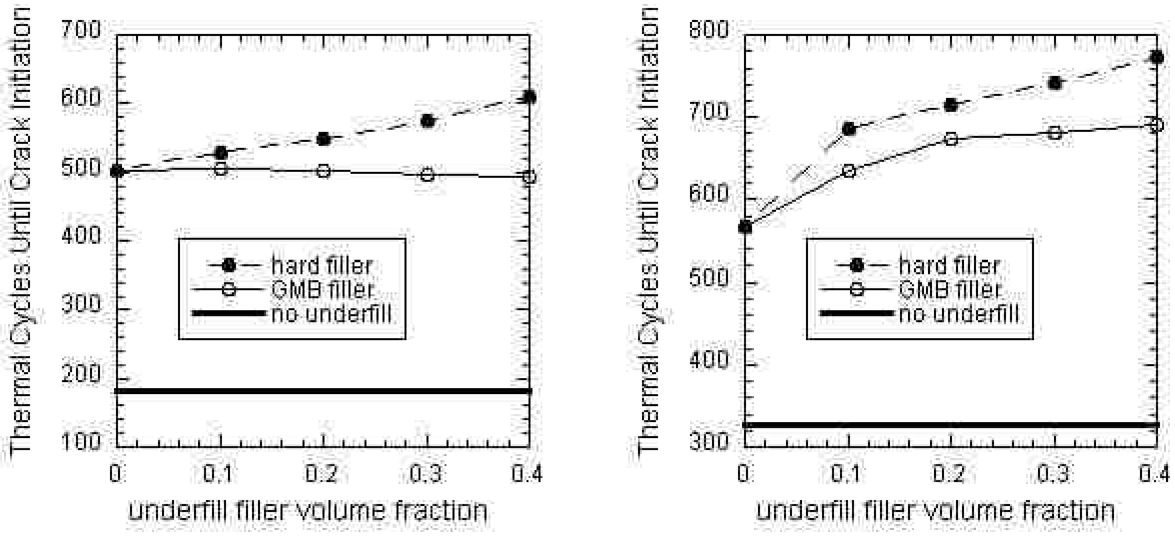

Figure 6-10: Thermal cycles until solder crack initiation vs. underfill FVF for GMB epoxy encapsulated capacitor (left) and resistor (right).

The predicted fatigue lives for the epoxy encapsulated, elastomer coated capacitor and resistor due to the addition of an underfill and filler are depicted in Figure 6-11. As in previous sections, the results from the debonded unfilled elastomer coatings and GMB filled Sylgard were very similar to those of the PMB polysulfide, thus PMB polysulfide was the only coating case presented in the plots.

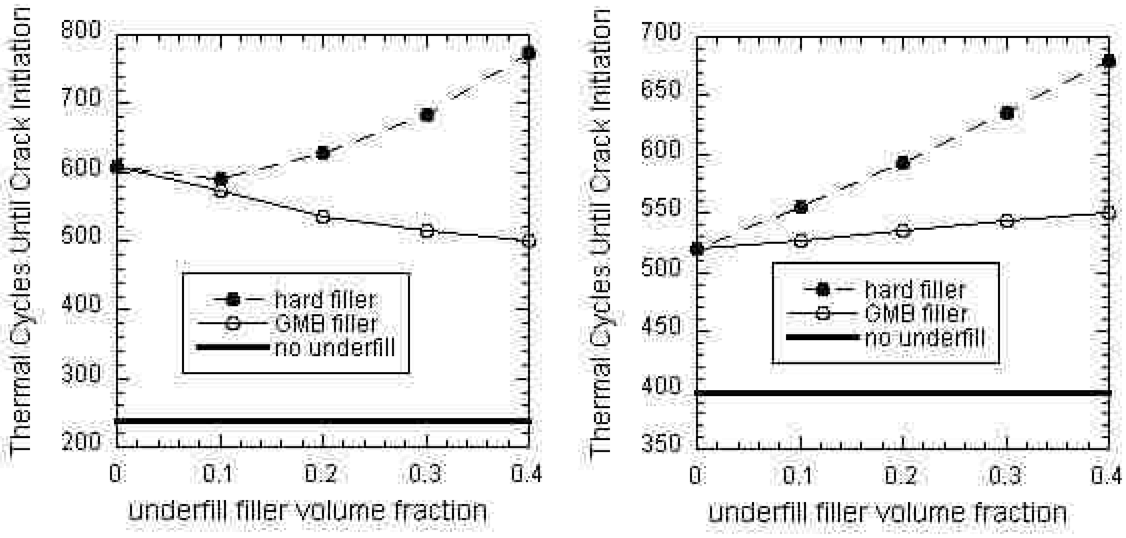

Figure 6-11: Thermal cycles until solder crack initiation vs. underfill FVF for elastomer coated, GMB epoxy encapsulated capacitor (left) and resistor (right).

As seen in the figures, some “trends” may be identified. In all of the cases, adding even an unfilled underfill increased the fatigue life, with the best case demonstrating an improvement from 239 cycles to 609 cycles for the capacitor, and a worst case improvement from 399 cycles to 538 cycles for the resistor. Note that the “no underfill” case assumes a void under the component.

For both the capacitor and resistor, increasing the hard filler volume fraction increased the fatigue life. Increasing the GMB filler volume fraction slightly increased the fatigue life for the resistor, but slightly decreased the fatigue life of the capacitor. The resistor fatigue life increase for both cases was linear with the addition of underfill filler (Figure 6-11, right). By adding 40% FVF hard filler, a 30% increase in fatigue life was realized, while the addition of 40% GMB filler resulted in a 6% increase in fatigue life. The capacitor results were slightly more complicated. While the fatigue life increased with the addition of solid hard filler (with the exception of 10% FVF), the increase was not linear with respect to the filler fraction. The capacitor ultimately achieved a 27% increase in fatigue life as the solid hard filler was increased to 40% FVF, but the addition of 40% GMB filler to the underfill resulted in an almost linear 18% decrease in fatigue life for the capacitor (Figure 6-11, left).

6.4 Underfill Filler Volume Fraction Results Discussion

For 828/DEA/GMB epoxy encapsulated components, adding an underfill significantly increased solder fatigue life over the void condition. Adding hard filler to the underfill significantly increased the ceramic stress for the elastomer coated capacitor, but the stress increase was not as dramatic in the uncoated case. Increasing the filler volume fraction (FVF) of hard filler improved the solder fatigue life of epoxy encapsulated components, but GMB had a minimal effect. Increasing the hard FVF in the underfill increased the underfill stress, and increasing the GMB FVF in the underfill decreased the underfill stress.

For unencapsulated/foam encapsulated components, optimal filler volume fractions in underfills were observed for solder fatigue. One such value that stood out was 20% FVF hard filler. In some cases, it was found that adding filler to the underfill could increase or decrease the solder fatigue life, and it was also noted that adding an underfill could result in opposite trends depending on the component geometry (capacitor or resistor). Adding underfill to the capacitor slightly decreased ceramic stress, while adding underfill to the resistor slightly increased ceramic stress, but in both cases, adding filler moved the stresses toward the no underfill stress state. Given some of these opposite trends, these non-intuitive results really emphasize the benefit of modeling.

Addition al results for the unencapsulated resistor and capacitor were published by Neidigk and Shen [56].

7 Underfill Thickness

Another goal for this research effort was to computationally investigate the effect of surface mount component underfill thickness, as variations in manufacturing processes can result in components being different heights off of the PCB. Using quasi-static, thermal stress, finite element models, these variations were investigated with the intent of understanding how they affect component stress, solder fatigue life, and stress in the polymer underfill. Additional variables included in the calculations were underfill filler volume fraction, elastomer coating, and over-encapsulation. As in previous sections, the intent of this study is not to predict quantitatively the onset of failure in these materials, but to identify “trends” that will lead to reductions in residual stress, enhance solder thermal fatigue life, and increase margins for components subjected to harsh dynamic environments.

Surface mount component finite element models similar to those used in previous investigations were also used for the underfill thickness study. Because the components vary in height off the PCB, a new mesh was constructed for each underfill thickness case. As in previous studies, these components were chosen because they represent very different component geometries with respect to stiffness. The ceramic “small” resistor and “large” capacitor, over-encapsulated and soldered to circuit boards can be seen in Figure 3-1 and Figure 3-2. Both models include underfill and an optional elastomer conformal coating. The geometry was based on actual cross-sectioned electrical components. The various encapsulation/underfill/coating cases investigated are summarized in Table 7-1. For each case shown in the table, the component height off the PCB was varied from 0.003” to 0.009” in 0.001” increments.

Table 7-1: Packaging variations modeled for underfill thickness study.

Underfills → **Encapsulation ↓**	**No Underfill**	**Unfilled Epoxy Underfill**	**Filled with 10-40 vol% Alumina**	**Filled with 10-40 vol% GMB**
No Encapsulation	X	X	X	X
GMB-Epoxy Encapsulation no Coating		X	X	X
GMB-Epoxy Encapsulation with 0.005” Polysulfide Filled with PMB		X	X	X
20# Foam Encapsulation no Coating		X	X	X

Component stress, underfill stress, and thermal solder fatigue are investigated as functions of underfill thickness for various encapsulation cases in the following sections. While a full study was performed involving underfill filler fractions ranging from unfilled to 40% filled, to reduce complexity, the plots in the following sections only depict the results for the 20% filled underfill cases.

7.1 Underfill Thickness and Component Stress

7.1.1 *No Encapsulant / Foam Encapsulant*

As shown in Figure 7-1 and Figure 7-2, the stress results for the unencapsulated and foam encapsulated components were very similar, thus the following discussion is applicable to both cases.

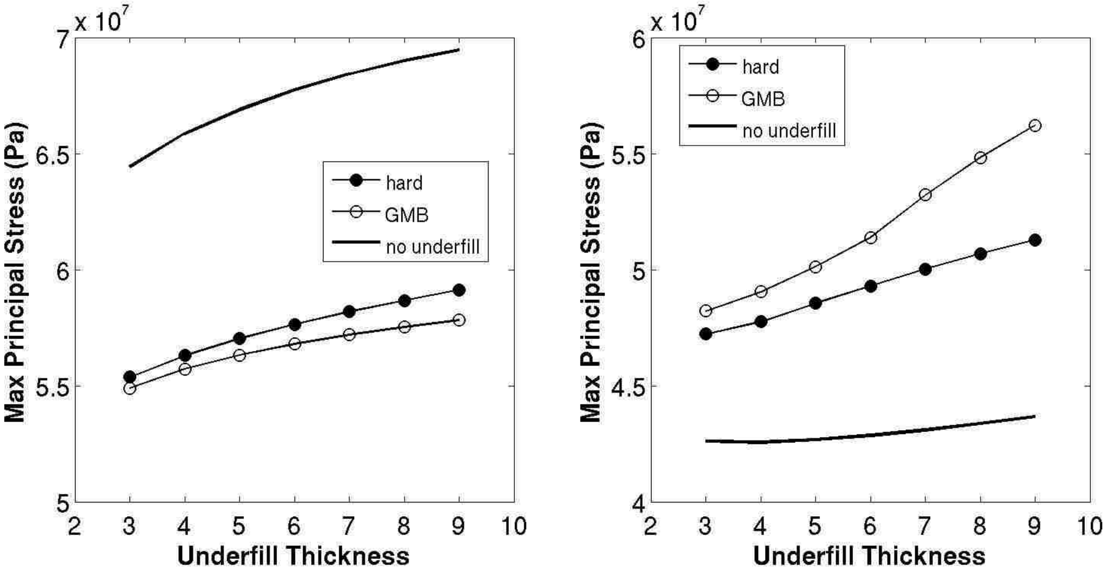

Figure 7-1: Ceramic maximum principal stress vs. underfill thickness for unencapsulated capacitor (left) and resistor (right) with 20% FVF solid and GMB underfills.

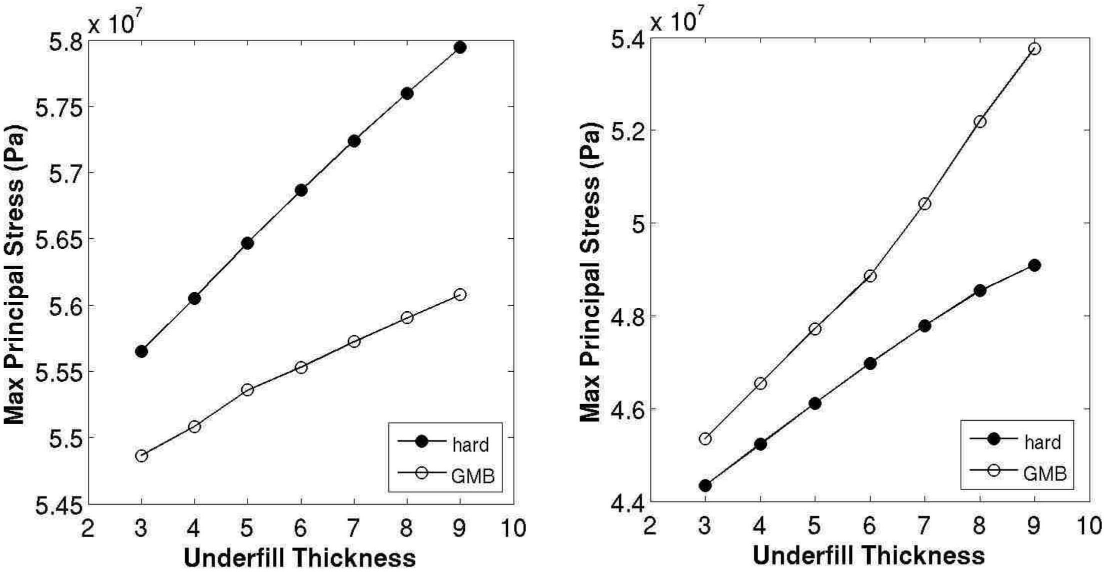

Figure 7-2: Ceramic maximum principal stress vs. underfill thickness for foam encapsulated capacitor (left) and resistor (right) with 20% FVF solid and GMB underfills.

As demonstrated in Chapter 4, the unencapsulated capacitor experienced a decrease in stress with the addition of an underfill, while the resistor experienced an increase in stress. For both cases, however, the capacitor and resistor experienced an increase in stress as the component height from the board was increased.

For the no underfill case, the capacitor maximum principal stress increased monotonically from 64.4 MPa to 69.5 MPa, or 7.9%, as the component height from the board was increased from 0.003” to 0.009” (Figure 7-1, left). The resistor without an underfill also experienced a 2.6% increase in stress from 42.6 MPa to 43.7 MPa as the height from the board was increased to 0.009” (Figure 7-1, right).

Increasing the 20% solid hard filled underfill thickness resulted in an increase in stress from 55.4 MPa to 59.1 MPa, or 6.7%, for the capacitor (Figure 7-1, left), and a 8.5% increase in stress from 47.2 MPa to 51.2 MPa for the resistor (Figure 7-1, right). An increase in underfill thickness for the 20% GMB filled underfill resulted in a 5.3% stress increase from 54.9 MPa to 57.8 MPa for the capacitor (Figure 7-1, left), and a 17% increase in stress from 48.2 MPa to 56.2 MPa for the resistor (Figure 7-1, right).

7.1.2 *Epoxy Encapsulant*

The effect on peak maximum principal stress in the ceramic for various underfill thicknesses can be seen in Figure 7-3 for the uncoated, epoxy encapsulated components. At first glance, the capacitor results (Figure 7-3, left) look odd, however, further investigation of the model, confirmed the result. With an underfill thickness increase from 0.003” to 0.004”, the stress in the capacitor increased from 59.6 MPa to 63.9 MPa for the 20% solid hard filled underfill, and from 55.2 MPa to 59.1 MPa for the 20% GMB filled underfill. These results constituted a stress increase of ~7%, while an underfill thickness increase from 0.004” to 0.009”, resulted in a stress decrease of 0.6 % from 63.9 MPa to 63.5 MPa for the 20% solid hard filler, and 4.2% from 59.1 MPa to 56.6 MPa for the 20% GMB filled underfill. For the resistor (Figure 7-3, right), an underfill thickness increase from 0.003” to 0.009” resulted in ceramic stress increase of ~34% for both underfill cases, as the 20% solid hard filled underfill case stress increased from 36.9 MPa to 49.5 MPa, and the 20% GMB filled underfill case stress increased from 37.9 MPa to 49.8 MPa.

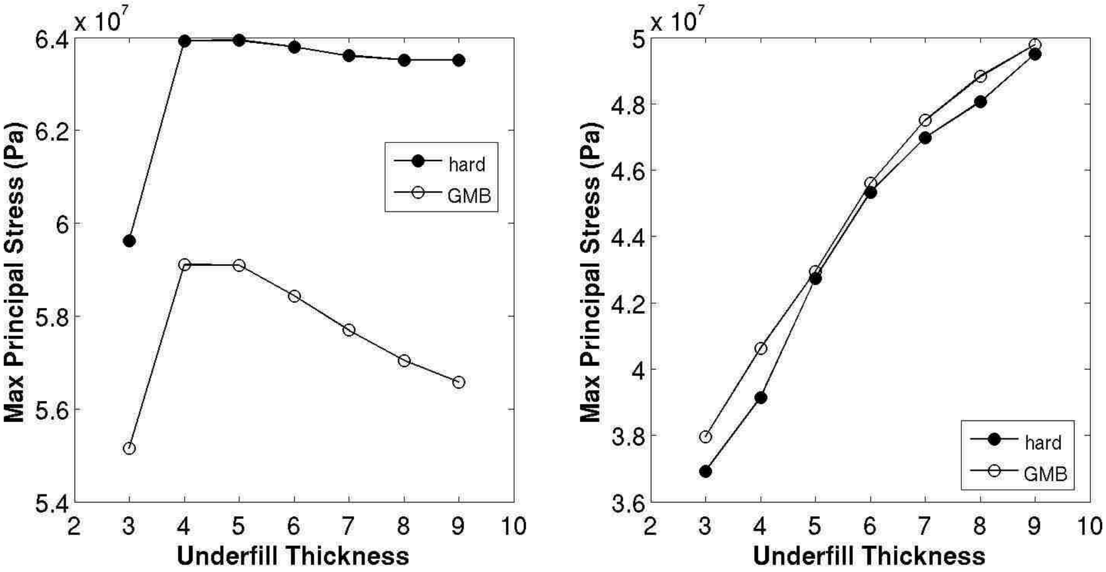

Figure 7-3: Ceramic maximum principal stress vs. underfill thickness for GMB epoxy encapsulated capacitor (left) and resistor (right) with 20% FVF solid and GMB underfills.

The conclusion to take from these models is that component stress in an epoxy over-encapsulated capacitor is not significantly affected by underfill thickness, and may result in stress variations at most on the order 7%. The resistor on the other hand, experienced a ~25% lower stress when the underfill thickness was reduced from 0.009" to 0.003".

The peak maximum principal stress in the ceramic, PMB polysulfide coated, epoxy encapsulated components as a function of various underfill thicknesses can be seen in Figure 7-4. The capacitor results (Figure 7-4, left), with an underfill thickness increase from 0.003" to 0.009", decreased in stress from 122 MPa to 107 MPa, or 12% for the 20% solid hard filled underfill case. The 20% GMB filled underfill case resulted in a 15% decrease from 112 MPa to 95.0 MPa. The resistor results were somewhat different (Figure 7-4, right). In the 20% GMB filled underfill case, the stress decreased 2% from 40.6 MPa to 39.8 MPa as the underfill thickness increased from 0.003" to 0.004", and the stress increased by 24% from 39.8 MPa to 49.2 MPa as the underfill thickness further increased from 0.004" to 0.009". The 20% solid hard filled underfill case resulted in a minimum stress of 44.0 MPa at an underfill thickness of 0.005", and a maximum stress of 46.4 MPa at an underfill thickness of 0.009", for a 5.5% disparity.

A couple trends identified from the PMB polysulfide coated, GMB epoxy encapsulated components were also found. Most notably, the stress in the capacitor decreased by as much as 12% as the underfill thickness was increased. The optimum height from the board for the more flexible resistor was found to be around 0.004” to 0.005” for both underfill filler cases.

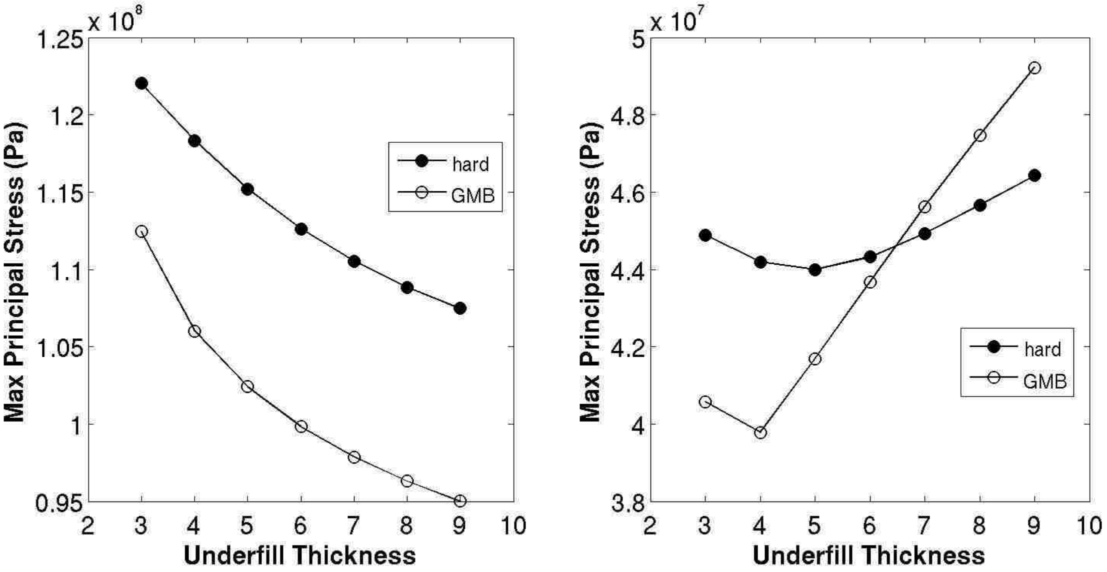

Figure 7-4: Ceramic maximum principal stress vs. underfill thickness for elastomer coated, GMB epoxy encapsulated capacitor (left) and resistor (right) with 20% FVF solid and GMB underfills.

7.2 Underfill Thickness and Underfill Stress

7.2.1 *No Encapsulant / Foam Encapsulant*

The calculated peak maximum principal stress in the underfill for the unencapsulated components as a function of underfill thickness can be seen in Figure 7-5. Results for 20% solid hard and GMB filled underfills are depicted for both the capacitor (left) and resistor (right). For both the capacitor and resistor, a monotonic decrease in stress was realized as the underfill thickness was increased from 0.003” to

0.009”. The capacitor underfill stress was decreased from 69.7 MPa to 67.9 MPa (2.6%), for the solid hard filled underfill case, while the GMB filled underfill case resulted in a decrease from 62.8 MPa to 60.2 MPa, or 4.1%. The resistor underfill stress also decreased by 2.8% from 68.2 MPa to 66.3 MPa for the solid hard filled underfill case, and the GMB filled underfill case resulted in a 3.6% decrease from 60.9 MPa to 58.7 MPa.

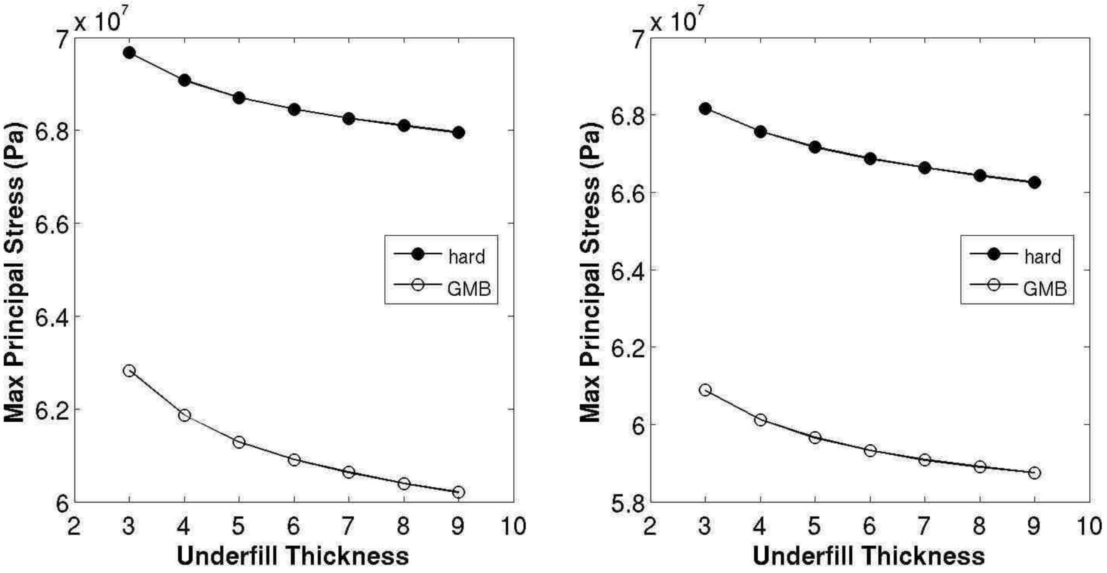

Figure 7-5: Underfill maximum principal stress vs. underfill thickness for unencapsulated capacitor (left) and resistor (right) with 20% FVF solid and GMB underfills.

Figure 7-6 depicts the calculated peak maximum principal stress in the underfill for the foam encapsulated capacitor (left) and resistor (right) as a function of underfill thickness. As seen in the figure, the capacitor with a 20% solid hard filled underfill experienced a decrease in underfill stress of 1.5% from 68.3 MPa to 67.3 MPa, as the underfill thickness was increased from 0.003" to 0.006". With further underfill thickening to 0.009", the stress increased 4.2% to 70.1 MPa. The capacitor with a 20% GMB filled underfill experienced a monotonic decrease in stress from 61.1 MPa to 59.0 MPa (3.4%) as the underfill thickness was increased from 0.003" to 0.009". The resistor (Figure 7-6, right) for both underfill filler cases experienced a monotonic decrease in stress as the underfill thickness was increased from 0.003" to 0.009". The 20% GMB filled underfill case experienced a decrease of 3.3% from 60.5 MPa to 58.5 MPa, and the 20% solid hard filled underfill case experienced a decrease of 2.9% from 67.8 MPa to 65.8 MPa.

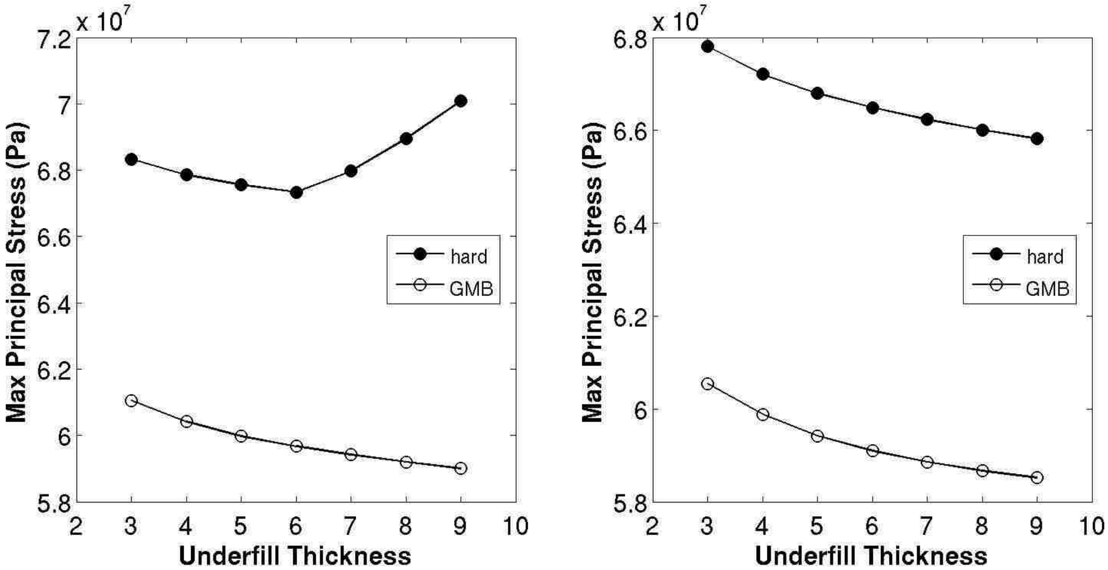

Figure 7-6: Underfill maximum principal stress vs. underfill thickness for foam encapsulated capacitor (left) and resistor (right) with 20% FVF solid and GMB underfills.

For three of the four foam encapsulated cases analyzed, stress decreased with increased underfill thickness. However, the magnitude of the stress reduction at most was only ~3%. While an optimum underfill thickness of 0.006” was identified for the 20% solid hard filled underfill capacitor case, the stress for all thickness investigated only varied by 4.2%.

7.2.2 *Epoxy Encapsulant*

The underfill maximum principal stress as a function of underfill thickness can be seen in Figure 7-7 for the uncoated, GMB epoxy encapsulated capacitor (left) and resistor (right). As seen in the figure, for both components in all cases, the underfill experienced a monotonic decrease in stress as the underfill thickness was increased from 0.003” to 0.009”. For the 20% GMB filled underfill cases, the capacitor underfill experienced a 19% decrease in stress from 82.2 MPa to 66.8 MPa, while the resistor underfill experienced a 5.8% decrease from 56.8 MPa to 53.5 MPa. In the 20% solid hard filled underfill cases, the capacitor underfill experienced a 15% decrease in stress from 108 MPa to 92.2 MPa, while the resistor underfill experienced a 2.6% decrease in stress from 70.3 MPa to 68.5 MPa.

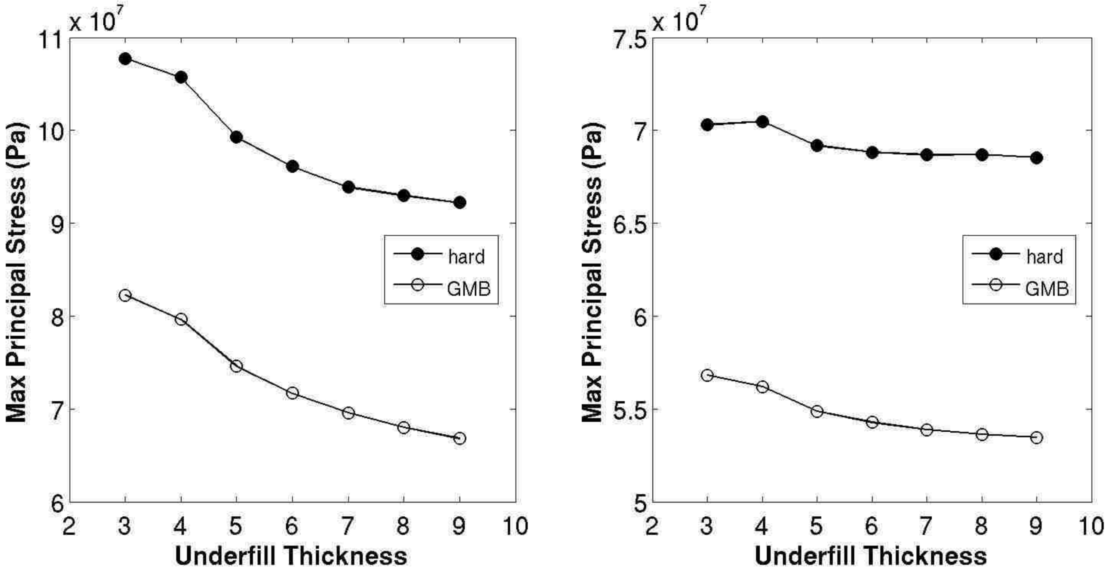

Figure 7-7: Underfill maximum principal stress vs. underfill thickness for GMB epoxy encapsulated capacitor (left) and resistor (right) with 20% FVF solid and GMB underfills.

For the PMB polysulfide coated, GMB epoxy encapsulated components, the underfill maximum principal stress as a function of underfill thickness can be seen in Figure 7-8. As seen in the figure, for the 20% solid hard filled underfill case, a peak stress of 168 MPa is experienced by the capacitor underfill (Figure 7-8, left) at an underfill thickness of 0.004”, which progressively decreased by 11% to 149.6 MPa at a thickness of 0.009”. The 20% GMB filled underfill case, resulted in a peak capacitor stress of 132 MPa (Figure 7-8, left) at an underfill thickness of 0.003”, which progressively decreased by 16.7% to 110 MPa at a thickness of 0.009”. The resistor underfill (Figure 7-8, right), experienced a monotonic decrease in stress for both underfill filler cases as thickness was increased. The solid hard filled underfill case resulted in a 6.7% decrease from 88.9 MPa to 82.9 MPa; while the GMB filled underfill case resulted in a 10% decrease from 71.1 MPa to 63.9 MPa.

While the trends for both GMB epoxy encapsulated cases appear fairly similar, e.g. underfill stress drops slightly with increased underfill thickness, the most notable observation is the stress increase in the capacitor underfill between the elastomer coated and uncoated cases. The maximum stress experienced by the capacitor underfill was 108 MPa for the uncoated case. The maximum stress experienced in the underfill for the elastomer coated capacitor was 168 MPa, a 56% increase in stress. This result is consistent with the findings in Section 5.2.

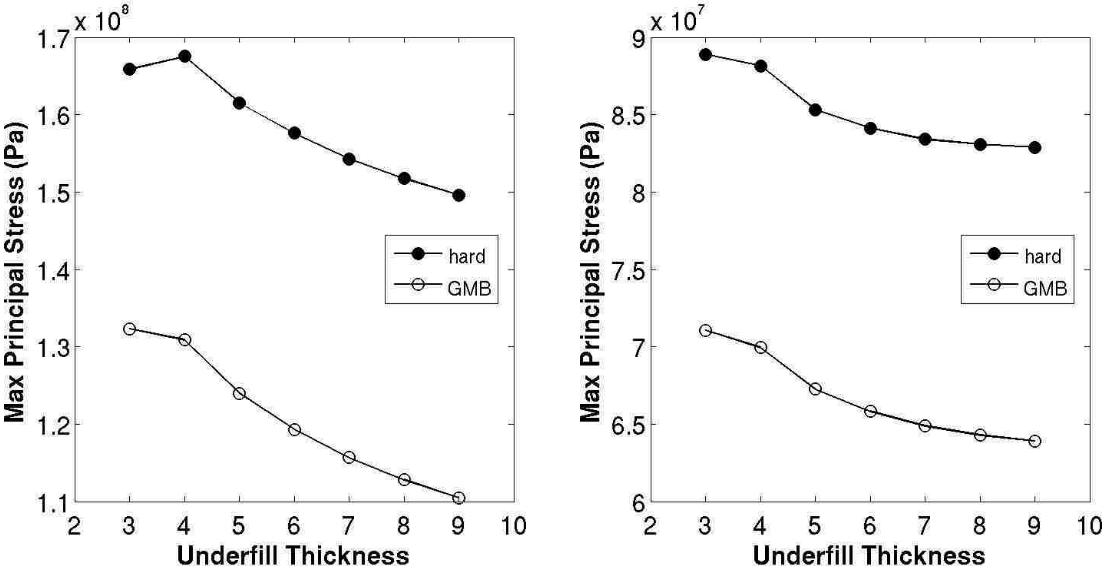

Figure 7-8: Underfill maximum principal stress vs. underfill thickness for elastomer coated, GMB epoxy encapsulated capacitor (left) and resistor (right) with 20% FVF solid and GMB underfills.

7.3 Underfill Thickness and Solder Fatigue

7.3.1 *No Encapsulant / Foam Encapsulant*

The predicted solder fatigue lives for the unencapsulated capacitor (left) and resistor (right) are plotted in Figure 7-9 for a range of underfill thicknesses. In the figure, it can be seen that at least for underfilled components, an optimum underfill thickness exists.

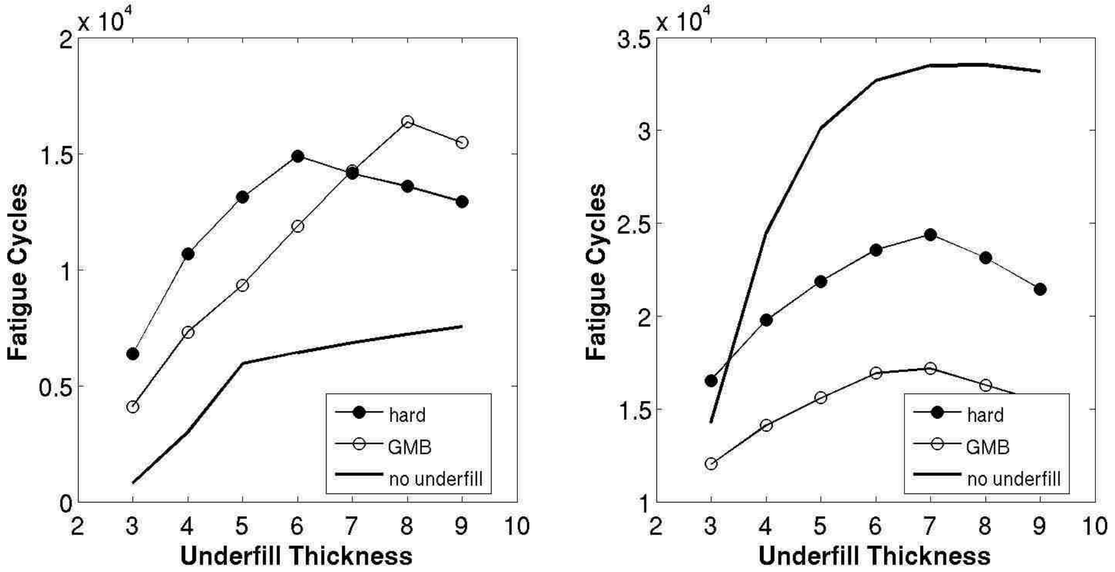

Figure 7-9: Thermal cycles for solder fatigue crack initiation vs. underfill thickness for unencapsulated capacitor (left) and resistor (right) with 20% FVF solid and GMB underfills.

For the capacitor, the 20% solid hard filled underfill case experienced a maximum fatigue life of 14,897 cycles with an underfill thickness of 0.006”. This was a 134% increase from the minimum fatigue life of 6,361 cycles experienced with an underfill thickness of 0.003". The 20% GMB filled case, on the other hand, resulted in a maximum fatigue life of 16,360 cycles at an underfill thickness of 0.008", a real improvement (299%) from the minimum fatigue life of 4,096 cycles experienced with an underfill thickness of 0.003". In all cases, when compared at the same height from the board, the underfilled capacitor fatigue lives exceeded those of the cases without underfill. The capacitor without underfill resulted in a monotonic increase in fatigue life from 803 cycles to 7,535 cycles (838% increase) as the gap from the board was increased from 0.003" to 0.009".

While adding underfill to the capacitor resulted in increased solder fatigue life, the opposite was true for the resistor. Only the case where the gap from the board was 0.003", did and underfilled resistor's fatigue life exceed that of the resistor without underfill. Both underfilled resistors experienced peak solder fatigue lives with an underfill thickness of 0.007". The GMB filled underfill case resulted in a peak solder fatigue life of 17,178 cycles, a 43% improvement from the 12,028 cycles predicted at 0.003", and the hard filled underfill case produced a peak fatigue life of 24,394 cycles, a 48% improvement from the 16,535 cycles also predicted at 0.003". The resistor without underfill resulted in a minimum fatigue life of 14,252 cycles at 0.003" from the board, and a maximum fatigue life of ~33,300 cycles at distances of 0.007", 0.008", and 0.009" from the board.

As a result of the study, a couple common “trends” were identified from the unencapsulated component underfill thickness study. Most notable were that underfill thickness can be tailored to optimize solder fatigue lives for underfilled components, and that increased elevation from the board resulted in increased fatigue life for components without underfill.

The predicted solder fatigue lives for the foam encapsulated capacitor (left) and resistor (right) are plotted in Figure 7-10 for a range of underfill thicknesses. In the hard filled underfill case, the capacitor experienced a maximum fatigue life of 5,845 cycles with an underfill thickness of 0.007”, a 229% increase from the minimum fatigue life of 1,777 cycles experienced for an underfill thickness of 0.003”. The GMB filled case resulted in a monotonic increase in fatigue life from a minimum of 1,500 cycles to a maximum of 5,050 cycles, resulting in a 237% increase as underfill thickness was increased from 0.003” to 0.009”. As with the unencapsulated case, both underfilled resistors achieved maximum solder fatigue lives with underfill thicknesses of 0.007” and minimum fatigue lives with underfill thicknesses of 0.003”. The GMB filled underfill case resulted in a peak solder fatigue life of 14,294 cycles, a 46% improvement from the 9,796 cycle minimum. The hard filled underfill case achieved a peak fatigue life of 20,363 cycles, a 56% improvement from the 13,084 cycle minimum.

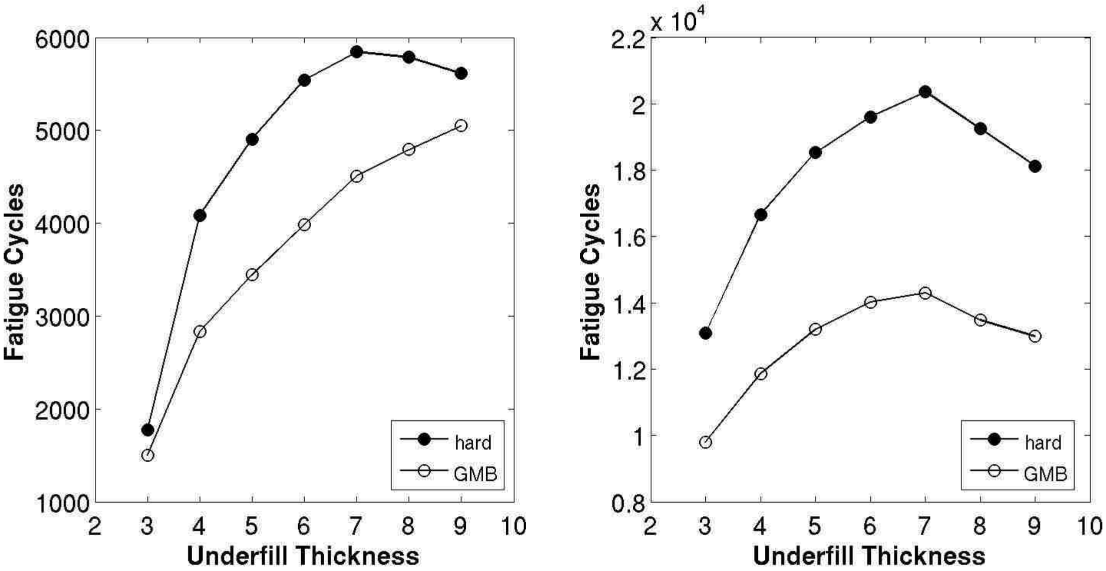

Figure 7-10: Thermal cycles for solder fatigue crack initiation vs. underfill thickness for foam encapsulated capacitor (left) and resistor (right) with 20% FVF solid and GMB underfills.

While the solder fatigue lives were somewhat reduced by the inclusion of foam encapsulation, the “trends” identified in the unencapsulated case appear to hold. Most importantly, underfill thickness can be tailored to optimize solder fatigue lives for underfilled components.

7.3.2 *Epoxy Encapsulant*

As shown in Figure 7-11 and Figure 7-12, the solder fatigue life predictions for the 828/DEA/GMB epoxy encapsulated components are quite similar. In all cases, both components experienced a monotonic increase in fatigue life with increased underfill thickness.

For the uncoated case, the capacitor (Figure 7-11, left) predicted a solder fatigue life increase from 53 cycles to 587 cycles, or 1007% for the 20% hard filled underfill, and from 48 cycles to 526 cycles, or 995% for the 20% GMB filled underfill. The uncoated resistor results can be seen in the right plot of Figure 7-11. In this case, the predicted solder fatigue life with the 20% hard filled underfill increased 221% from 777 cycles to 2,491 cycles. The 20% GMB filled underfill resulted in an increase of 210% from 748 cycles to 2,320 cycles.

The results for the PMB polysulfide coated, GMB epoxy encapsulated capacitor can be seen in the left plot of Figure 7-12. As shown in the figure, the predicted solder fatigue life increased by 869% from 56 cycles to 543 cycles for the 20% hard filled underfill, and by 985% from 48 cycles to 521 cycles for the 20% GMB filled underfill. For the elastomer coated resistor (Figure 7-12, left), the solder fatigue life was predicted the to increase by 442% from 458 cycles to 2,482 cycles for the 20% hard filled underfill, and by 446% from 426 cycles to 2,324 cycles for the 20% GMB filled underfill.

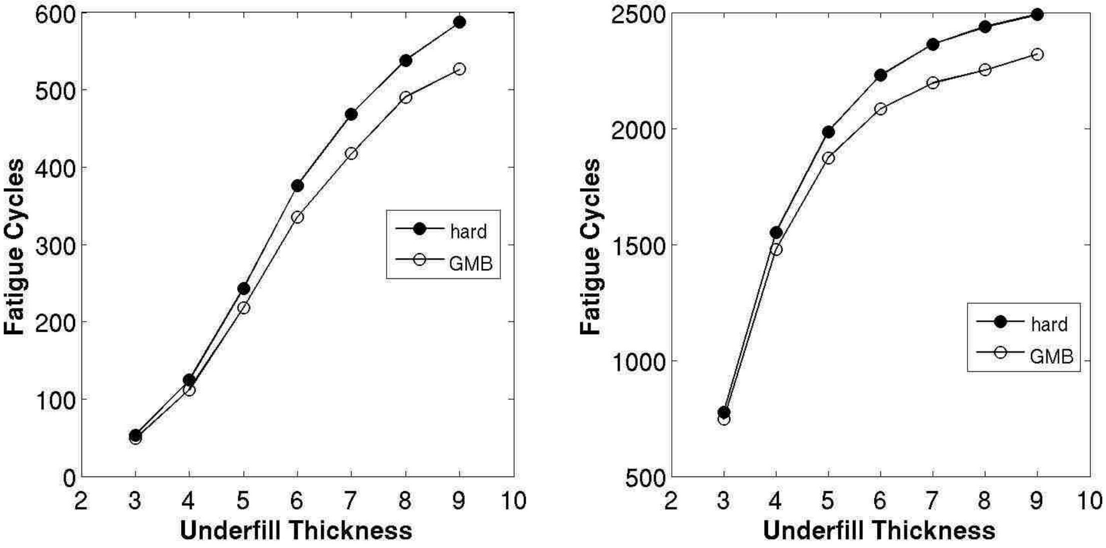

Figure 7-11: Thermal cycles for solder fatigue crack initiation vs. underfill thickness for GMB epoxy encapsulated capacitor (left) and resistor (right) with 20% FVF solid and GMB underfills.

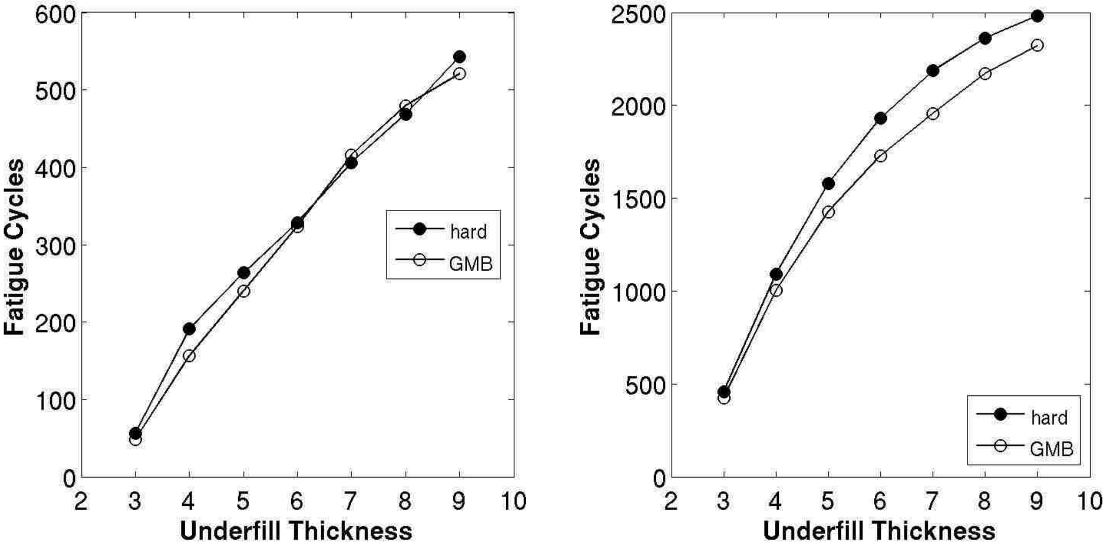

Figure 7-12: Thermal cycles for solder fatigue crack initiation vs. underfill thickness for elastomer coated, GMB epoxy encapsulated capacitor (left) and resistor (right) with 20% FVF solid and GMB underfills.

7.4 Underfill Thickness Results Discussion

The unencapsulated and foam encapsulated components experienced a modest increase in ceramic stress (2.6% to 17% depending on which case) as the component height from the board was increased, however, the underfill stress only varied by 1.5% to 4.2%. The most notable “trend” identified for the unencapsulated and foam encapsulated components, was the ability to optimize solder fatigue lives for underfilled components. By varying the underfill thickness, fatigue lives could be improved as much as 838%.

For uncoated GMB epoxy encapsulated capacitor, ceramic stress was only affected by 7% due to underfill thickness variations. The thinner more flexible resistor experienced a ~25% stress reduction as the underfill thickness was decreased from 0.009” to 0.003”. For the PMB polysulfide coated, GMB epoxy encapsulated components, the stress in the capacitor decreased by as much as 12% as underfill thickness was increased. Stress in the more flexible resistor was found to vary as much as 24%, and an optimum height from the board was found to be around 0.004” to 0.005”. The solder fatigue life predictions for all the 828/DEA/GMB epoxy encapsulated cases were quite similar. In all cases, both components experienced a huge monotonic increase in fatigue life with increased underfill thickness ranging from 210% for the resistor to 1007% for the capacitor.

8 Underfill Glass Transition Temperature

For a component subjected to thermal cycling, common sense would state that a room temperature cured elastomeric underfill would be disastrous. Given the high CTE and large bulk modulus of elastomers, upon heating, the elastomer would swell and pop components off the PCB. In addition, the adhesive strength of rubbery polymers is relatively small compared to that of glassy thermoset polymers, thus additional component stress reduction from the underfill during PCB flexure or dynamics would be minimal. The intent of this computational study was to identify whether an ideal glass transition temperature exists for underfill materials subjected to thermal cycling, and determine where it should lie within the thermal operating range of a packaged component.

Using the quasi-static, thermal stress, finite element models, described in Chapter 3, residual manufacturing stresses were investigated for the capacitor and resistor to determine the effects of underfill glass transition temperature (Tg) on component stress, solder fatigue life, and underfill stress for surface mount components. Additional variables included in the calculations were underfill filler volume fraction, elastomer coating, and over-encapsulation. For each case shown in Table 8-1, the glass transition temperatures were varied from -40°C to 100°C in 20 degree increments. This was done by modifying the reference temperature in the SPEC constitutive model [2] for the underfill. The underfill thickness in both components was assumed to be 0.005" thick, to isolate any findings to Tg effects. As in previous studies, the intent was to identify, where possible, simple design guidelines for surface mount electronics packaging by looking for "trends". Because the results of the encapsulated and foam encapsulated cases were so similar, only the unencapsulated results are discussed in the following sections. To reduce complexity, the plots in the following sections only depict the results for the 20% filled underfill cases.

Table 8-1: Packaging variations modeled for underfill glass transition study.

Underfills → Encapsulation ↓	**No Underfill**	**Unfilled Epoxy Underfill**	**Filled with 10-40 vol% Alumina**	**Filled with 10-40 vol% GMB**
No Encapsulation	X	X	X	X
GMB-Epoxy Encapsulation no Coating		X	X	X
GMB-Epoxy Encapsulation with 0.005" Polysulfide Filled with PMB		X	X	X
20# Foam Encapsulation no Coating		X	X	X

8.1 Underfill Tg and Component Stress

8.1.1 *No Encapsulant*

The ceramic maximum principal stress results as a function of underfill Tg for the unencapsulated capacitor (left) and resistor (right) can be seen in Figure 8-1. As seen in the figure, a Tg reduction from 100°C to -40°C, reduced the capacitor stress by 10% from 58.8 MPa to 52.7 MPa for the 20% hard filled underfill, and by 11% from 58.4 MPa to 52.2 MPa for the 20% GMB filled underfill. The opposite trend was true for the resistor however. The resistor, for the same 100°C to -40°C underfill Tg reduction, experienced a 98% stress increase from 45.9 MPa to 90.7 MPa for the GMB filled case and a 111% increase from 47.0 MPa to 99.3 MPa for the hard filled case.

While a modest stress reduction (~10%) was experienced in the capacitor, a large stress increase (~100%) was experienced by the resistor with underfill Tg reduction. Since the resistor is more flexible than the capacitor, it is susceptible to the high CTE and large bulk modulus of the elastomeric underfill, which results in bending of the resistor. This bending can lead to higher localized stresses.

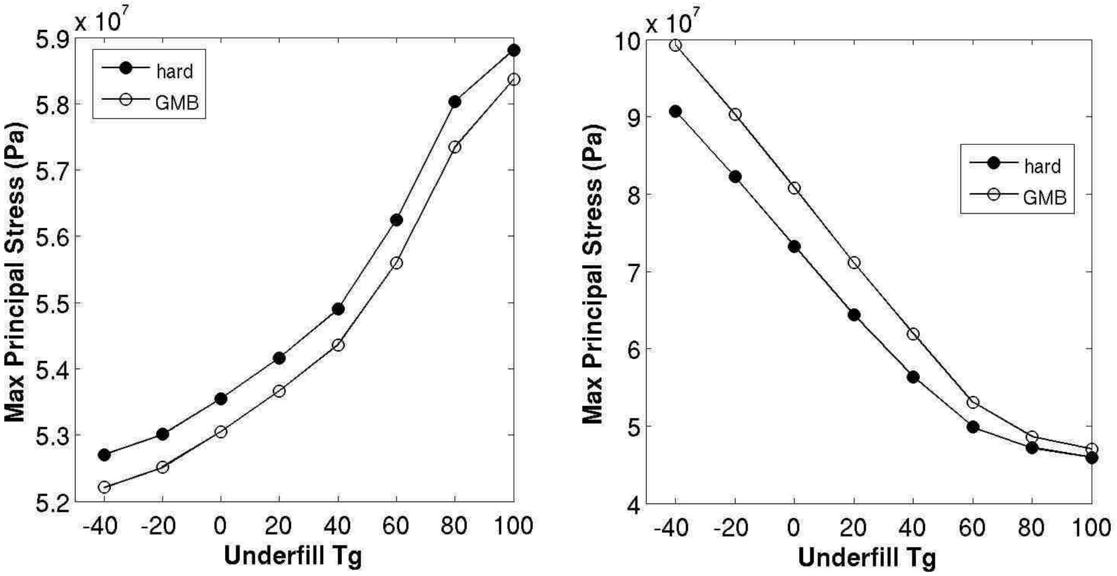

Figure 8-1: Ceramic maximum principal stress vs. underfill Tg for unencapsulated capacitor (left) and resistor (right) with 20% FVF solid and GMB underfills.

8.1.2 *Epoxy Encapsulant*

The ceramic maximum principal stress results as a function of underfill Tg for the 828/DEA/GMB epoxy encapsulated capacitor (left) and resistor (right) can be seen in

Figure 8-2. As seen in the figure, reduction of the Tg from 100°C to 20°C, reduced the capacitor stress by 33% from 67.7 MPa to 45.2 MPa for the 20% hard filled underfill. Further reduction of the Tg to -40°C, however, resulted in a stress increase from 45.2 MPa to 48.7 MPa. For the 20% GMB filled underfill case, the capacitor experienced a reduction in stress from 61.5 MPa to 44.7 MPa, or 27% with a Tg reduction from 100°C to 40°C, but upon further reduction of the Tg to -40°C, the ceramic stress increased from 44.7 MPa to 49.3 MPa.

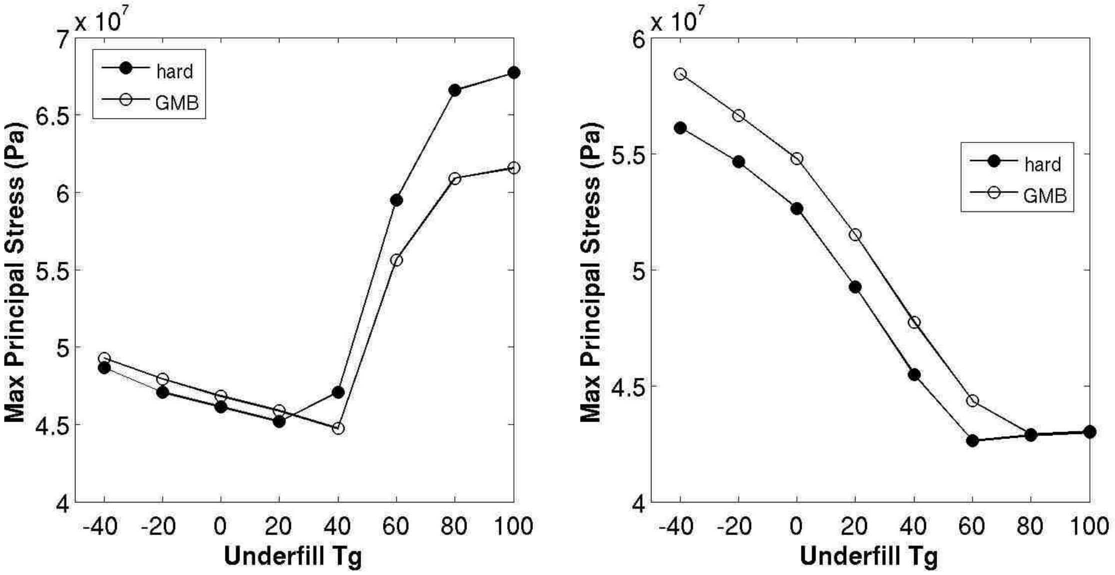

Figure 8-2: Ceramic maximum principal stress vs. underfill Tg for GMB epoxy encapsulated capacitor (left) and resistor (right) with 20% FVF solid and GMB underfills.

The 20% hard filled underfill resistor case (Figure 8-2 , right), resulted in a slight decrease in ceramic stress from 43 MPa to 42.6 MPa for a Tg decrease from 100°C to 60°C, but a 32% increase in stress from 42.6 MPa to 56.1 MPa with further Tg reduction to -40°C. Similarly, the 20% GMB underfilled resistor, resulted in a decrease in ceramic stress from 43 MPa to 42.9 MPa for a Tg decrease from 100°C to 80°C, followed by a 36.1% increase in stress from 42.9 to 58.4 at a Tg of -40°C.

Figure 8-3 depicts the ceramic maximum principal stress results as a function of underfill Tg for the PMB polysulfide coated, GMB epoxy encapsulated components. As seen in the left plot, the capacitor stress was reduced monotonically from 125 MPa to 66.7 MPa (47%) for the 20% hard filled underfill case, when the Tg was reduced from 100°C to -40°C. Likewise, the 20% GMB filled underfill case resulted in a 42% stress reduction from 109 MPa to 63.3 MPa. The resistor (Figure 8-3, right), for both underfill filler cases, experienced an increase in stress with underfill Tg reduction. With the Tg reduced from 100°C to -400°C, the hard filled underfill case, resulted in a stress increase of 63% from 40.3 MPa to 65.8 MPa, and for the GMB filled underfill case, an increase of 84%, from 39.8 MPa to 73.4 MPa was the result.

“Trends” seen for the GMB epoxy encapsulated components appear similar to those of the unencapsulated. As underfill Tg was reduced, the stress in the capacitor decreased, but increased in the resistor. The most notable exception to this trend was for the uncoated capacitor, which experienced a sharp decrease in stress until the underfill reached about ~40°C, but then experienced a stress increase with further Tg reduction. This trend can be explained by the confined state of the underfill when over encapsulated. In the rubbery state, the underfill experiences an order of magnitude drop in the shear modulus, which explains the further stress decrease for the elastomer coated and unencapsulated cases. However, when the underfill was confined by the GMB epoxy encapsulation, the bulk modulus becomes the dominant contributor to the stress state, and because of the higher rubbery CTE, a stress increase was experienced with further cooling.

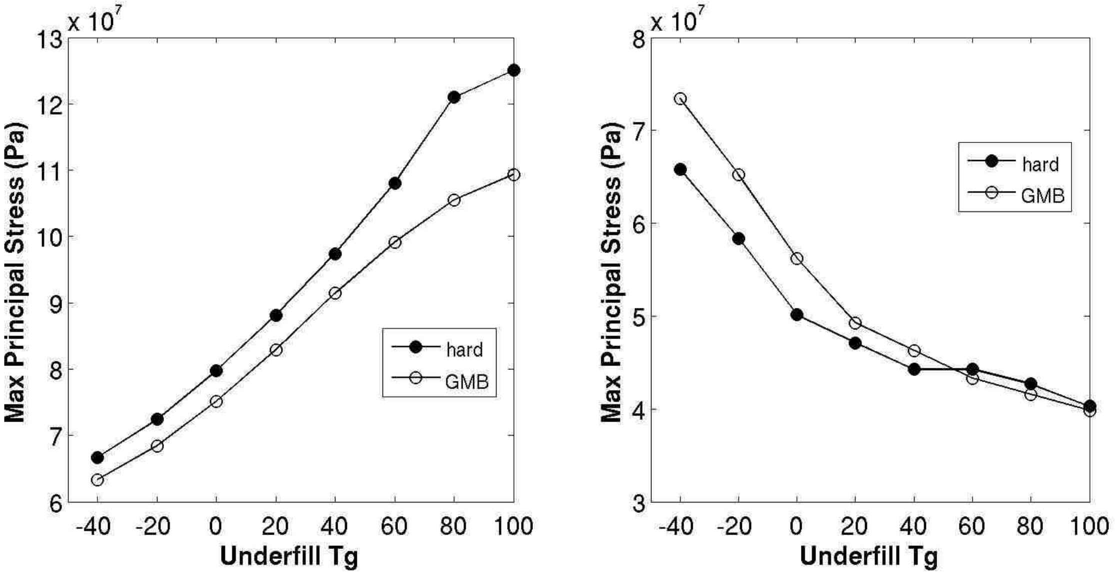

Figure 8-3: Ceramic maximum principal stress vs. underfill Tg for elastomer coated, GMB epoxy encapsulated capacitor (left) and resistor (right) with 20% FVF solid and GMB underfills.

8.2 Underfill Tg and Underfill Stress

8.2.1 *No Encapsulant*

The predicted maximum principal stress in the underfill as a function of Tg for the unencapsulated components can be seen in Figure 8-4. With a Tg reduction from

100°C to 60°C, the capacitor (left) experienced a stress increase of 25.5% from 55.5 MPa to 69.5 MPa for the 20% hard filled underfill case, and a stress increase of 31% from 48.2 MPa to 63.1 MPa for the 20% GMB filled underfill case. Further reduction of the Tg to -40°C, resulted in a more modest 17% stress decrease from 69.5 MPa to 57.6 MPa and a 11% decrease from 63.1 MPa to 56.3 MPa for the hard and GMB filled cases respectively. Results for the resistor underfill (right) were found to be almost identical, and did not warrant further discussion.

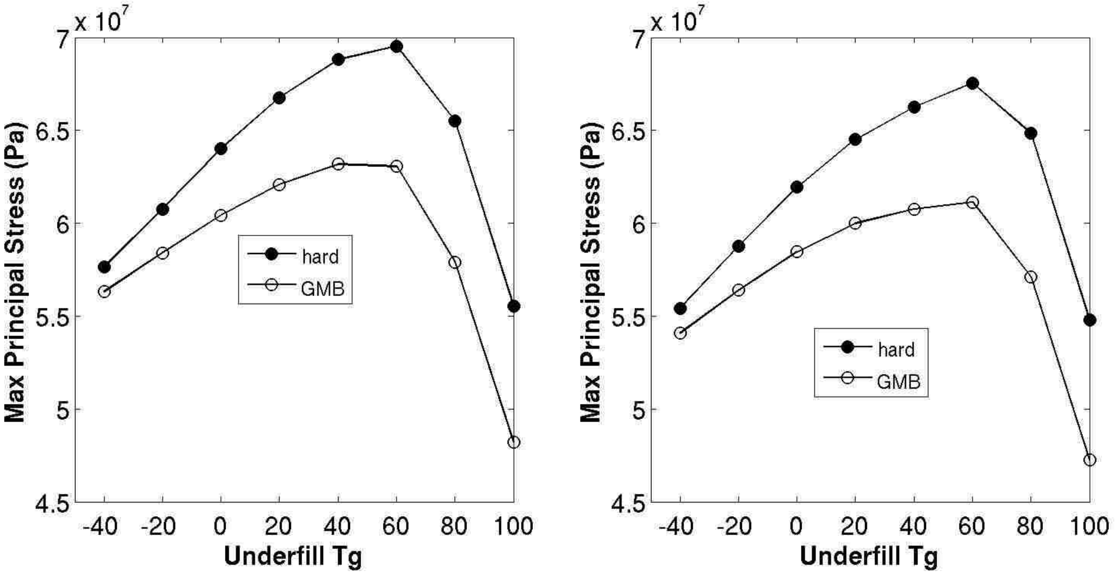

Figure 8-4: Underfill maximum principal stress vs. underfill Tg for unencapsulated capacitor (left) and resistor (right) with 20% FVF solid and GMB underfills.

As described in the results and seen in the figure, a sharp increase in underfill stress occurred as the Tg was decreased from 100°C to 60°C for all cases depicted. This stress increase was then followed by a more gradual reduction in stress as the Tg was further reduced to -40°C. While it is not the intent of this section to try and predict material failure, these stresses appear very high for the underfill material, if experienced near or above Tg, and might lead to adhesive failure. Further investigation in this area is recommended. It is also interesting to note that the Tg of 100°C resulted in the minimum underfill stress for all cases. This temperature was well above the stress free temperature of 80°C for the analysis, and would result in glassy material properties for the underfill throughout the entire thermal regime.

8.2.2 *Epoxy Encapsulant*

In Figure 8-5, the 828/DEA/GMB epoxy encapsulated component maximum principal stress in the underfill as a function of Tg can be seen. As seen in the figure, a Tg reduction from 100°C to 80°C, resulted in a capacitor (left) stress increase from 105 MPa to 106 MPa for the 20% hard filled underfill case, and a stress increase of 4.8% from 73.9 MPa to 77.5 MPa for the 20% GMB filled underfill case. Further reduction of the Tg to 0°C for the hard filled underfill, resulted in a stress reduction of 39% from 106 MPa to 64.6 MPa, and reduction of the Tg to 20°C for the GMB filled underfill, resulted in a stress reduction of 34% from 77.5 MPa to 50.9 MPa. Further reduction of the Tg to -40°C, resulted in an increase in stress for both underfill materials to 64.6 MPa and 69.9 MPa for the hard and GMB filled underfill materials respectively.

The 20% hard filled underfill resistor, seen in the right plot of Figure 8-5, experienced a stress increase of 15% from 59.4 MPa to 68.3 MPa for a Tg reduction from 100°C to 80°C. Continued reduction of the underfill Tg to 20°C, produce a drop in stress from 68.3 MPa to 62.3 MPa, or 8.8%, and a further reduction in the Tg to -40°C, resulted in a 25% stress increase to 77.9 MPa. For the GMB filled underfill case, a Tg reduction from 100°C to -40°C, resulted in a monotonic stress increase of 45% from 44.3 MPa to 81.1 MPa.

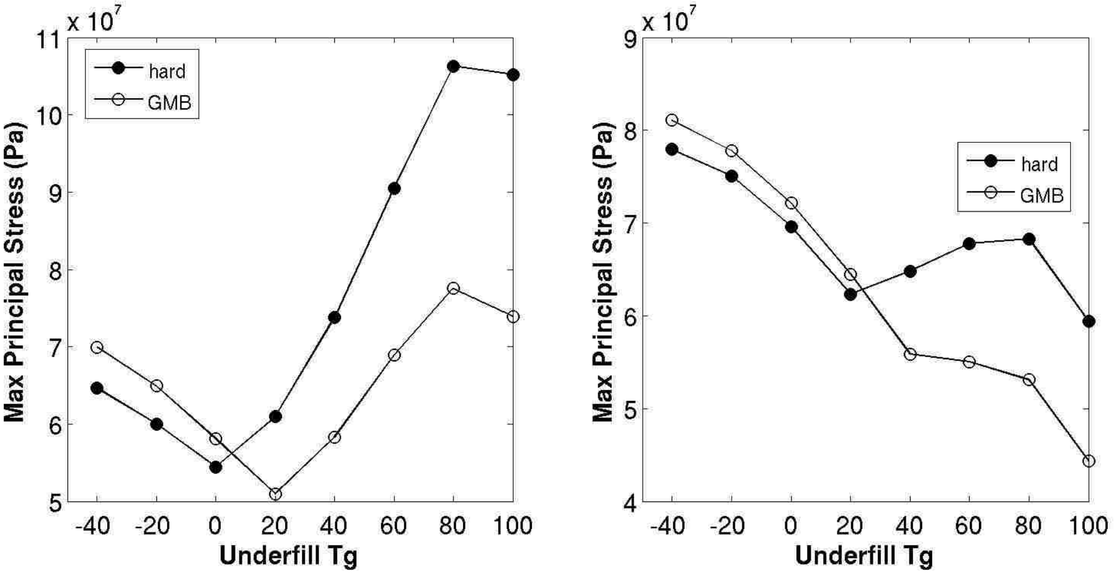

Figure 8-5: Underfill maximum principal stress vs. underfill Tg for GMB epoxy encapsulated capacitor (left) and resistor (right) with 20% FVF solid and GMB underfills.

Figure 8-6, depicts the maximum principal stress in the underfill as a function of Tg for the polysulfide PMB coated, 828/DEA/GMB epoxy encapsulated components. For both capacitor underfill material cases (left), the peak stress results remain virtually unchanged at underfill glass transition temperatures of 100°C and 80°C. A Tg reduction from 80°C to -40°C, however, resulted in a decrease in stress from 170 MPa to 50.8 MPa

(70%) for the 20% hard filled underfill case, and a decrease in stress from 130 MPa to 51.1 MPa, or 61% for the 20% GMB filled underfill case.

With the resistor (Figure 8-6, right), a Tg reduction from 100°C to 80°C, resulted in a stress increase of 10% from 78.1 MPa to 86.2 MPa for the 20% hard filled underfill case, and a stress increase of 12% from 60.4 MPa to 67.8 MPa for the 20% GMB filled underfill case. Further reduction of the underfill Tg to -40°C, resulted in a monotonic stress decrease to ~54 MPa, a decrease of 37% and 20% for the hard and GMB filled cases respectively.

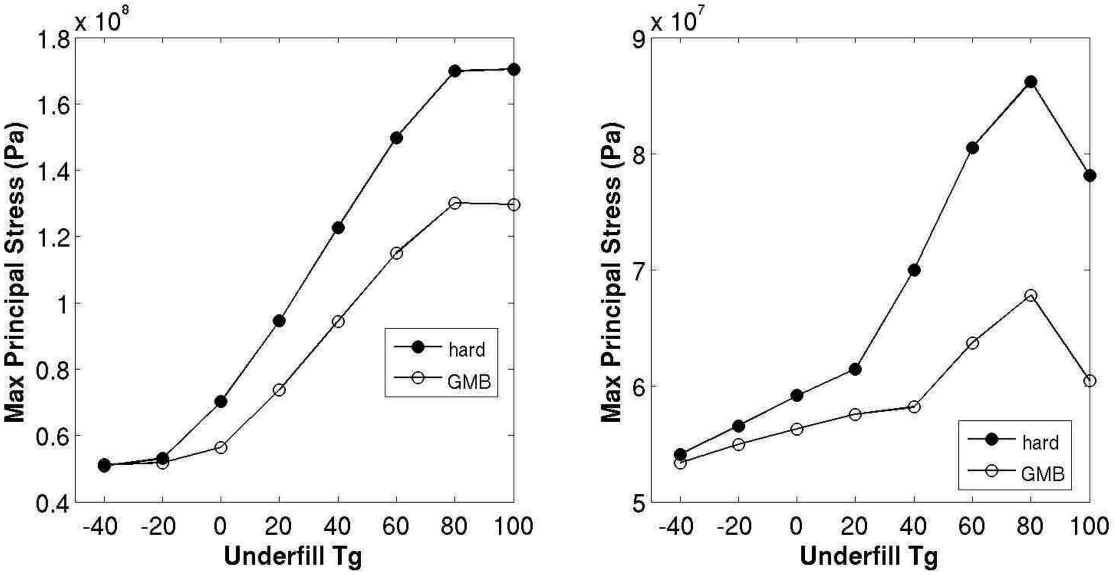

Figure 8-6: Underfill maximum principal stress vs. underfill Tg for elastomer coated, GMB epoxy encapsulated capacitor (left) and resistor (right) with 20% FVF solid and GMB underfills.

As explained in the last paragraph of Section 8.1.2, the increase in stress experienced by the GMB epoxy encapsulated underfills at lower Tg's can be attributed to the confined state of the underfill when over encapsulated. In the rubbery state, the underfill experiences an order of magnitude drop in the shear modulus, which explains the further stress decrease for the elastomer coated and unencapsulated cases. However, when the underfill was confined by the GMB epoxy encapsulation, the bulk modulus becomes the dominant contributor to the stress state, and because of the higher rubbery CTE, a stress increase was experienced with further cooling. That said, it is highly unlikely that the underfills remain bonded to the components at these predicted stresses for materials with Tg's around room temperature. In the rubbery state, polymer strength is significantly degraded, and adhesion at stresses in the neighborhood of 50, 60, 70 MPa is highly unlikely. Maintaining adhesion under these stresses, however, could be possible for polymers in their glassy state.

The real "trend" that should be noted for these underfill stress results is that with underfill Tg's above the stress free temperature, a stress reduction was experienced. As the underfill Tg deceased from 100°C to the stress free temperature (80°C), stress in the underfill increased.

8.3 Underfill Tg and Solder Fatigue

8.3.1 *No Encapsulant / Foam Encapsulant*

The predicted solder fatigue lives for the unencapsulated components are plotted in Figure 8-7 for a range of underfill glass transition temperatures. With a Tg reduction from 100°C to 60°C, the capacitor (Figure 8-7, left) experienced a solder fatigue life increase of 34% from 9,101 cycles to 12,235 cycles for the 20% hard filled underfill case. With further underfill Tg reduction to -40°C, the fatigue cycles monotonically decreased by 86% to 1,691 cycles. For the 20% GMB filled underfill case, a solder fatigue life increase of 4.0% from 9,813 cycles to 10,210 cycles was experienced for a Tg reduction from 100°C to 80°C, followed by a monotonic fatigue life decrease of 85% to 1,494 cycles for an underfill Tg of -40°C. The resistor (Figure 8-7, right), for both underfill filler cases, experienced a decrease in solder fatigue life with underfill Tg reduction. With the Tg reduced from 100°C to -40°C, the hard filled underfill case, resulted in a fatigue cycle decrease of 92% from 30,316 cycles to 2,513 cycles, and for the GMB filled underfill case, a decrease of 94%, from 34,964 cycles to 2,172 cycles was the result.

It should be pointed out that peak solder fatigue lives for both the resistor and capacitor were experienced within ~20°C of the stress free temperature (in this case 80°C), and that the rate of fatigue life decline was steepest near this max value.

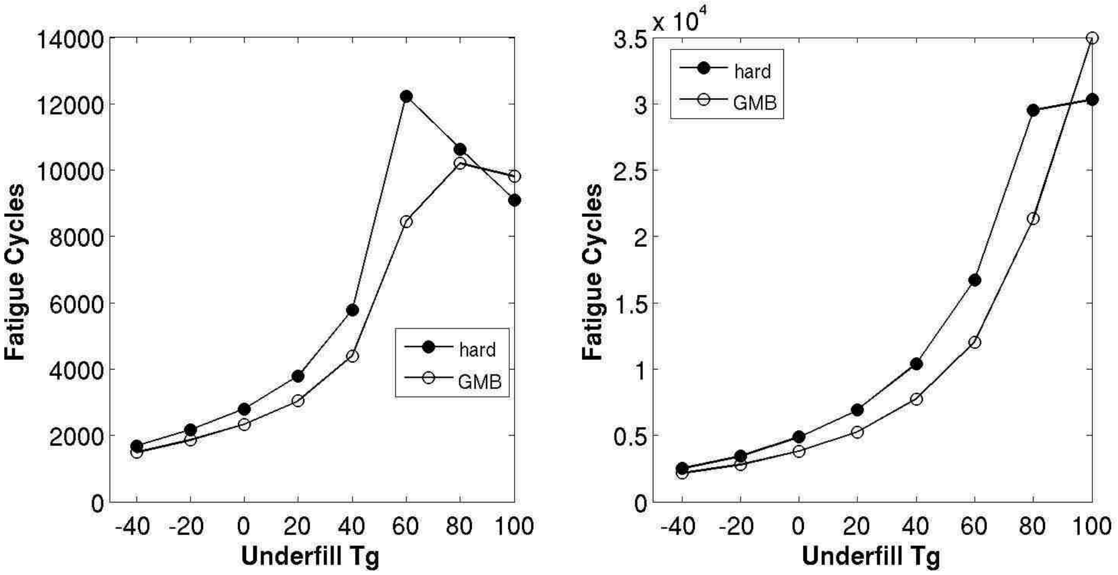

Figure 8-7: Thermal cycles for solder fatigue crack initiation vs. underfill Tg for unencapsulated capacitor (left) and resistor (right) with 20% FVF solid and GMB underfills.

8.3.2 *Epoxy Encapsulant*

In Figure 8-8, the predicted solder fatigue lives for the 828/DEA/GMB epoxy encapsulated components can be seen for a range of underfill glass transition temperatures. The 20% hard filled underfill capacitor (left) experienced a solder fatigue life decrease of 75% from 260 cycles to 64 cycles for a Tg reduction from 100°C to -20°C. The 20% GMB filled underfill case resulted in a solder fatigue life decrease of 75% from 236 cycles to 58 cycles for the same Tg reduction. It should be noted that the rate of fatigue life decline was lowest for underfills with elevated Tg's.

The resistor (Figure 8-8, right), for both underfill filler cases, experienced a decrease in solder fatigue life as the underfill Tg was decreased. With a Tg reduction from 100°C to 40°C, the hard filled underfill case, resulted in a fatigue cycle decrease of only 6.3% from 2,054 cycles to 1,925 cycles. Continued underfill Tg reduction to -40°C, resulted in a considerably more drastic drop in solder the fatigue life by 77% to 448 cycles. Similarly, the GMB filled underfill case resulted in a fatigue cycle decrease of only 2.6% from 1,953 cycles to 1,902 cycles for a Tg reduction from 100°C to 60°C. Upon further reduction of the underfill Tg to -40°C, the solder fatigue life dropped by 79% to 403 cycles.

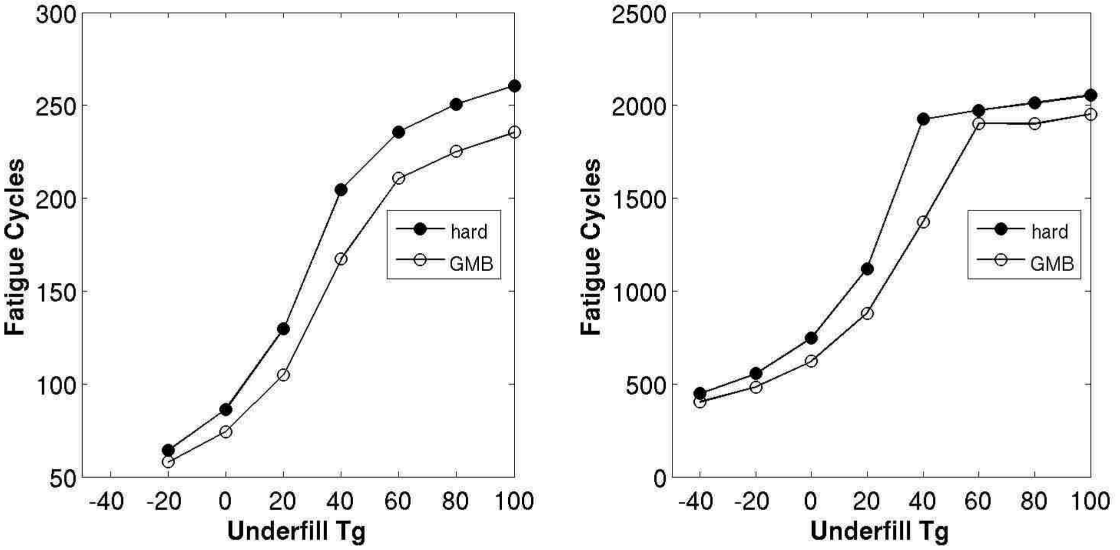

Figure 8-8: Thermal cycles for solder fatigue crack initiation vs. underfill Tg for GMB epoxy encapsulated capacitor (left) and resistor (right) with 20% FVF solid and GMB underfills.

The predicted solder fatigue lives for the polysulfide PMB coated, 828/DEA/GMB epoxy encapsulated components can be seen in In Figure 8-9, for a range of underfill glass transition temperatures. The capacitor (left) with a hard filled underfill initially experienced a solder fatigue life increase of 12% from 254 cycles to 285 cycles with a Tg reduction from 100°C to 40°C. For a Tg reduction from 100°C to 60°C, the GMB filled underfill capacitor also experienced a solder fatigue life increase from 227 cycles to 258 cycles, or of 14%. Further reduction of the underfill Tg to -40°C resulted in decreased fatigue lives on the order of 83% for both underfill cases.

The 20% hard filled underfill resistor (Figure 8-9, right) experienced a solder fatigue life decrease of 79% from 1,670 cycles to 357 cycles for a Tg reduction from 100°C to -40°C. The 20% GMB filled underfill case also resulted in a solder fatigue life decrease of 79% from 1,537 cycles to 322 cycles for the same Tg reduction. Note that the rate of fatigue life decline was lowest for underfills with elevated Tg's.

For all the cases investigated, the solder fatigue life "trends" were found to be similar. Most notably, underfill Tg's within about 20°C to 40°C of the stress free temperature, resulted in the highest fatigue lives for the both components. Underfill Tg's significantly below the stress free temperature, reduced the fatigue life by as much as 83%.

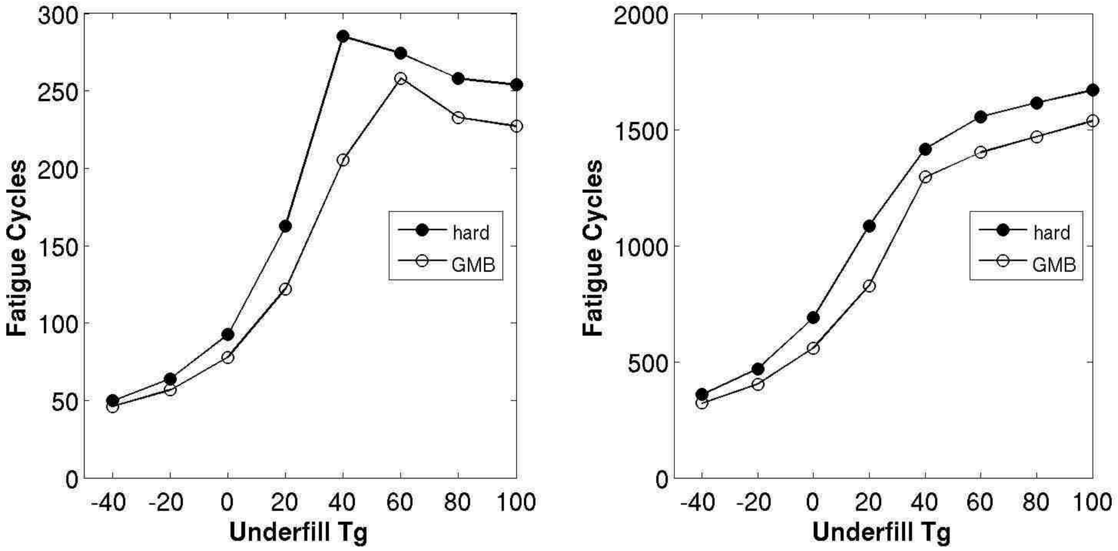

Figure 8-9: Thermal cycles for solder fatigue crack initiation vs. underfill Tg for elastomer coated, GMB epoxy encapsulated capacitor (left) and resistor (right) with 20% FVF solid and GMB underfills.

8.4 Underfill Tg Results Discussion

The most important finding from the underfill glass transition temperature study was that an underfill Tg should be close to the stress free temperature. Granted, in some cases it appeared that a Tg 20°C below the stress free temperature was best, and in others, 20°C above proved best, but in no case was a low Tg desirable. Low Tg underfill materials realized little benefit in component or underfill stress, and resulted in significant decreases in solder fatigue life.

9 Other Packaging Considerations

9.1 Confined Polymers

An over-encapsulated high-voltage transformer assembly, following manufacturing, passed subsequent thermal cycle testing and was then placed in storage. Four years later, the transformer failed the same thermal cycle test [1]. An x-ray of the failed transformer can be seen in Figure 9-1.

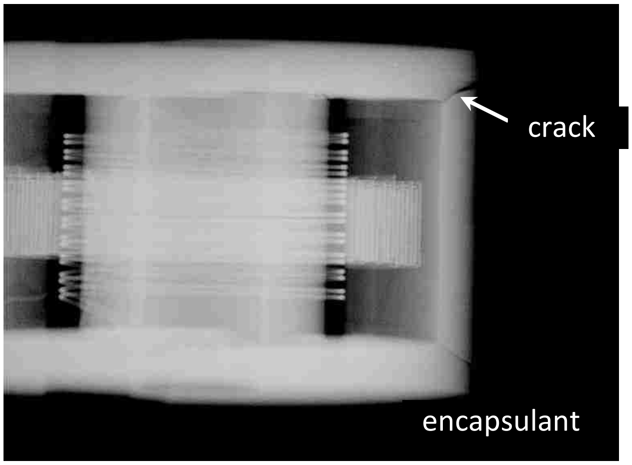

Figure 9-1: X-ray image of a failed ceramic transformer.

A systematic finite element analysis was carried out to investigate the generation of thermal stresses in the transformer assembly. The finite element model can be seen in Figure 9-2.

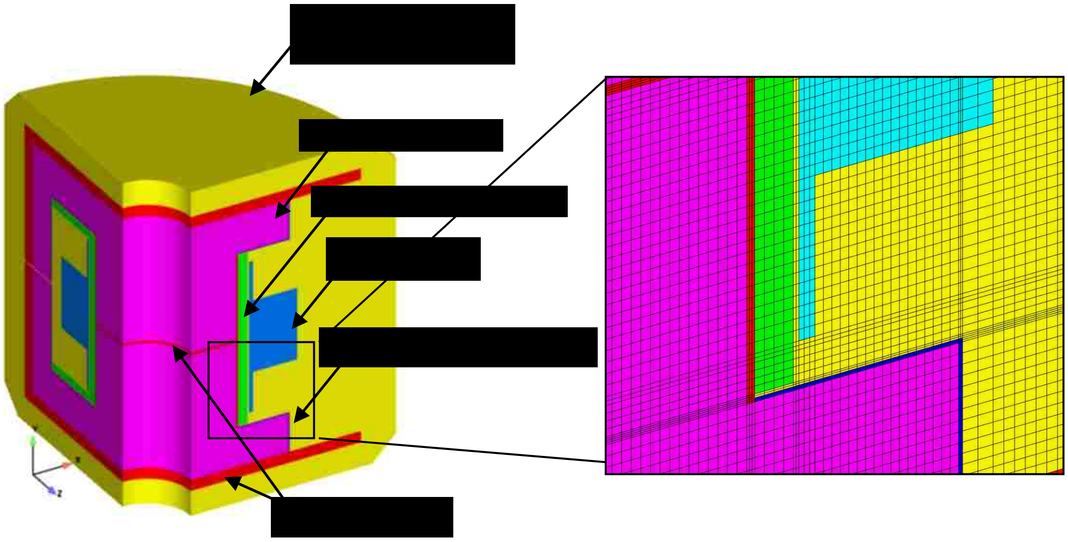

Figure 9-2: Model geometry of the transformer assembly used in the finite element analysis. A representative region is shown with the finite element mesh.

Although the ferrite core is entirely enclosed by materials with much greater coefficients of thermal expansion, it was demonstrated that, due to the combination of complex geometry and material properties, local tensile stresses could still be generated in the ceramic core upon cool-down from the stress free temperature. As seen in Figure 9-3, the magnitude of the maximum principal stress in the ceramic was predicted to exceed the nominal fracture strength of the ferrite of ~100 MPa.

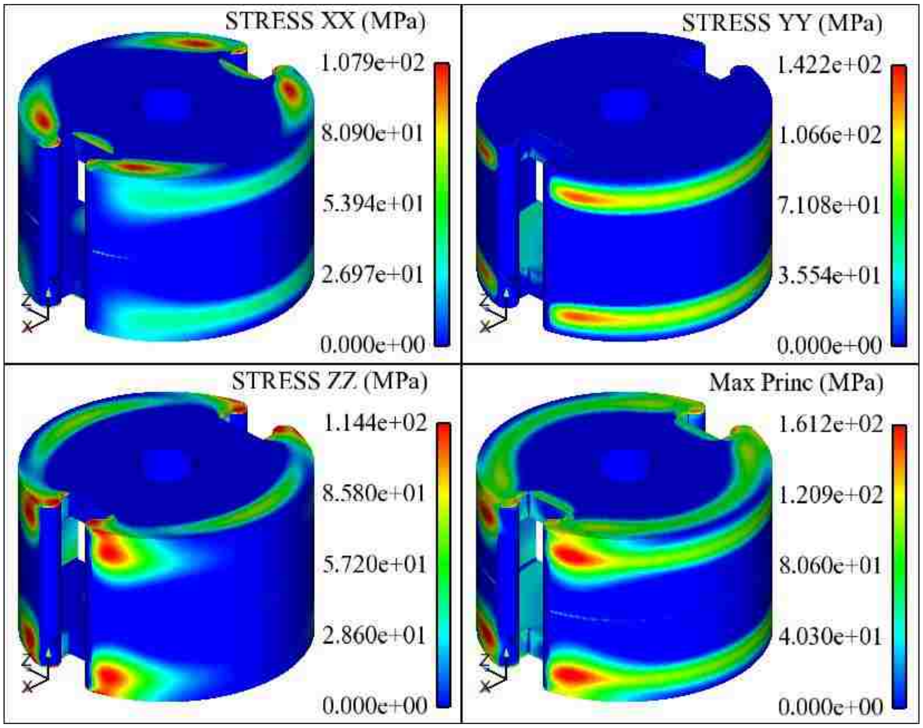

Figure 9-3: Contour plots of simulated (a) hydrostatic stress in encapsulant and (b) tensile stress directions and maximum principal stress in the ferrite core after cooling to -55°C, in the case of elastic analysis without the silicone coating.

Using the PEC model, calculations taking into account the nonlinear viscoelastic response of the filled epoxy encapsulation suggested that, after prolonged physical aging, the thermal stress in the ceramic core actually increased, primarily due to the contraction of the encapsulation with time. These results can be seen in Figure 9-4, and offer a mechanistic explanation on the performance of the transformer.

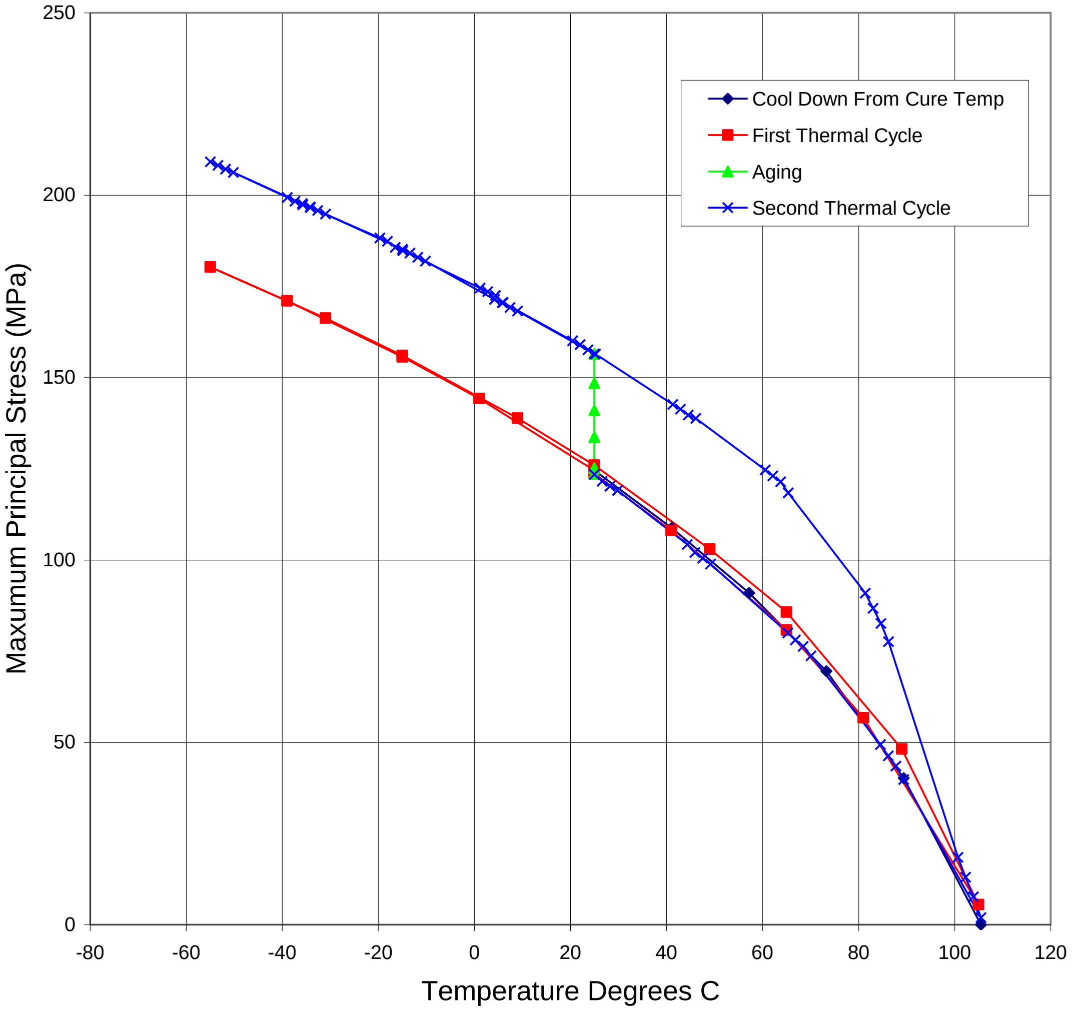

Figure 9-4: Simulated variation of the maximum principal stress with temperature at an element in the region of highest tensile stress on the outside diameter of the ferrite core, during the entire thermal history.

Ultimately, a significant stress reduction was realized when a thin silicone coating was incorporated in the model to decouple the encapsulant from the core. Because of the low adhesive strength of the silicone, it acts as a mold release which results in debonding of the confined epoxy from the ferrite transformer.

9.2 Component Positioning

In the previous chapters, an extensive parameter study was performed with the intent of understanding how variations in geometry and materials affect residual stress in packaged surface mount components. Another critical variable, however, is how objects packaged together in an assembly affect one another. Objects with significantly disparate CTE's packaged in an assembly can results in unintended board bending. One such example of board bending can be seen in Figure 9-5 (symmetrical about the x-y plane), and is the result of the packaging depicted in Figure 9-6. As might be expected, circuit board bending significantly affects the solder fatigue life of surface mounted components.

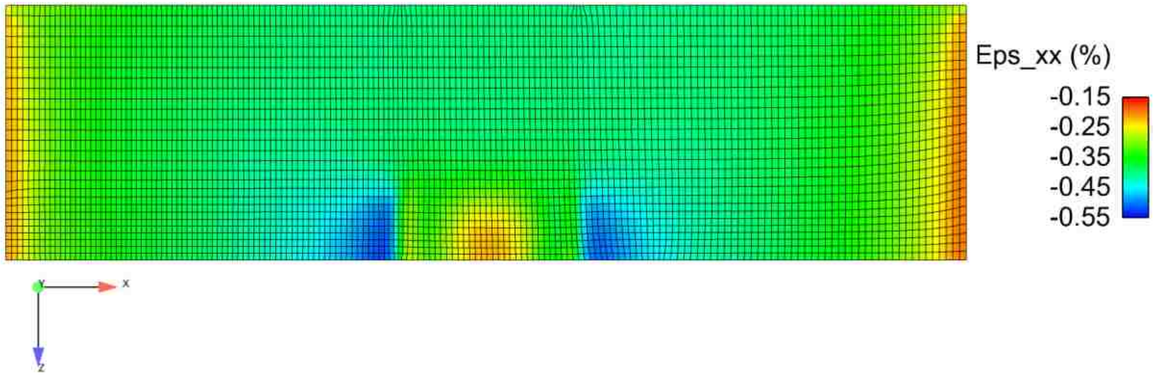

Figure 9-5: Contour plot of PCB strain due to GMB epoxy encapsulation and steel support.

Figure 9-6 demonstrates an encapsulated electronic assembly that is particularly susceptible to board bending. Because of the mismatch in coefficients of thermal expansion of the GMB epoxy over-encapsulation, steel board support, and other materials, significant bending of the board about the support was predicted using quasi-static, thermal stress finite element models. The effect of the PCB bending on solder fatigue life was investigated by utilizing submodels and tied contact to insert a component into the model at two separate locations. The component used for the calculations was the surface mount resistor described in Chapter 3.

As seen in the figure, the resistor was inserted above the board-to-support interface, and also at a more benign location from the support. The resistor was assumed to be coated with 0.02” PMB polysulfide coating with a 40% FVF GMB underfill. The thermal cycle consisted of cooling from 80°C to -55°C, followed by heating to 70°C, and finally cooling back to -55°C. The change in plastic strain used for the Coffin-Manson solder fatigue calculation (Section 2.4.2) was calculated between the two low thermal excursions of -55°C for eutectic tin-lead solder.

The results of the calculations were quite dramatic. The predicted fatigue life of the resistor located above the board support (Figure 9-6, top) was 27 thermals cycles until solder crack initiation, and the fatigue life of the resistor located away from the support (Figure 9-6, bottom) was calculated to be 140 thermal cycles. This represents a 418% increase in fatigue life, due only to position on the board with respect to the steel board support. While the calculation was not performed for foam encapsulation, the “trend” would be similar.

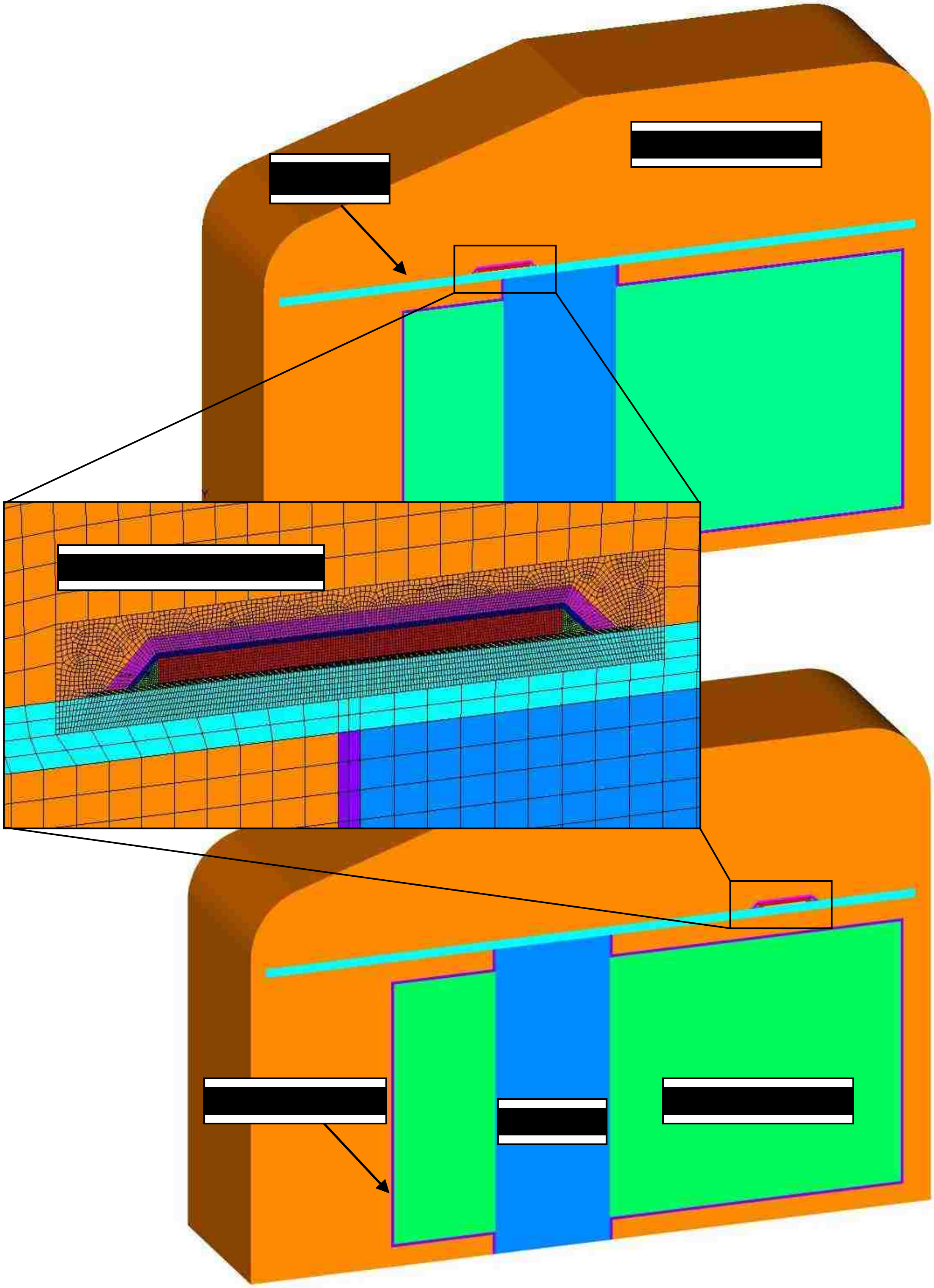

Figure 9-6: Half symmetry model of GMB epoxy encapsulated electronic device with resistor on PCB in two different locations.

10 Predicting Underfill Failure

10.1 Underfill Fatigue/Creep Failure

While high underfill residual stress can affect dynamic survivability, by reducing the margin to yield, fatigue and creep failure of the underfill also should be considered. Shown in Figure 10-1, is the maximum principal stress vs. maximum principal strain for underfill elements subjected to thermal cycles. The components investigated consisted of an 828/DEA/GMB epoxy encapsulated, 0.02” thick PMB polysulfide coated capacitor and resistor (as described in Chapter 3). The FVF for the underfills were 40% for both the GMB and hard fillers.

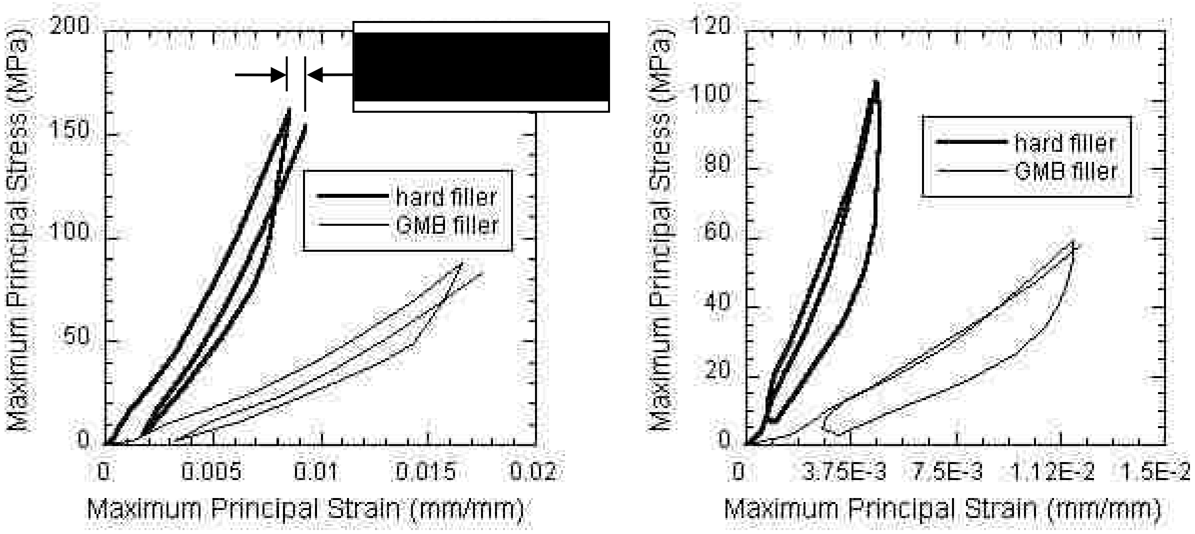

Figure 10-1: Epoxy encapsulated capacitor (left) and resistor (right) underfill maximum principal stress vs. maximum principal strain in underfill element.

As can be seen in the figure, permanent strain in the underfill increased significantly for the capacitor model during a thermal cycle, and less for the resistor model. The strain increase due to one thermal cycle for the capacitor was found to be ~0.001 for both the hard filler and GMB fillers, indicating that ~200 thermal cycles could lead to crack initiation if strain to failure was assumed to be 20% (assuming the same strain per thermal cycle). For the resistor, no permanent strain increase was realized due to the thermal cycle for the hard filled underfill case; however, a strain increment of 3.5E-4 was calculated for the GMB filled underfill, or ~570 thermal cycles to crack initiation. Clearly more investigation in this area is needed.

10.2 Plug on a Plate Tests and Modeling

Inconsistencies in solder geometry and the danger of breaking electrical connections make it undesirable to rely exclusively on solder joints to mechanically attach a component subjected to dynamic environments. Hence, to compensate, encapsulation or underfills are employed. To better understand underfill failure, experiments were performed with the simplest of geometries in an attempt to isolate any nonlinear response to the underfill itself. These tests were then modeled to investigate the role that runaway viscoelasticity plays in underfill failure. Coupled calculations were performed to include thermal processing (residual stress) followed by the desired dynamic or quasi-static loading. In addition, the underfill mesh geometries were modified to investigate the effects of mesh refinement and fillet geometry.

10.3 **Dynamic Impact**

Determination of mechanical characteristics of filled and unfilled thermosets and thermoplastics, including resistance to fracture under different conditions of loading, is of great importance in different branches of engineering. It appears that these materials show a delay time in their mechanical properties, especially in fast or impact loading [57]. In another example, the rate-dependence is clear, as both the global yield stress and plastic flow stress increase monotonically with increasing strain rate [58-60]. Efforts have also been made to model high rate polymer loading; however, the limitations discussed in Section 2.1 also apply to these (plasticity based) models [61]. Considering the success of the SPEC model at predicting the behavior of polymers under various quasi-static thermal and deformation histories, the next logical progression was the applications of the SPEC model to polymers under dynamic loading applications. Because potential energy is the basis for the nonlinear viscoelastic response in the SPEC model, an investigation of high rate predictions could give valuable insight into other possible applications of the model.

The finite element mesh for the dynamic impact test can be seen in Figure 11-2. The test was designed to impart a dynamic loading on the underfilled steel plug while varying the pendulum angle and the underfill thickness.

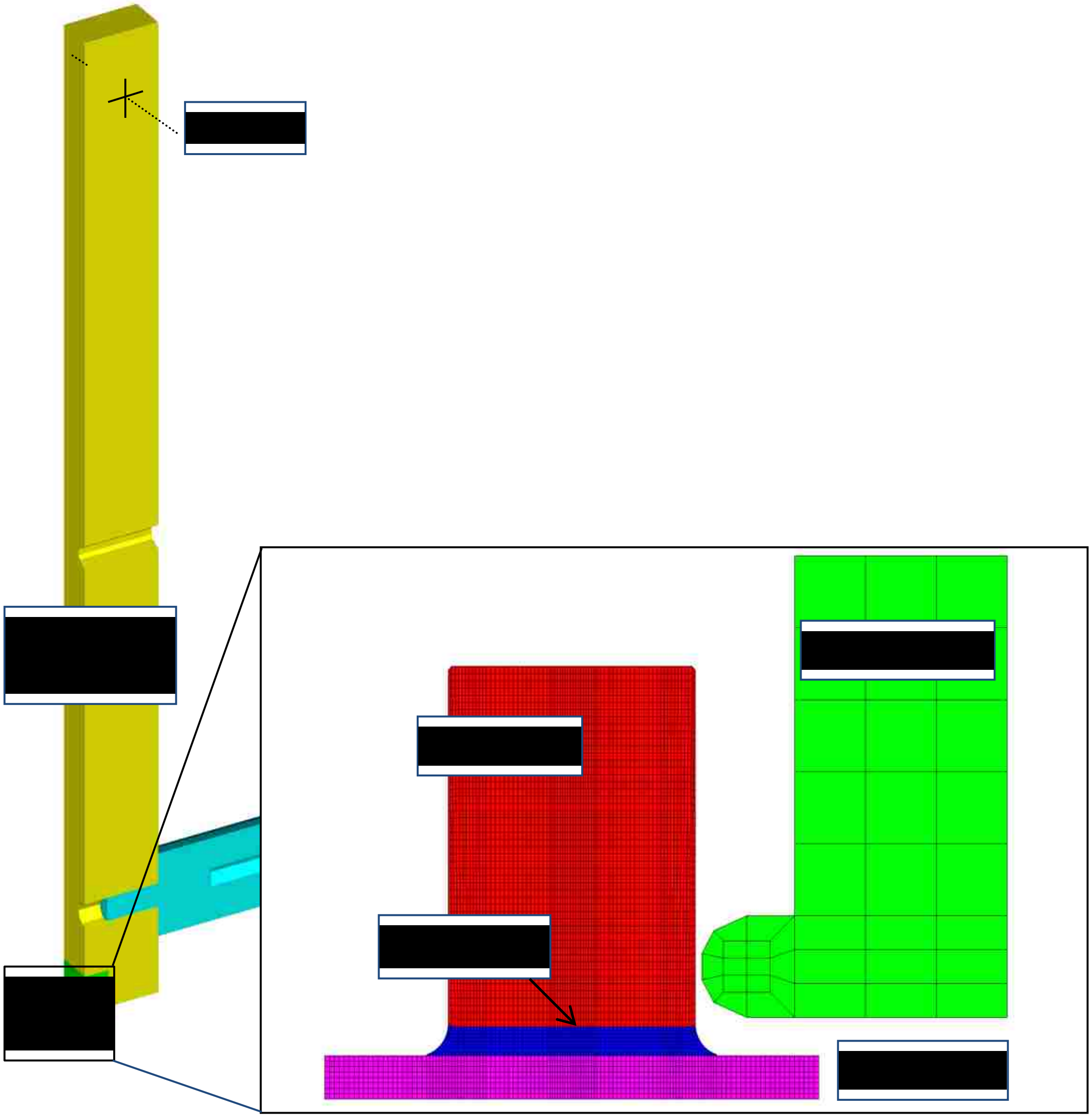

Figure 10-2: Pendulum and Steel Plug Finite Element Geometry.

Experimentally, underfill failure was achieved with pendulum angles ranging from 50 to 65 degrees for a cylindrical plug having a 0.04” thick, filleted underfill. The impact tests were performed by incrementally raising the pendulum 5 degrees until failure (cylinder pop-off) occurred. If underfill cracking initiated at smaller pendulum angles, it was not observed. Figure 10-3 depicts finite element stress-strain predictions for various impact angles. As can be seen in the figure, increased yielding occurs with increased pendulum angle. Typically in tension, glassy epoxy failure occurs with very little yielding, indicating that predicted failure initiation (cracks) might be evident after pendulum angles as low as 45 degrees. The stress and strain plotted are the maximums at given time steps regardless of location.

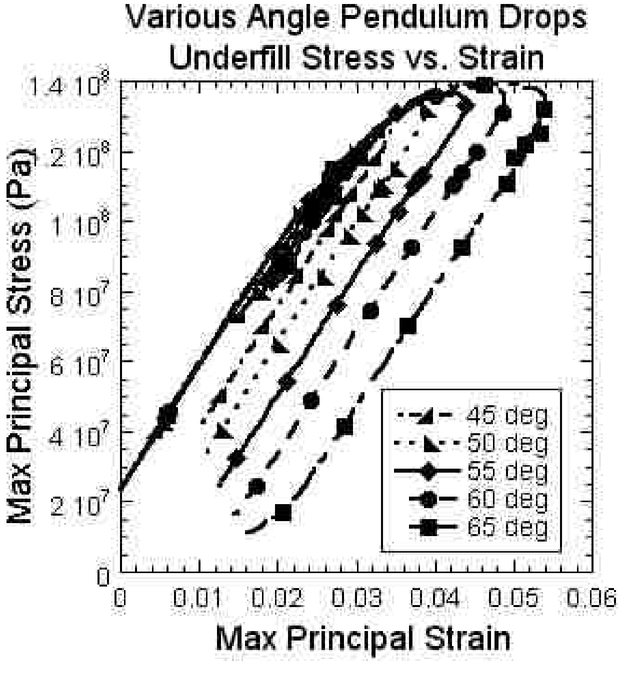

Figure 10-3: Predicted Underfill Stress vs. Strain for Various Pendulum Angles.

Following the somewhat promising initial predictions for the impact test, variations on fillet geometry and mesh resolution were also investigated. Using the case of the 45 degree pendulum drop, epoxy stress-strain predictions were compared. The models included high and low resolution mesh filleted geometries as well as a low resolution mesh unfilleted geometry (Figure 10-4). The results can be seen in Figure 10-5. As shown in the figure, for similarly located elements in the fillet, mesh resolution does not appear to be a significant factor for stress strain convergence. The unfilleted prediction, however, results in significantly higher stresses and strains. This difference may be important because underfill geometry is often simplified in finite element models, and the actual polymer fillets are neglected. To further investigate, quasi-static push-off tests were performed and also modeled.

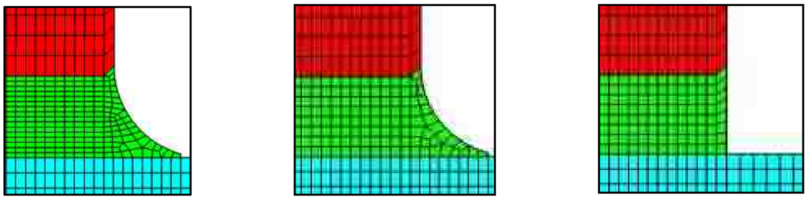

[redacted] [redacted] [redacted]

Figure 10-4: Finite Element Meshes for Fillet Geometry and Mesh Resolution Investigation.

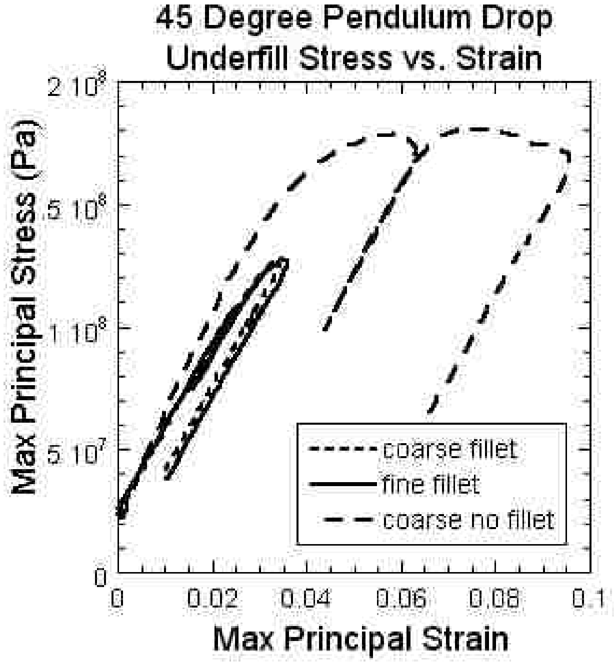

Figure 10-5: Peak Maximum Principal Strain in Underfill for 45 Degree Impact Angle.

10.4 Quasi-static Push-off

Quasi-static tests and models were also conducted using the same plug-on-a-plate geometry. A finite element mesh of the geometry can be seen in Figure 10-6. As with the dynamic impact tests the pusher, plug, and plate were made of stainless steel in an attempt to isolate any nonlinear material response to the underfill. Again, a 0.04" underfill thickness was assumed.

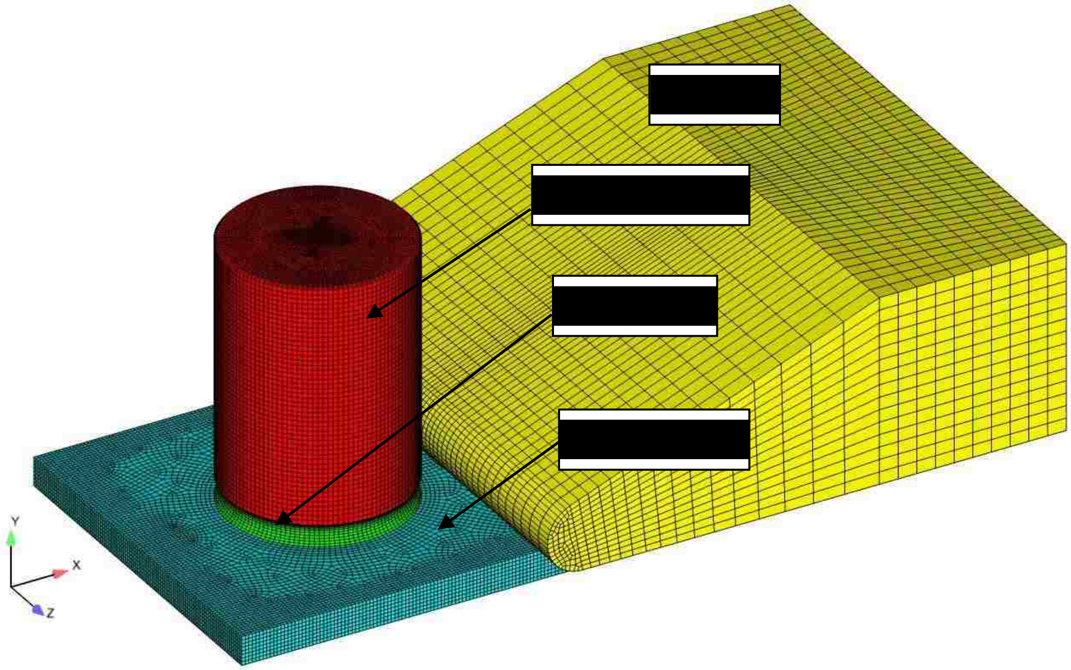

Figure 10-6: Pusher and Steel Plug Finite Element Geometry.

The experiments performed to corroborate the predictions were found to be more difficult than anticipated. Initially, fixture slop accounted for a significant amount of the measured displacement. As shown in Figure 10-7, the predicted response is significantly stiffer than the data. By removing unnecessary fixturing and using an extensometer to measure plug displacement, accurate data were finally measured.

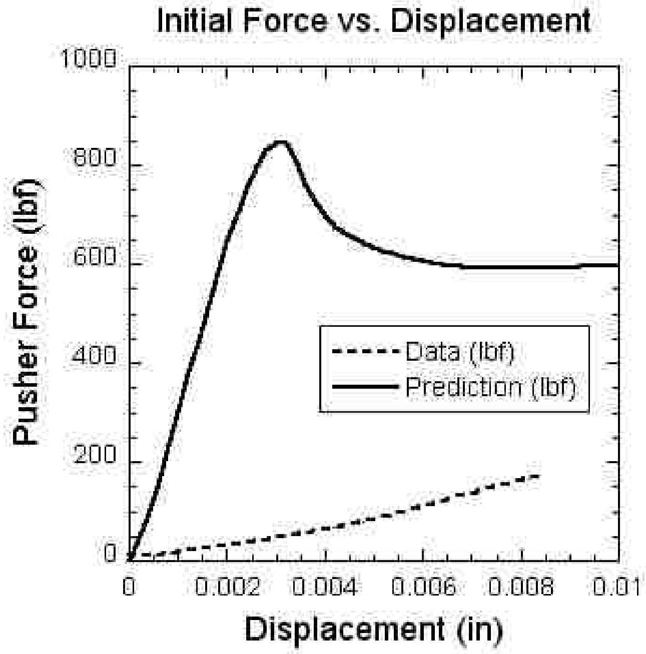

Figure 10-7: Predicted vs. Measured Pusher Force/Displacement with Fixture Slop.

Another disparity between the predictions and the data was that plastic yielding occurred between the stainless steel pusher and plug. As seen in Figure 10-8, as much as 12% equivalent plastic strain was predicted in the plug during a test.

By including plasticity in the model, and accurately measuring plug displacement, close agreement between the model and the experimental data was achieved (Figure 10-9). As can be seen in the figure, the predicted “runaway” viscoelastic response or yielding of the underfill occurs for pusher force of approximately 600 lbs, while the experimental data indicates underfill failure for a load of ~550 lbs.

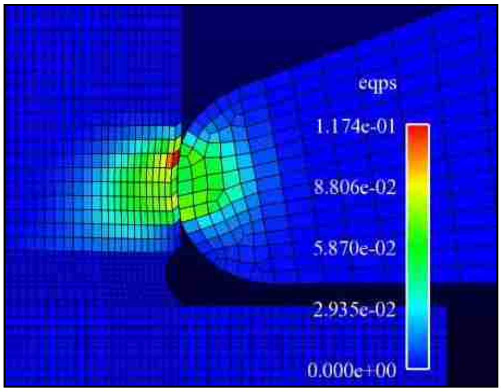

Figure 10-8: Contour Plot of Predicted Equivalent Plastic Strain in Pusher and Plug.

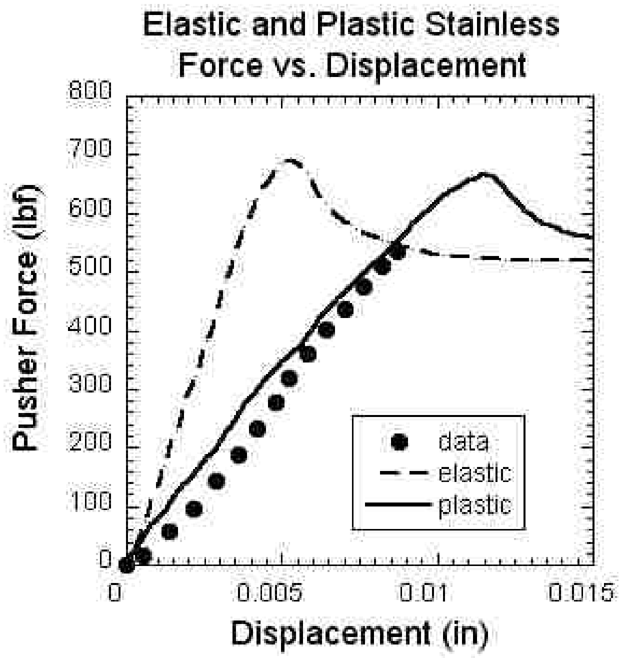

Figure 10-9: Predicted and Measured Pusher Force vs. Displacement.

Because of the wide variability encountered in underfill fillet geometry, a study was performed to determine the effect of fillet geometry on force-displacement predictions. Three fillet geometries were investigated and are depicted in Figure 10-10.

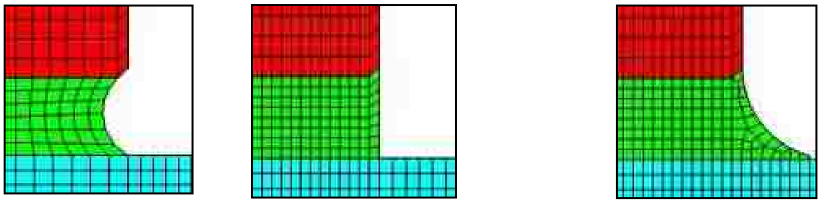

[redacted] [redacted] [redacted]

Figure 10-10: Finite Element Model Fillet Geometries.

The predicted force-deflection results from the various geometries can be seen in Figure 10-11. The data used for comparison were from undercut fillet geometry. As seen in the figure, fillet geometry does not significantly change the linear portion of the predicted force displacement response of the plug. This is encouraging because simplified geometry is often used in models of underfilled electronics.

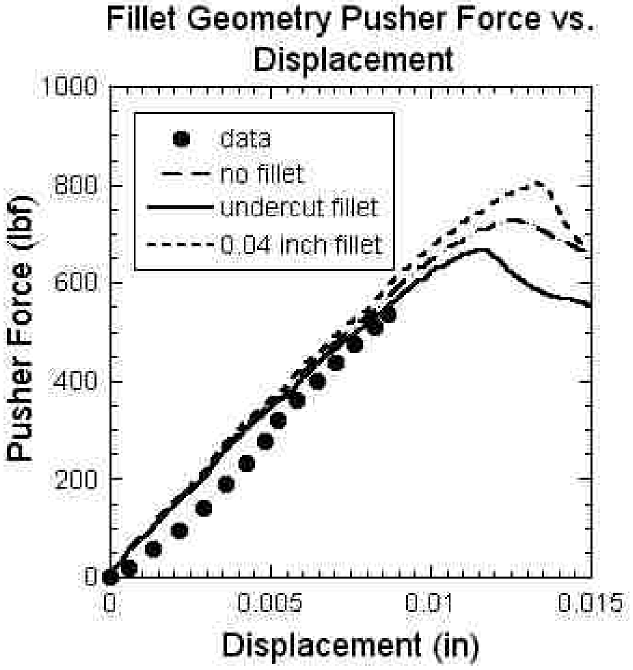

Figure 10-11: Predicted and Measured Pusher Force vs. Displacement for Various Fillet Geometries.

A mesh resolution study also was performed for the undercut fillet geometry.

Plots of the mesh refinements used in the analyses can be seen in Figure 10-12.

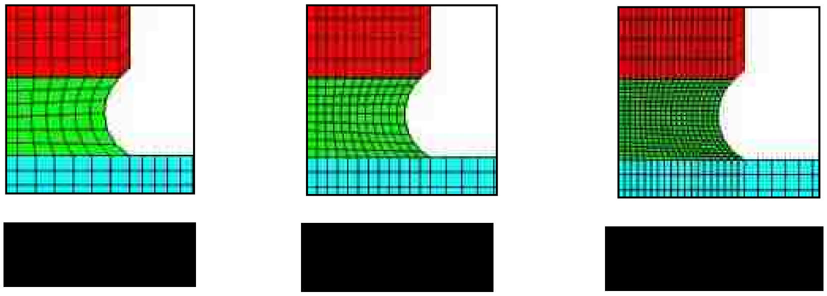

Figure 10-12: Mesh Refinement for Underfill Fillet Geometry.

Force deflection predictions for the mesh refinement study overlaid with the experimental data can be seen in Figure 10-13. There is very little difference between the results obtained from the various mesh resolution predictions.

Applied pusher force versus undercut underfill maximum principal strain (Figure 10-14) also was plotted for similarly located elements in the different mesh refinements. As seen in the figure, close agreement exists between the predictions. The experimental sample failed at an applied load of ~550 lbs, which is approaching the apparent “yield” in the force/strain plot. If “runaway” viscoelasticity were adopted as a mechanism of failure, the maximum principle strain might provide a good metric of when that occurs.

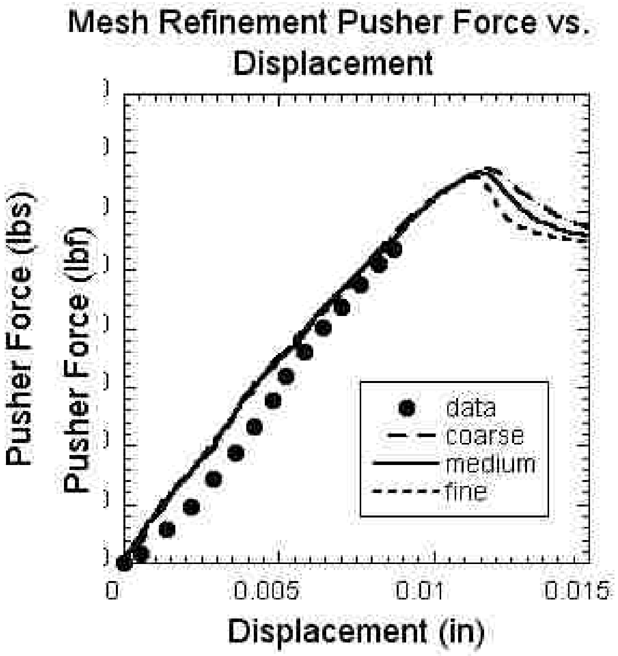

Figure 10-13: Predicted and Measured Pusher Force vs. Displacement for Various Mesh Refinements.

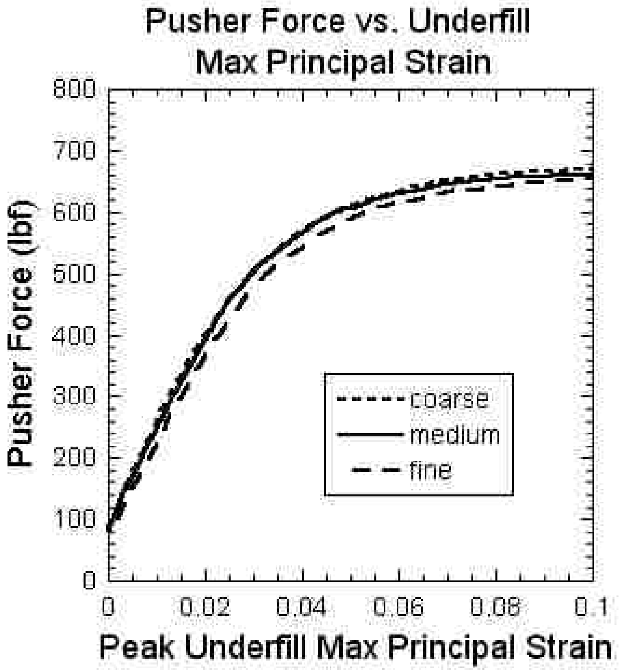

Figure 10-14: Pusher Load vs. Predicted Underfill Max Principal Stain for Various Mesh Refinements.

The results to this point indicate that the macroscopic response of plug deflection shows some small sensitivity to changes in fillet geometry and little sensitivity to mesh refinement for the undercut underfill. The question remaining is whether a maximum principal strain can be used to identify the onset of underfill failure. A mesh resolution study also was performed for the no fillet geometry, the configuration most likely to be meshed in a practical component analysis. Plots of the mesh refinements used in the analyses can be seen in Figure 10-15.

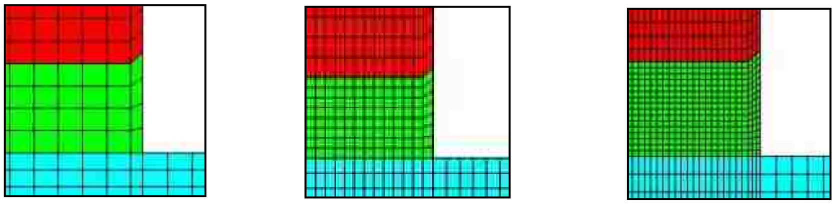

[redacted] [redacted] [redacted]

Figure 10-15: Mesh Refinement for Underfill Fillet Geometry.

Force deflection predictions for the mesh refinement study overlaid with the experimental data are shown in Figure 10-16. There is a noticeable difference between the results from the various mesh resolution predictions in the nonlinear regime (i.e., post yield). The peak pusher force decreases with mesh refinement and shows no evidence of convergence.

The applied pusher load verses underfill maximum principal strain is depicted in Figure 10-17. As seen in the figure, convergence with mesh refinement is not evident. Unlike the undercut unfilleted geometry, there is no convergence in the apparent “yield” marking a well-defined value for the onset of a runaway viscoelastic response. At the experimental failure load of ~550 lbs, the predicted elemental strain ranges from 3% to 10% for the coarse and fine meshes respectively.

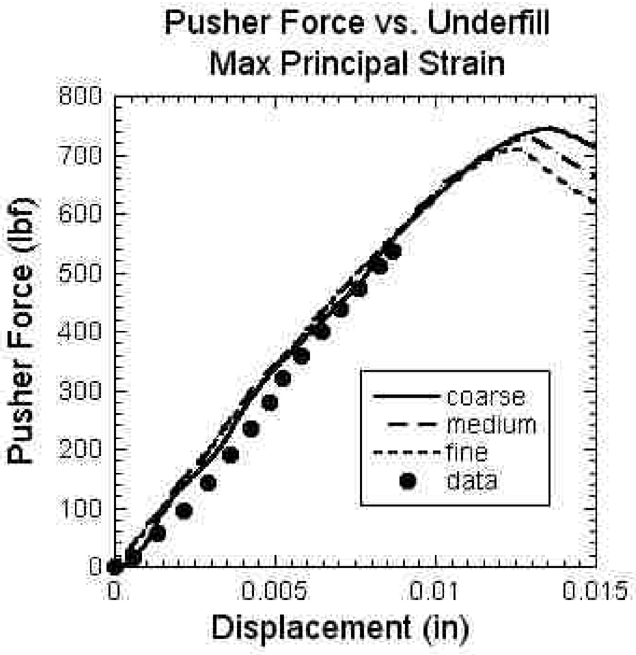

Figure 10-16: Predicted and Measured Pusher Force vs. Displacement for Various Mesh Refinements.

In the filleted and undercut fillet geometry, the peak maximum principal strains in the epoxy do not occur at an interface with the stainless steel. By assuming a square-fillet geometry, the epoxy peak maximum principal strain is located at the interface with the base plate, a location with a very high strain gradient. This means that although runaway viscoelasticity and a maximum principal strain failure metric may well correlate with failure, the predictions may be very sensitive to the details of the geometry which are not typically captured in large scale component analyses. If that is the case, then a more phenomenolocal viscoelastic failure metric may be required. This is to be determined.

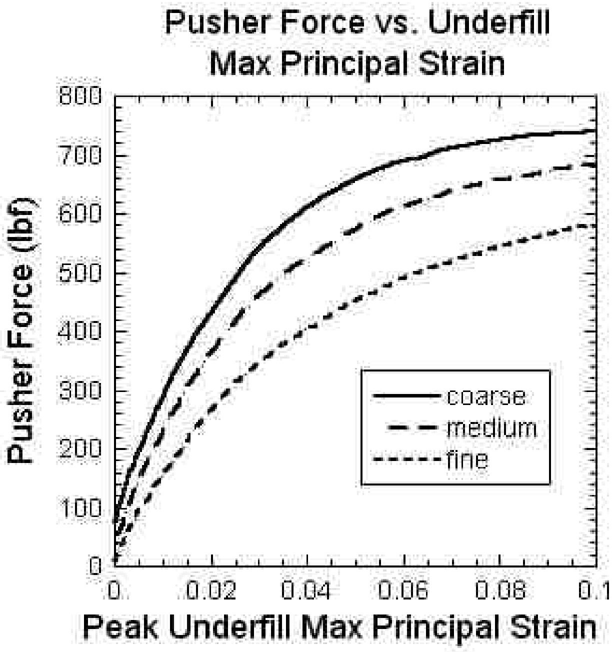

Figure 10-17: Pusher Load vs. Predicted Underfill Max Principal Strain for Various Mesh Refinements.

Following this preliminary effort, additional research in this area was conducted by Elisberg [62].

11 Component Level Dynamics

While understanding residual stress is critical to packaging design, our goal is to provide packaging guidelines for the complete lifecycle of surface mount components. The focus of the next sections is an initial attempt at investigating the response, at the component level, of a representative surface mount component subjected to various G loadings for various durations. The intent of the analyses was to determine at what acceleration level does a nonlinear material response (i.e. solder yielding, underfill viscoelasticity) appear.

Starting with the capacitor model shown in Figure 3-1, the encapsulation, coating, and circuit board material blocks were removed, leaving only the ceramic, underfill, solder, and solder pad (Figure 11-1). Linear elastic modal analyses were then performed (using half symmetry versions of the model when needed) to determine first modes in all three axes. A series of dynamic inputs was applied to the model following a cool-down from 80°C to 25°C as to include residual stress in the underfill. To achieve the dynamic response, a matrix of haversine pulses of increasing duration, bounding the identified natural frequency for the mode of loading, was applied for a constant G level. The acceleration was then increased incrementally and the process repeated until a nonlinear response was identified. At this point, the underfill/solder materials dampen the response due to a viscoelastic/plastic material response, which can be identified utilizing shock transmissibility plots.

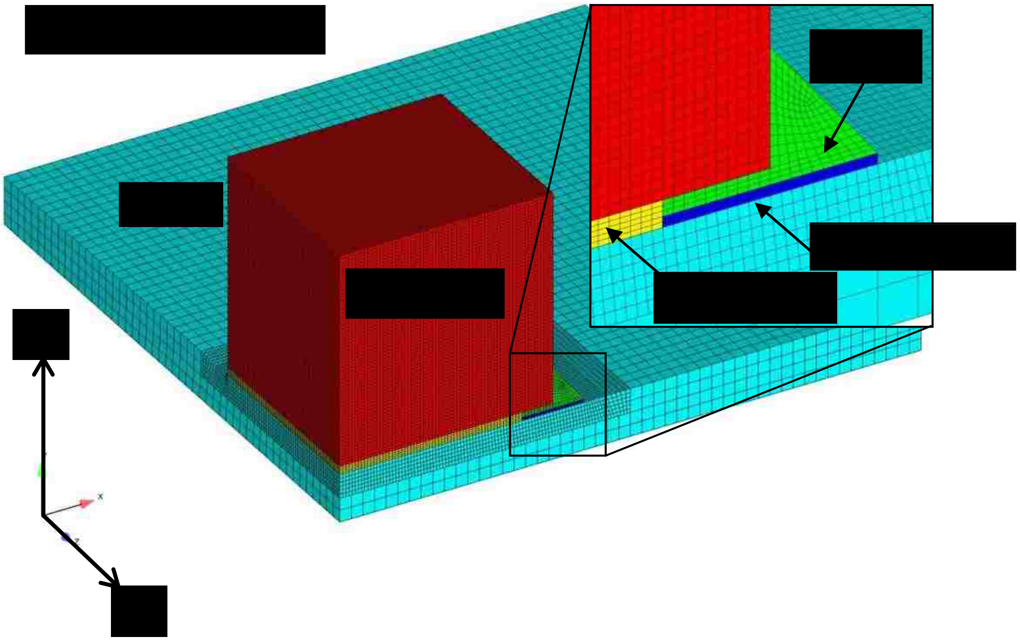

Figure 11-1: Finite element model of unencapsulated capacitor subjected to dynamic input.

11.1 Shock Transmissibility

The first normal mode (Y-direction) for the capacitor was calculated to be 1.57E5 Hz, and the resulting transmissibility curves for shock in the normal direction can be seen in Figure 11-2 (left). As shown in the figure no noticeable change in transmissibility occurs even at levels up to 100,000 G's. At 500,000 G's a decrease in the reaction can be seen, and at 1,000,000 G's significant damping is achieved. One could assume that retention of the component to the board is no longer likely at these levels, given that the underfill material would likely fail.

The first shear mode (Z-direction, parallel to solder joint) for the capacitor was calculated to be 7.41E4 Hz, and the resulting transmissibility curves for shock in the shear direction can be seen in Figure 11-2 (right). As seen in the figure, material nonlinearity was achieved at significantly lower accelerations than for the normal case. By 50,000 G’s, a noticeable decrease in the reaction was achieved. Again, one could assume that retention of the component to the board is unlikely at these levels.

An immediate conclusion that can be drawn from these dynamic results is that the representative component appears an order of magnitude stronger in normal loading than in shear. This result was made possible by the polymer constitutive model. Yield of the underfill material is not a property, but it is instead a structural response driven by rapid relaxation. These relaxation rates are a function of temperature, loading mode, and thermal history. In the normal calculation, a hydrostatic stress state was developed in the underfill material resulting in a longitudinal mode of loading dominated by the bulk modulus through K+4/3G, where K and G are the bulk and shear moduli respectively. The apparent yield stress of the polymer is significantly higher in this state of mixed mode loading. In the shear calculation, the underfill response was dominated by the significantly weaker apparent shear yield stress and modulus. It is important to note that the accelerations required to develop a nonlinear material response in this unencapsulated capacitor were significant. In the normal direction, as much as 500,000 G’s were required to develop yielding in the solder and underfill materials. These high G levels indicate that component failure will not likely be the result of inertial loading, especially in an encapsulated system.

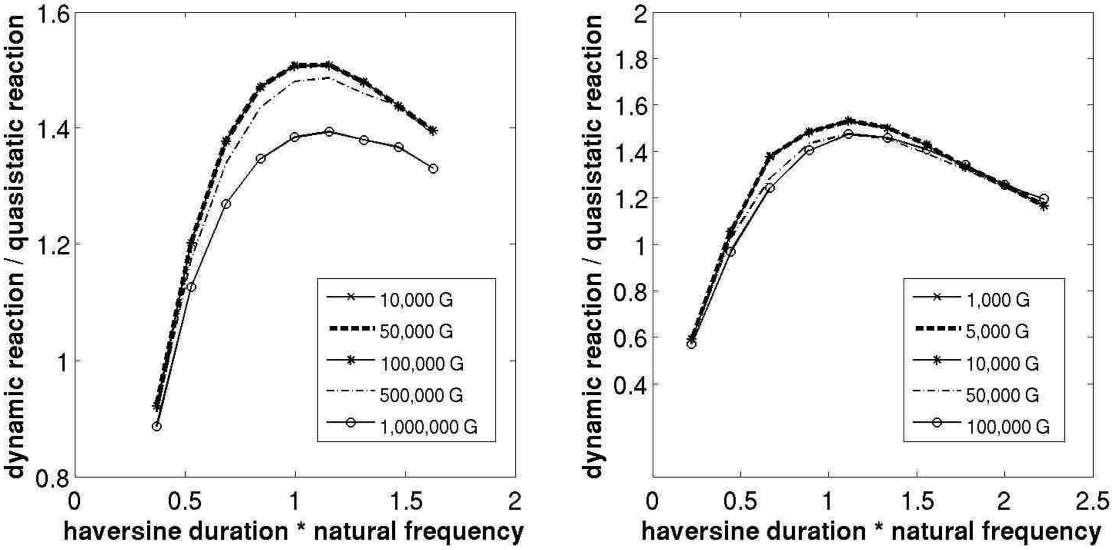

Figure 11-2: Capacitor Normal (left) and Shear (right) Shock Transmissibility.

12 Conclusions

Computational tools have been developed to analyze the stresses and strains generated in packaged electronic components. Some typical material data and constitutive equations for unfilled and filled glassy thermosets, elastomers and eutectic tin-lead solder also have been presented. Using these computational tools and material definitions, finite element analyses were performed to evaluate design options for generic surface mounted components subjected to thermal cycling only. From this effort, an attempt has been made to identify, where possible, simple design guidelines for surface mount electronics packaging by looking for “trends”.

12.1 Epoxy Encapsulation and Foam Encapsulation

The first, and most obvious, conclusion from these modeling efforts was that 828/DEA/GMB epoxy over encapsulation reduced the solder fatigue life of surface mount components by an order of magnitude relative to an unencapsulated system. Stress in the underfill was virtually unchanged, and the ceramic component stress was slightly increased by the addition of the epoxy over-encapsulation. Foam encapsulation reduced the solder fatigue life of capacitor by approximately one half of the unencapsulated value, but had relatively little impact on the fatigue life of the resistor. The stress in the underfill and ceramic were also relatively unaffected by the addition of foam encapsulation.

12.2 Elastomer Coatings

Unfilled elastomer coatings when over-encapsulated by an epoxy will likely result in tearing or debonding of the coating (important for finite element model boundary conditions). The filled elastomer coatings probably will not tear or debond. The application of the elastomer coating to the large encapsulated capacitor resulted in a significant reduction of hydrostatic stress in the ceramic. The cost, however, was a large increase in the localized ceramic stress at the solder joints.

12.3 Underfill Filler Volume Fraction

For unencapsulated/foam encapsulated components, optimal filler volume fractions in underfills were observed for solder fatigue. In some cases, it was found that adding filler to the underfill could increase or decrease the solder fatigue life, demonstrating the need for modeling. Furthermore, adding underfill could result in opposite trends for the capacitor and resistor, as adding underfill to the capacitor slightly decreased ceramic stress, while adding underfill to the resistor slightly increased ceramic stress, but in both cases, adding filler moved the stresses toward the no underfill stress state.

Under no circumstances is a void desirable under an 828/DEA/GMB epoxy encapsulated component. Amu underfill significantly increased solder fatigue life over the void condition. Adding hard filler to the underfill significantly increased the ceramic stress for the elastomer coated capacitor, but the stress increase was not as dramatic in the uncoated case. Increasing the filler volume fraction (FVF) of hard filler improved the solder fatigue life of epoxy encapsulated components, but GMB had a minimal effect. Increasing the hard FVF in the underfill increased the underfill stress, and increasing the GMB FVF in the underfill decreased the underfill stress.

12.4 Underfill Thickness

The most notable "trend" identified for the unencapsulated and foam encapsulated components, was the ability to optimize solder fatigue lives for underfilled components. By varying the underfill thickness, fatigue lives could be improved as much as 838%. The solder fatigue life predictions for all the 828/DEA/GMB epoxy encapsulated components experienced a huge monotonic increase in fatigue life with increased underfill thickness. In most cases, there was a direct correlation with low stress and high fatigue life.

12.5 Underfill Glass Transition Temperature

The most important finding from the underfill glass transition temperature study was that an underfill Tg should be close to the stress free temperature. Granted, in some cases it appeared that a Tg 20°C below the stress free temperature was best, and in others, 20°C above proved best, but in no case was a low Tg desirable. Low Tg underfill materials realized little benefit in component or underfill stress, and resulted in significant decreases in solder fatigue life.

12.6 Polymer Confinement

Because of its low adhesive strength, a significant stress reduction can be realized when a thin silicone coating is utilized as a mold release to decouple the encapsulant from a confining geometry.

12.7 Component Location

The results of the calculations were quite dramatic. The predicted fatigue life of the resistor located above the board-to-support interface (Figure 9-6, top) was 27 thermals cycles until solder crack initiation, and the fatigue life of the resistor located away from the support (Figure 9-6, bottom) was calculated to be 140 thermal cycles. This represents a 418% increase in fatigue life, due only to position on the board with respect to the steel board support.

12.8 Predicting Underfill Failure

In typical underfill modeling, simplifying assumptions such as square-fillet geometry result in the epoxy peak maximum principal strain being located at the interface with the PCB, a location with a very high strain gradient. This means that although runaway viscoelasticity and a maximum principal strain failure metric may well correlate with failure, but the predictions may be very sensitive to the details of the geometry.

12.9 Component Level Dynamics

The accelerations required to develop a nonlinear material response in an unencapsulated capacitor were significant. The levels were so high (500 KG's) that component failure will not likely be the result of inertial loading, but instead board from board bending.

References

[1] Neidigk, M. A. and Y.-L. Shen, "Nonlinear viscoelastic finite element analysis of physical aging in an encapsulated transformer," J. Electron. Packag., vol. 131, 011003, 2009.

[2] Adolf, D. B., R. S. Chambers, and M. A. Neidigk, "A simplified potential energy clock model for glassy polymers," Polymer, vol. 50, pp. 4257-4269, 2009.

[3] Salmon, E. R., 1987, Encapsulation of Electronic Devices and Components, Marcel Dekker, Inc., New York.

[4] Chung, D. D. L., 1995, Materials for Electronic Packaging, Butterworth-Heinemann, Boston.

[5] Lupinski, J. H. and Moore, R. S., 1989, Polymeric Materials for Electronics Packaging and Interconnection, American Chemical Society, Washington D.C.

[6] Pecht, M. G., Nguyen, L. T., and Hakim, E. B., 1995, Plastic-Encapsulated Microelectronics, Wiley, New York.

[7] Neilsen, M., B. Boyce, and P. Vianco, "A constitutive model for Sn-Pb Solder," in Proceedings of Materials Science & Technology 2010, Dr. John J. Stephens, Jr. Memorial Symposium: Deformation and Interfacial Phenomena in Advanced High-temperature Materials, p.824, 2010.

[8] Shen, Y.-L., N. Chawla, E. S. Ege, and X. Deng, "Deformation analysis of lap-shear testing of solder joints," Acta Mater., vol. 53, pp. 2633-2642, 2005.

[9] Moy, W. H. and Y.-L. Shen, "On the failure path in shear-tested solder joints," Microelectron. Reliab., vol. 47, pp. 1300-1305, 2007.

[10] Chawla, N. and R. S. Sidhu, "Microstructure-based modeling of deformation in Sn-rich (Pb-free) solder alloys," J. Mater. Sci.: Mater. Electron., vol. 18, pp. 175-189, 2007.

[11] Aluru, K., F.-L. Wen and Y.-L. Shen, "Modeling of solder fatigue failure due to ductile damage," J. Mech., vol. 26, pp. N23-N27, 2010.

[12] Shen, Y.-L. and K. Aluru, "Numerical study of ductile failure morphology in solder joints under fast loading conditions," Microelectron. Reliab., vol 50, pp. 2059-2070, 2010.

[13] Adolf, D. B., M. Neidigk, R. Chambers, M. Neilsen, S. Spangler, K. Austin, "Packaging Strategies for PCB Components, Vol. I: Materials & Thermal Stresses," Sandia National Laboratories Report SAND2011-4751, 2011

[14] Frear, D. R., S. N. Burchett, M. K. Neilsen, and J. J. Stephens, "Microstructurally based finite element simulation of solder joint behavior," Soldering Surf. Mount Technol., vol. 25, pp. 39-42, 1997.

[15] Solomon, H. D., "Fatigue of 60/40 solder," IEEE Trans. Components Hybrids Manuf. Technol., vol. 9, pp. 423-432, 1986.

[16] Caruthers, J. M., D. B. Adolf, R. S. Chambers, and P. Shrikhande, "A thermodynamically consistent, nonlinear viscoelastic approach for modeling glassy polymers," Polymer 45, 4577-4597 (2004)

[17] Ferry, J. D., Viscoelastic Properties of Polymers, (Wiley, New York, 1980)

[18] Arruda, E. M. and M. C. Boyce, "Evolution of plastic anisotropy in amorphous polymers during finite straining," Int. J. Plast., 9, 697-720 (1993)

[19] Boyce M. C., D. M. Parks, and A. S. Argon, "Large inelastic deformation of glassy polymers. Part I: Rate dependent constitutive model," Mech. Mater. 7, 15-33 (1988)

[20] G'Sell, C. and J. J. Jonas, "Yield and transient effects during the plastic deformation of solid polymers," J. Mater. Scie. 16, 1956-1974 (1981)

[21] Pandermarakis, Z. G., and B. Spathis, "Plastic behavior of glassy polymers: Experiment and theoretical description based on three different approximations," J. Appl. Polym. Sci. 97, 2032-2046 (2005)

[22] Ellyin, F. and X. Zihui, "Nonlinear Viscoelastic Constitutive Model for Thermoset Polymers," J. Eng. Mater. Tech. 128, 579-585 (2006)

[23] Hopkins, I. M., "Stress relaxation of linear viscoelastic substances under varying temperature," J. Polym. Sci. 28, 631-632 (1958)

[24] Morland, L. W. and E. H. Lee, "Stress analysis for linear viscoelastic materials with temperature variation," Trans. Soc. Rheol. 4, 233-263 (1960)

[25] Bernstein, B. and A. Shokooh, "The stress clock function in viscoelasticity," J. Rheol. 24, 189-211 (1980)

[26] Williams, M. L., R. F. Landel, and J. D. Ferry, "The temperature dependence of relaxation mechanisms in amorphous polymers and other glass-forming liquids," J. Am. Chem. Soc. 77, 3701-3707 (1955)

[27] Knauss, W. G. and I. J. Emri, "Non-linear viscoelasticity based on free volume consideration," Comp. Struc. 13, 123-128 (1981)

[28] Knauss, W. G. and I. J. Emri, "Volume change and the nonlinearity thermo-viscoelastic constitution of polymers," Polym. Engng. 27, 86-100 (1986)

[29] Shay, R. M., and J. M. Caruthers, "A new nonlinear viscoelastic constitutive equation for predicting yield in amorphous solid polymers," J. Rheol. 30, 781-827 (1986)

[30] Losi, G. U. and W. G. Knauss, "Free volume theory and nonlinear thermoviscoelasticity," Polym. Eng. Sci. 32, 542-557 (1992)

[31] Shay, R. M., and J. M. Caruthers, "A predictive model for the effects of thermal history on the mechanical behavior of amorphous polymers," Polym. Engng. Sci. 30, 1266-1280 (1990)

[32] Shapery, R. A., "On the characterization of nonlinear viscoelastic materials," Polym. Engng. Sci. 9, 295-310 (1969)

[33] Ruggles-Wrenn, M. B. and J. G. Balaconis, "Some aspects of the mechanical response of BMI 5250-4 neat resin at 191°C: Experiment and modeling," J. Appl. Poly. Sci. 107, 1378-1386 (2007)

[34] O'Connell, P. A. and G. B. McKenna, "The non-linear viscoelastic response of polycarbonate in torsion: An investigation of time-temperature and time-strain superposition," Mech. Time-Dep. Mater. 6, 207-229 (2002)

[35] Kwang, S. C. and S. Y. Kim, "Thermodynamic theory of the viscoelasticity and yield of glassy polymers: Internal time theory," J. Appl. Polym. Sci. 89, 2400–2411 (2003)

[36] Kovacs, A. J., J. M. Hutchinson, and A. R. Ramos, "Isobaric volume and enthalpy recovery of glasses. II. A transparent multiparameter theory," J. Polym. Sci.-Phys. 17, 1097-1162 (1979)

[37] Narayanaswammy, O. S., "A model of structural relaxation in glass," J. Am. Ceram. Soc. 54, 491-498 (1971)

[38] Hodge, I. M., “Enthalpy relaxation and recovery in amorphous materials,” J. Non-Cryst. Solids 169, 211-266 (1994)

[39] Johari, G. P., “A resolution for the enigma of a liquids configurational entropy-molecular kinetics relation,” J. Chem. Phys. 112, 8958-8969 (2000)

[40] Hodge, I. M. and J. M. O’Reilly, “Nonlinear kinetic and thermodynamic properties of monomeric organic glasses,” J. Phys. Chem. 103, 4171-4176 (1999)

[41] Pesce J. and G. B. McKenna, “Prediction of the subyield extension and compression responses of glassy polycarbonate from torsional measurements,” J. Rheol. 41, 929-942 (1997)

[42] Tervoort T. A., “A multi-mode approach to finite, three-dimensional, nonlinear viscoelastic behavior of polymer glasses,” J. Rheol. 40, 779-797 (1996)

[43] Plazek, D. J., “1995 Bingham medal address: Oh, thermorheological simplicity, wherefore art thou?” J. Rheol. 40, 987-1014 (1996)

[44] Truesdell, C., Rational Thermodynamics (Springer-Verlag, New York, 1984)

[45] Coleman, B. D. and W. Noll, “Foundations of linear viscoelasticity,” Rev. Mod. Phys. 33, 239-249 (1961)

[46] Coleman, B. D., “Thermodynamics of materials with memory,” Arch. Ration. Mech. Anal. 17, 1-46 (1964)

[47] Lustig, S. R., R. M. Shay, and J. M. Caruthers, “Thermodynamic constitutive equation for materials with memory on a material time scale,” J. Rheol. 40, 69-106 (1996)

[48] Adam, G. and J. H. Gibbs, “On the temperature dependence of cooperative relaxation in glass-forming liquids,” J. Chem. Phys. 43, 139-146 (1965)

[49] Adolf, D. B., R. S. Chambers, and J. M. Caruthers, “Extensive validation of a thermodynamically consistent, nonlinear viscoelastic model for glassy polymers,” Polymer 45, 4599-4621 (2004)

[50] Adolf, D. B., R. S. Chambers, and J. Flemming, “Potential energy clock model: Justification and challenging predictions,” J. Rheol. 51, 517-540 (2007)

[51] G'Sell, C. and G. B. McKenna, "Influence of physical ageing on the yield response of model DGEBA/poly (propylene-oxide) epoxy glasses," Polymer 33, 2103-2113 (1992)

[52] Colucci, D. M., P. A. O'Connell, and G. B. McKenna, "Stress relaxation experiments in polycarbonate: A comparison of volume changes for two commercial grades," Polym. Eng. Sci. 37, 1469-1474 (1997)

[53] Stephens, J. J. and D. R. Frear, "Time-dependent deformation behavior of near-eutectic 60Sn-40Pb solder," Metal. Mater. Trans. A, 30A, pp. 1301-1313, 1999.

[54] Neilsen, M., S. Burchett, C. Stone, J. Stephens, "A viscoplastic theory for braze alloys," SAND96-0984, Sandia National Laboratories, Albuquerque, NM, April 1996.

[55] ADAGIO/ANDANTE Users Reference Manual, Sandia National Laboratories, Albuquerque, New Mexico, 2005.

[56] Neidigk, M. A. and Y.-L. Shen, "Predicting the Effect of Underfill Filler Volume Fraction on Solder Fatigue Life and Residual Stress for Surface Mount Components Using Nonlinear Viscoelastic Analyses," IEEE T. Compon. Pack., Vol. 2, No. 9, Sept. 2012

[57] Klepaczko, J.R. Klepaczko, Y.V. Petrov, S.A. Atroshenko, P. Chevrier, G.D. Fedorovsky, S.I. Krivosheev, and A.A. Utkin, "Behavior of particle-filled polymer composite under static and dynamic loading", Eng. Frac. Mech. 75, 136-152 (2008)

[58] Arruda, E. M., M. C. Boyce, and R. Jayachandran, "Effects of strain rate, temperature, and thermomechanical coupling on the finite strain deformation of glassy polymers," Mech. Mater. 19, 193-212 (1995)

[59] Li, Zhouhua and J. Lambros, "Strain rate effects on the thermomechanical behavior of polymers," Int. J. Sol. Struct. 38, 3549-3562 (2001)

[60] Mulliken, A. D., S. Y. Soong, M. C. Boyce, and R. E. Cohen, "High-rate thermomechanical behavior of poly(vinyl chloride) and plasticized poly(vinyl chloride)," J. Phys. IV 134, 217-223 (2006)

[61] Richeton, J., S. Ahzi, K.S. Vecchio, F.C. Jiang, and A. Makradi, "Modeling and validation of the large deformation inelastic response of amorphous polymers over a wide range of temperatures and strain rates," Int. J. Solids and Structures 44, 7938-7954 (2007)

[62] Elisberg, B., “Predicting Adhesive Failure Initiation of an Epoxy Underfill for Electronic Packaging Survivability,” University of New Mexico Master’s Thesis, 2012